Time-resolved linear and non-linear rheology of thixotropic and aging complex fluids: Application to particulate and biopolymeric physical gels

by

Joshua David John Rathinaraj

B. Tech, Indian Institute of Technology - Madras (2019)

Submitted to the Department of Mechanical Engineering
in partial fulfillment of the requirements for the degree of

Master of Science

at the

MASSACHUSETTS INSTITUTE OF TECHNOLOGY

June 2021

Author .....
Department of Mechanical Engineering
May 14, 2021

Certified by .....
Prof. Gareth H. McKinley
School of Engineering Professor of Teaching Innovation
Thesis Supervisor

Accepted by .....
Prof. Nicolas Hadjiconstantinou
Chairman, Department Committee on Graduate Theses

Time-resolved linear and non-linear rheology of thixotropic and aging complex fluids:

Application to particulate and biopolymeric physical gels

by

Joshua David John Rathinaraj

Submitted to the Department of Mechanical Engineering
on May 14, 2021, in partial fulfillment of the
requirements for the degree of
Master of Science

Abstract

Temporal changes in microstructure and relaxation dynamics are ubiquitously observed in materials such as hydrogels, food products and drilling fluids. These materials are in general known as mutating materials and the build-up or breakdown of microstructure is commonly both time– and shear-rate (or shear-stress)–dependent resulting in a range of complex phenomena collected under the term thixotropy. It is becoming increasingly important to develop time-resolved rheometric techniques to quantify the behavior of mutating materials accurately.

In the present study we first discuss the introduction of better time-resolved techniques in superposition rheometry. Conventional superposition rheometry consists of combining Small Amplitude Oscillatory Shear (SAOS) with a steady unidirectional shear rate to gain insight into the shear-induced changes to the viscoelastic properties of a complex fluid. Orthogonal superposition (OSP), in which the two modes of deformation are perpendicular, has been preferred over parallel superposition to avoid non-linear cross-coupling of the steady shear and oscillatory deformation fields. This cross coupling can lead to unphysical sign changes in the measured material properties, and makes it difficult to interpret the flow-induced mechanical properties. Recently, orthogonal superposition has been used to investigate the shear-induced anisotropy taking place in colloidal gels by comparing the transient evolution of orthogonal moduli with the parallel moduli immediately after cessation of shear. However, probing transient evolution using the OSP technique can be challenging for rapidly mutating complex materials which evolve on time scales comparable to the time scale of the experiment. Using a weakly associated alginate gel, we demonstrate the potential of superimposing fast optimally windowed chirp (OWCh) deformations orthogonally to the shear deformation which substantially reduces the measurement time. We evaluate the changes in the rate-dependent relaxation spectrum in the direction of applied unidirectional shear rate and in the orthogonal direction deduced from the damping function and orthogonal moduli data respectively. We measure systematic changes between the two spectra measured in orthogonal directions thus revealing and quantifying flow-induced

anisotropy in the alginate gel.

Secondly, we develop a signal processing technique to monitor accurate temporal evolution of the complex modulus for a specified deformation frequency. Oscillatory rheometric techniques such as Small Amplitude Oscillatory Shear (SAOS) and, more recently, Large Amplitude Oscillatory Shear (LAOS) are now quite widely used for rheological characterization of the viscoelastic properties of complex fluids. However, the conventional application of Fourier transforms for analyzing oscillatory data assume the signals are time-translation invariant, which constrains the rate of mutation of the material to be extremely small. This constraint makes it difficult to accurately study shear-induced microstructural changes in thixotropic and gelling materials. We explore applications of the Gabor transform (a Short Time Fourier Transform (STFT) combined with a Gaussian window), for providing optimal joint time-frequency resolution of a mutating material's viscoelastic properties. First, we show using simple analytic models that application of the STFT enables extraction of useful data from the initial transient response following the inception of oscillatory flow. Secondly, using measurements on a Bentonite clay we show that using a Gabor transform enables us to more accurately measure rapid changes in both the storage and loss modulus with time, and also extract a characteristic thixotropic/aging time scale for the material. Finally, we consider extension of the Gabor transform to non-linear oscillatory deformations using an amplitude-modulated input strain signal, in order to track the evolution of the Fourier-Chebyshev coefficients characterizing thixotropic fluids at a specified deformation frequency. We show that there is a trade-off between frequency and time resolution (effectively a rheological uncertainty principle). We refer to the resulting test protocol as Gaborheometry and construct an operability diagram in terms of the imposed ramp rate and the mutation time of the material. This unconventional, but easily implemented, rheometric approach facilitates both SAOS and LAOS studies of time-evolving materials, reducing the number of required experiments and the data post-processing time significantly.

Finally, we use the time-resolved techniques developed in this thesis to understand the thixotropic aging behavior of bentonite dispersions. In soft glassy materials such as bentonite clays, the relaxation dynamics and the microstructure slowly but continuously evolve with time to progressively form more stable structures. We investigate and quantify this complex aging behavior of bentonite dispersions by measuring the evolution in the linear viscoelastic behavior at different age times and temperatures. We model the linear viscoelastic properties using a material time domain transformation and a fractional Maxwell gel model which allows us to develop a rheological master curve to quantify and predict the aging behavior of this soft glass over a range of temperatures and time scales.

The time-resolved rheometric techniques and procedures for quantifying the rheology of rapidly mutating complex fluids can be extended to a wide range of soft materials and allows us to obtain insight into how microstructural changes drive the evolution in the bulk rheological behavior for thixotropic and aging materials.

Thesis Supervisor: Prof. Gareth H. McKinley
Title: School of Engineering Professor of Teaching Innovation

Acknowledgments

This thesis wouldn't be complete without some key people and I am honored to have the chance to show my gratitude here.

First, I want to thank my advisor Professor Gareth H. McKinley for being not only an amazing guide but a role model I can look up to as an aspiring researcher. He has been a great teacher and patiently taught me the basics of research and the subject of rheology as I joined the lab without much knowledge about the field of non-Newtonian fluids. His mentoring has been greatly responsible for my growth as a graduate student researcher. I have greatly admired his love for science in general and the eagerness to learn new things. The way he approaches a research problem, the thought process in solving a problem has greatly influenced me. I have learned so much from him and am hoping to contribute an epsilon to his repository of knowledge in the upcoming years. Gareth, I am looking forward to exploring and learn with you the yet unexplored areas of complex fluids but now as a much better-equipped graduate student.

Secondly, I am beyond grateful for the friendship I have with Bavand, Michela, Sami and Anoop. They have been like my family away from home here and have been my go-to for everything. The numerous dinners in the pre-covid times, endless video calls during covid and all our conversations will be in my memories always. I can go on to write pages about these wonderful people but for the best interest of keeping the acknowledgement section within a couple of pages, I shall stop by saying "You guys are simply the best!". I am thankful for the friendship with Maanasa and Aditya who have been my good friends. Preparing for doctoral qualification exams, keeping up with all unexpected changes due to the pandemic has been an experience of a lifetime and I am so glad to have gone through it with them.

I am also indebted to all my lab mates especially Jianyi Du, Crystal, Ippolyti, Jae, Jake, Pablo and Igor for clarifying my doubts without any hesitations while working in the lab. I am thankful to all the friends I made here and some whom I knew from my undergrad: Arun, Raj, Sreedath, Baju, Richa, Elizabeth, SJ and Jacqueline. Thank you Rachel for your support while I was writing this thesis.

This work in the thesis would not have been possible without the collaboration with my collaborators: Jan Hendricks, Christian Clasen, Kyle R. Lennon, James Swan, Miguel Gonzalez and Ashok Santra. I would like to thank Jan Hendricks for collecting the orthogonal superposition data for alginate. Kyle has been my collaborator with the work on bentonite and his mathematical insights have been helpful for the work presented in this thesis. James Swan, Miguel Gonzalez and Ashok Santra met with me every two weeks and I have greatly benefited from their expertise. They have been accommodating and have constantly provided me with suggestions.

I am thankful to my friends at GCF and BSF, here at MIT. I am also thankful to my friends from childhood: Rohan, Godwin, Joel, Johnson, Stanly, Andrew, Vasanth, Evangeline, Sarah and Ram for their support throughout these two years.

Amma and Appa, None of this would have been possible if not for you both. Both of you placed my dreams over your career and priorities. All that I have achieved and I will achieve will always be *our achievements*. I love you both immensely! Thank you Richie and Sam for all your help and support always. Thank you for always being there. I am extremely fortunate and thankful to have had the prayers of my grandparents with me all the time. Thank you thatha, Ammachi, and Aachima.

A theory with mathematical beauty is more likely to be correct than an ugly one that fits some experimental data. God is a mathematician of a very high order, and He used very advanced mathematics in constructing the universe.

-**Paul Adrien Maurice Dirac**

Contents

List of Figures

List of Tables

Chapter 1

Introduction

1.1 Rheology

Rheology is the study of the deformation and flow of matter [73]. The first scientific contribution in understanding the response of a fluid due to the imposed kinematics was introduced by Newton in the 1600s. He put forward the theory that for simple fluids, the shear rate and shear stress follow a linear relationship. The fluids which follow this flow behavior are now known as Newtonian fluids whose examples including air and water. Rheology mainly deals with investigating the deformation and flow behavior of fluids which do not follow the Newtonian relationship, often called as non-Newtonian fluids or complex fluids. Some of the key phenomena which complex fluids may exhibit are viscoelasticity (eg. silly putty), shear thinning or thickening, presence of a yield stress and large extensional viscosity. Viscoelasticity is the property of a material to demonstrate both elastic and viscous behavior. The phenomena of increase and decrease of viscosity with shear rate in complex fluids is known as shear thinning and shear thickening respectively. The experimental techniques for determining the rheological properties of materials, such as relationships between stress, strain and strain rate are collected under the term rheometry and the laboratory devices used for such measurements are known as rheometers.

Most of the fluids we encounter in everyday use apart from air and water such as polymers, emulsions, suspensions, pastes, foams and food products are all complex fluids. These fluids are of great importance to a wide range of industrial and bio-medical

applications. Therefore, over the past 80 years, there has been significant efforts devoted to developing constitutive equations for the relationships between material properties and imposed deformation kinematics to quantify the behavior of complex fluids. The two most common types of rheology are shear flow rheology and extensional rheology which deals with elongational flows. In this thesis, we will be focusing only on shear flow rheology.

1.2 Shear flow rheology

Shear flow is the most common type of flow in rheology. The velocity of the shear flow is unidirectional and adjacent layers of fluid slide over each other and do not mix [73]. Such a flow can be established in a rheometer using several geometry configurations such as the plate-plate and cone-plate configuration. The fluid is constrained between the two rigid walls of the fixture and one of the plates is moved with a steady or oscillatory velocity in a single constant direction. A schematic figure showing shear flow between two parallel plates is shown in the Fig. 1-1. The kinematics of any fluid deformation may be represented

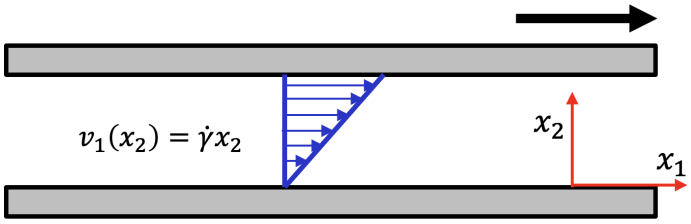

Figure 1-1: Shear flow between two parallel plates. Only the top plate moves in the x_1 direction effecting shear flow. Figure inspired from [73].

by a symmetric tensor, called the rate of strain tensor which is defined in terms of the gradient of velocity field and its transpose:

$$\dot{\gamma} = \nabla \boldsymbol{v} + \nabla \boldsymbol{v}^T \tag{1.1}$$

where $\boldsymbol{v}(\boldsymbol{x}; t)$ is the velocity vector at position $\boldsymbol{x}$ and time t.

The stress tensor for any arbitrary flow or deformation can be written as:

$$\boldsymbol{\sigma} = \begin{pmatrix} \sigma_{11} & \sigma_{12} & \sigma_{13} \\ \sigma_{21} & \sigma_{22} & \sigma_{23} \\ \sigma_{31} & \sigma_{32} & \sigma_{33} \end{pmatrix} \tag{1.2}$$

The stress tensor is symmetric for isotropic materials in the asence of non-conservative body force and hence has only six unknown coefficients since $\sigma_{ij} = \sigma_{ji}$.

For a homogeneous shear flow in the x_1-x_2 plane as seen in in Fig. 1-1, the velocity vector may be written as:

$$\boldsymbol{v} = \begin{pmatrix} v_1 \\ v_2 \\ v_3 \end{pmatrix} = \begin{pmatrix} \dot{\gamma}(t)x_2 \\ 0 \\ 0 \end{pmatrix} \tag{1.3}$$

where $\dot{\gamma}(t)$ is commonly referred to as the shear rate. Therefore, the rate of strain tensor for shear flow in x_1-x_2 direction is given as:

$$\dot{\boldsymbol{\gamma}} = \begin{pmatrix} 0 & \dot{\gamma}(t) & 0 \\ \dot{\gamma}(t) & 0 & 0 \\ 0 & 0 & 0 \end{pmatrix} \tag{1.4}$$

and the corresponding stress tensor for shear flow deformation is given by

$$\boldsymbol{\sigma} = \begin{pmatrix} \sigma_{11}(t) & \sigma_{12}(t) & 0 \\ \sigma_{21}(t) & \sigma_{22}(t) & 0 \\ 0 & 0 & \sigma_{33}(t) \end{pmatrix} \tag{1.5}$$

The normal stress differences N_1 and N_2 are defined as $N_1 = \sigma_{11} - \sigma_{22}$ and $N_2 = \sigma_{22} - \sigma_{33}$ For the purpose of ease, we will note the shear stress σ_{12} as just σ in this chapter.

1.2.1 Steady simple shear flow

When the deformation rate is homogeneous and applied shear rate in driving the flow is constant i.e. $\dot{\gamma}(t) = \dot{\gamma}_0$ in Eq. (1.26), we consider the shear flow to be steady simple shear flow. For steady shear flow, we define the material function viscosity as the ratio of shear stress to shear rate.

$$\eta(\dot{\gamma}) = \frac{\sigma}{\dot{\gamma}_0} \tag{1.6}$$

1.2.2 Creep

When the flow of the fluid is driven by constant shear stress instead of shear rate, it is known as s creep. The shear strain accumulated in the material between two times t_1 and t_2 due to the finite shear rate resulting from the shear stress imposed on the material is:

$$\gamma(t_1, t_2) = \int_{t_1}^{t_2} \dot{\gamma}(t')dt' \tag{1.7}$$

The constant shear stress $\sigma(t) = \sigma_0$ is applied for $t \geq 0$ and the material function, creep compliance J is defined as:

$$J(t, \sigma_0) = \frac{\gamma(0, t)}{\sigma_0} \tag{1.8}$$

In the linear viscoelastic limit the material strain increases linearly with the imposed stress and we can define the linear viscoelastic creep compliance as:

$$J(t) = \frac{\gamma(t)}{\sigma_0} \tag{1.9}$$

1.2.3 Step strain

In step strain experiments, a constant shear strain γ_0 is imposed at time $t = 0$. The material function, stress relaxation modulus $G(t, \gamma_0)$ is defined as:

$$G(t, \gamma_0) = \frac{\sigma(t, \gamma_0)}{\gamma_0} \tag{1.10}$$

For small strains, the relaxation modulus becomes independent of the applied strain.

$$G(t) = \frac{\sigma(t, \gamma_0)}{\gamma_0} \tag{1.11}$$

This limit is noted as the linear viscoelastic regime. In general, $G(t)$ is referred to as the linear viscoelastic relaxation modulus.

To quantify the extent of non-linearity arising in a complex fluid at higher strains an additional material function, the damping function $h(\gamma)$ is defined as:

$$h(\gamma_0) = \frac{G(t, \gamma_0)}{G(t)} \tag{1.12}$$

1.2.4 Small Amplitude Oscillatory Shear

In Small Amplitude Oscillatory Shear (SAOS), an oscillatory shear strain or shear stress within the linear viscoelastic regime with a specified deformation frequency is applied as input to drive the flow periodically. This enables a systematic probing of the time-dependent response of the material. The material functions for Small Amplitude Oscillatory Shear strain are the storage modulus $G'(\omega)$ and loss modulus $G''(\omega)$. In the complex plane, the material function from SAOS is referred to as the complex moulus G^* and is given by

$$G^*(\omega) = G'(\omega) + iG''(\omega) = \frac{\tilde{\sigma}(\omega)}{\tilde{\gamma}(\omega)} \tag{1.13}$$

where $\tilde{\sigma}(\omega)$ is the Fourier transform of the stress signal and $\tilde{\gamma}(\omega)$ is the Fourier transform of the strain signal.

These material functions vary with the frequency of deformation ω. The real part of the complex modulus corresponds to the storage modulus and the imaginary part of the complex modulus is the loss modulus. For an input strain of $\gamma(t) = \gamma_0 \sin(\omega_0 t)$, the resulting stress can be written in terms of the storage modulus and loss modulus as:

$$\sigma(t) = \gamma_0 \left(G'(\omega) \sin(\omega_0 t) + G''(\omega) \cos(\omega_0 t)\right) \tag{1.14}$$

Conversely, if a small oscillatory stress is applied as input known as SAOStress, it is

more convenient to represent the measured output strain in terms of the complex compliance J^* which can be defined for any deformation frequency ω as:

$$J^*(\omega) = J'(\omega) + iJ''(\omega) = \frac{\tilde{\gamma}(\omega)}{\tilde{\sigma}(\omega)} \tag{1.15}$$

where $J'(\omega)$ and $J''(\omega)$ are referred to as the elastic compliance and viscous complex compliance respectively.

1.3 Constitutive relations

1.3.1 General Linear Viscoelastic model

Boltzmann argued that the linear stress response for any small shear deformation for any complex fluid can be written as:

$$\boldsymbol{\sigma}(t) = \int_{-\infty}^{t} G(t-t')\dot{\boldsymbol{\gamma}}(t')dt' \tag{1.16}$$

where $G(t-t')$ is the time dependent relaxation modulus [7]. This Boltzmann superposition integral Eq. (1.16) can be re-written using memory function $M(t-t')$ which is defined as

$$M(t-t') = -\frac{\partial G(t-t')}{\partial t'} \tag{1.17}$$

Using integration by parts, Eq. (1.16), the stress tensor for General Linear Viscoelastic model may be written in terms of memory function as:

$$\boldsymbol{\sigma}(t) = \int_{-\infty}^{t} M(t-t')\boldsymbol{\gamma}(t,t')dt' \tag{1.18}$$

From applying Fourier transform on both sides of the Eq. (1.16), we can obtain the complex modulus G^*in terms of the relaxation modulus $G(t)$. The complex modulus G^* acts as the transfer function between the shear stress and shear rate :

$$G^*(\omega) = i\omega \int_{t=0}^{t=\infty} G(t)e^{-i\omega t}dt \tag{1.19}$$

It is also common in rheology to represent the material response by continous relaxation spectrum $H_0(\tau)$. By using the idea of relaxation spectrum, the relaxation modulus can be written in an expression implying a continuum of exponentials [7]. The relationship between the relaxation modulus and the spectrum may be written as:

$$G(s) = \int_{-\infty}^{\infty} H_0(\tau) e^{-s/\tau} d\ln\tau \tag{1.20}$$

Therefore, either specifying relaxation modulus or relaxation spectrum is sufficient to describe the material's response in the linear viscoelastic regime. By using Eq. (1.19), we can write the complex modulus in terms of the relaxation spectrum:

$$G'(\omega) = \int_{0}^{\infty} H(\tau) \frac{\omega^2\tau^2}{1+\omega^2\tau^2} d\ln\tau \tag{1.21}$$

$$G''(\omega) = \int_{0}^{\infty} H(\tau) \frac{\omega\tau}{1+\omega^2\tau^2} d\ln\tau \tag{1.22}$$

1.3.2 K-BKZ constitutive equation

In the 1960s, Bernstein, Keasley and Zapas as well as Kaye working independently suggested a generalized constitutive equation to capture viscoelastic response of complex materials in non-linear deformations [106, 93, 6, 7]:

$$\boldsymbol{\sigma}(t) = \int_{-\infty}^{t} \left[\frac{\partial U}{\partial I_1} \boldsymbol{C^{-1}}(t,t') - \frac{\partial U}{\partial I_2} \boldsymbol{C}(t,t') \right] dt' \tag{1.23}$$

Here, $\boldsymbol{C(t,t')}$ and $\boldsymbol{C^{-1}(t,t')}$ are the Cauchy-Green strain tensor and Finger strain tensor respectively and where the shear strain $\gamma(t,t')$ is

$$\gamma(t,t') = \int_{t}^{t'} \dot{\gamma}(t'')dt'' \tag{1.24}$$

Without going into details of these finite strain tensors (see DPL volume 1 chapters 8-9 for details [7]), we specify the form of these strain tensors for a shear flow with an arbitrary

shear strain $\gamma(t,t')$:

$$\boldsymbol{C^{-1}}(t,t') = \begin{pmatrix} 1+\gamma^2(t,t') & -\gamma(t,t') & 0 \\ -\gamma(t,t') & 1 & 0 \\ 0 & 0 & 1 \end{pmatrix} \tag{1.25}$$

$$\boldsymbol{C}(t,t') = \begin{pmatrix} 1 & -\gamma(t,t') & 0 \\ -\gamma(t,t') & 1+\gamma^2(t,t') & 0 \\ 0 & 0 & 1 \end{pmatrix} \tag{1.26}$$

I_1 and I_2 are the first and second invariants the Finger strain tensor $C^{-1}(t,t')$.

$$I_1 = tr\left(\boldsymbol{C^{-1}}\right) \tag{1.27}$$

$$I_2 = \frac{1}{2}\left[tr\left(\boldsymbol{C^{-1}}\right)^2 - tr\left(\left(\boldsymbol{C^{-1}}\right)^2\right)\right] \tag{1.28}$$

In Eq. (1.23) $U(I_1, I_2)$ is a strain energy potential function and the predictions to the response from K-BKZ model depends on the choice of potential function. Wagner further simplified the the K-BKZ model by the assumption that the potential function is independent of the second invariant and represented the constitutive equation for the shear stress in terms of memory function and the damping function defined above:

$$\boldsymbol{\sigma(t)} = \int_{-\infty}^{t} M(t-t')h(I_1, I_2)\boldsymbol{C^{-1}}(t,t')dt' \tag{1.29}$$

For shear flow, the invariants are equal and given by

$$I_1 = I_2 = \gamma^2 + 3 \tag{1.30}$$

Therefore, the shear stress can be written as:

$$\sigma(t) = \int_{-\infty}^{t} M(t-t')h(\gamma)\gamma(t,t')dt' \tag{1.31}$$

1.3.3 Lodge-type Constitutive model

The K-BKZ model is written in terms of strain. To think of liquid-like materials in terms of strain rates, the Lodge-type constitutive model is used. This constitutive equation has been used commonly for superposition rheometry where two shear flows typically a linear oscillatory flow and a steady shear flow are imposed simultaneously to probe the material's non-linear response [105]. The stress response can be written in the general form

$$\boldsymbol{\sigma}(t) = -p\boldsymbol{I} + \int_{-\infty}^{t}\int_{-\infty}^{\infty} \frac{H(\tau, II_{2\dot{\gamma}})}{\tau} \exp\Big(-\frac{(t-t')}{\tau}\Big) d\ln\tau [\boldsymbol{C^{-1}}(\boldsymbol{t},\boldsymbol{t'}) - \boldsymbol{I}]dt' \tag{1.32}$$

Here, H is the non-linear relaxation spectrum which depends on the applied deformation rate amplitudes unlike the linear spectrum $H_0(\tau)$ defined above in Eq. (1.20) and $II_{2\dot{\gamma}}$ is the second invariant of the rate of strain tensor. This constitutive equation is discussed in detail in chapter 2 and hence its not discussed further in this section.

1.4 Mechanical models to represent the material functions

"I can never satisfy myself until I can make a mechanical model of a thing. If I can make a mechanical model I can understand it. As long as I cannot make a mechanical model all the way through I cannot understand." - Lord Kelvin

The material functions of these complex fluids can often be represented by simple linear and non-linear mechanical models. The earliest mechanical models for describing the general response of these complex materials were initiated by Maxwell, Kelvin and Voigt who have had their presence felt in every field of classical physics.

1.4.1 Maxwell model

Maxwell suggested a combination of a spring and dashpot in series to represent the viscoelastic behavior. The stress-strain or shear rate relationship for a Hooken spring is $\sigma = G_0\gamma$ and for a linear dashpot (or damping element) is given as $\sigma = \eta_0\dot{\gamma}$. The total strain or shear rate from the Maxwell is the summation of the the response from the spring

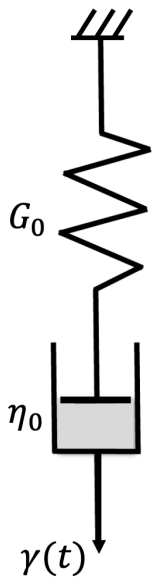

Figure 1-2: Mechanical model representation of the linear Maxwell model consisting of a combination of spring and dashpot elements in series.

and the dashpot and the stress experienced by both spring and dashpot is the same.

$$\dot{\gamma}(t) = \dot{\gamma}_{spring}(t) + \dot{\gamma}_{dashpot}(t) \tag{1.33}$$

Therefore, constitutive equation for the Maxwell model may be written as:

$$\sigma(t) + \frac{\eta_0}{G_0}\frac{d\sigma(t)}{dt} = \eta_0\frac{d\gamma(t)}{dt} \tag{1.34}$$

The relaxation time for the Maxwell model is defined as $\tau_0 = \eta_0/G_0$. By integrating Eq. (1.34) using an integrating factor, we can write the stress $\sigma(t)$ as:

$$\sigma(t) = \int_{-\infty}^{t} \frac{\eta_0}{\tau_0} e^{\frac{-(t-t')}{\tau_0}} \dot{\gamma}(t')dt' \tag{1.35}$$

Comparing the form of Eq. (1.35) with Eq. (1.16), we identify the relaxation modulus for the Maxwell model as

$$G(t) = \frac{\eta_0}{\tau_0} e^{(-t/\tau_0)} \tag{1.36}$$

Taking Fourier transform of the above equation and multiplying by $i\omega$, we can obtain the real and imaginary parts of the complex modulus for the Maxwell model as well.

$$G'(\omega) = G_0 \frac{\omega^2\tau^2}{1+\omega^2\tau^2} \tag{1.37}$$

$$G''(\omega) = G_0 \frac{\omega\tau}{1+\omega^2\tau^2} \tag{1.38}$$

1.4.2 Kelvin-Voigt model

The Kevin-Voigt model comprises of a Hookean spring and a dashpot similar to the Maxwell model but in a parallel combination of the two mechanical elements. The total stress from

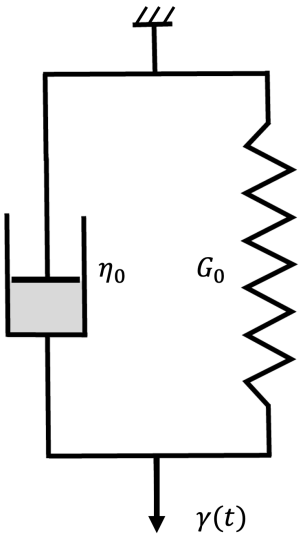

Figure 1-3: Mechanical model representation of Kelvin-Voigt model which corresponds to a combination of spring and dashpot elements in parallel configuration.

the Maxwell model is the summation of the response from the spring and dashpot and the strain or strain rate experienced by both spring and dashpot are equal. Therefore the total stress can be written as

$$\sigma(t) = G_0\gamma(t) + \eta_0\dot{\gamma}(t) \tag{1.39}$$

For an applied oscillatory strain $\gamma(t) = \gamma_0 \sin(\omega t)$, the output stress can be compared with Eq. (1.14) and hence the storage modulus and loss modulus for the Kelvin-Voigt can be

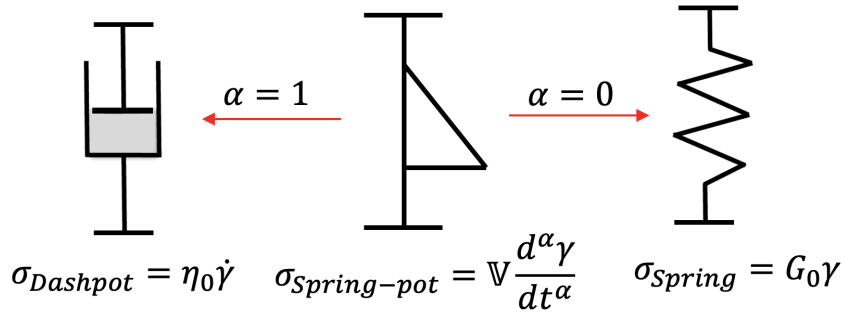

Figure 1-4: The schematic representation of a spring-pot element that interpolates between a Hooken spring $\alpha = 0$ and a dashpot $\alpha = 1$.

obtained as:

$$G'(\omega) = G_0 \tag{1.40}$$

$$G''(\omega) = \eta_0 \omega \tag{1.41}$$

1.4.3 Fractional Maxwell Model

Many complex materials do not follow the simple Maxwell model or Kelvin-Voigt model and hence there has been significant interests in recent years to use a spring-pot element [47, 46], that interpolates between a spring ($\alpha = 0$) and a dasphot ($\alpha = 1$) as shown in Fig. 1-4. The stress response for a single spring-pot can be written using a fractional derivative as:

$$\sigma(t) = \mathbb{V}\frac{d^{\alpha}\gamma}{dt^{\alpha}} \tag{1.42}$$

When the mechanical elements, spring and dashpot in the Maxwell model are both replaced by spring-pot elements, it is known as Fractional Maxwell Model (FMM). This is illustrated in Fig. 1-5. The constitutive equation for the FMM can be written as:

$$\sigma(t) + \frac{\mathbb{V}}{\mathbb{G}}\frac{d^{\alpha-\beta}\sigma(t)}{dt^{\alpha-\beta}} = \mathbb{V}\frac{d^{\alpha}\gamma(t)}{dt^{\alpha}} \tag{1.43}$$

The characteristic relaxation time constant for the Fractional Maxwell Model (FMM) is given by $\tau_0 = \left(\frac{\mathbb{V}}{\mathbb{G}}\right)^{\frac{1}{\alpha-\beta}}$. By applying unit step strain in the Eq. (2.6), one can obtain the

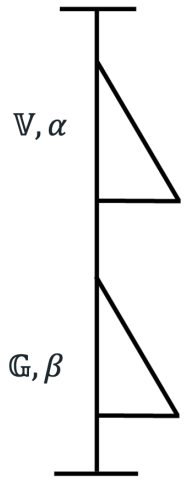

Figure 1-5: The schematic representation of Fractional Maxwell Model (FMM). It comprises of two spring-pots in series configuration and has 4 material properties.

relaxation modulus of the FMM to be

$$G(t) = \mathbb{G}t^{-\beta} E_{\alpha-\beta,\alpha-\beta}\left(-\left(\frac{t}{\tau_0}\right)^{\alpha-\beta}\right) \tag{1.44}$$

where $E_{a,b}(z)$ is the Mittag-Leffler function defined as:

$$E_{a,b}(z) = \sum_{k=0}^{\infty} \frac{z^k}{\Gamma(ak+b)} \tag{1.45}$$

By taking Fourier transform on both sides of the Eq. (2.6), the complex modulus for the FMM can be derived as:

$$G^*(\omega) = \frac{\mathbb{V}(i\omega)^{\alpha}\mathbb{G}(i\omega)^{\beta}}{\mathbb{G}(i\omega)^{\alpha} + \mathbb{V}(i\omega)^{\beta}} \tag{1.46}$$

Two important special cases of the FMM are called Fractional Maxwell Liquid (FML) and Fractional Maxwell Gel (FMG). For, Fractional Maxwell Liquid (FML), the parameter $\alpha = 1$, and the FMM simplifies to a series configuration of spring pot and dashpot. For Fractional Maxwell Gel (FMG), the parameter $\beta = 0$, the FMM simplifies to a series configuration of spring pot and spring in series [47, 81]. If both the parameters α and β are 0 and 1 respectively,, we recover the simple Maxwell model from FMM. The asymptotes

	G'	G''
$\lim_{\omega\to 0}$	$\mathbb{V}\omega^{\alpha}\cos\left(\frac{\pi}{2}\alpha\right)$, if $\alpha \neq 1$	$\mathbb{V}\omega^{\alpha}\sin\left(\frac{\pi}{2}\alpha\right)$, if $\alpha \neq 0$
$\lim_{\omega\to 0}$	$\frac{\mathbb{V}^2}{\mathbb{G}}\omega^{2-\beta}\cos\left(\frac{\pi}{2}\beta\right)$, if $\alpha = 1$	$\mathbb{V}\omega^{\alpha}\sin\left(\frac{\pi}{2}\alpha\right)$, if $\alpha = 0$
$\lim_{\omega\to\infty}$	$\mathbb{G}\omega^{\beta}\cos\left(\frac{\pi}{2}\beta\right)$, if $\beta \neq 1$	$\mathbb{G}\omega^{\beta}\sin\left(\frac{\pi}{2}\beta\right)$, if $\alpha \neq 0$
$\lim_{\omega\to\infty}$	0 $(\forall\omega)$, if $\beta = 1$	$\frac{\mathbb{G}^2}{\mathbb{V}}\omega^{-\alpha}\cos\left(\frac{\pi}{2}\alpha\right)$, if $\alpha = 0$

Table 1.1: Asymptotic behavior of complex modulus of Fractional Maxwell model (FMM) [46].

for FMM in the frequency domain are tabulated in Table 1.1. [46].

1.5 Time-resolved rheology

In the previous sections, we discussed the different shear flows, constitutive equations, material functions and corresponding mechanical models encountered in this thesis. Many complex materials which are of industrial significance undergo various changes in their physical and chemical properties with time. In particular, rheological properties such as complex modulus, viscosity and relaxation modulus can be time dependent even in the limit of small amplitide deformation. This time dependence may arise due to several reasons such as reversible coordinate bonds, and microstructural build up or break down with time. This phenomena of time dependence in rheological properties has been documented for over a century and is often noted as thixotropic or anti-thixotropic behavior. According to Mewis and Wagner [71], *Thixotropy is defined as the continuous decrease of viscosity with time when flow is applied to a sample that has been previously at rest and the subsequent recovery of viscosity in time when the flow is discontinued*. Anti-thixotropic behavior corresponds to the case where there is a continuous increase of viscosity with time when flow is applied and the subsequent decrease of viscosity in time when the flow is discontinued. Some examples of thixotropic fluids are blood, drilling fluids, colloidal gels, etc.

Some thioxtropic fluids are out of thermodynamic equilibrium and their microstructures continuously evolve with time to try and attain minimum free energy even without any initiation of flow or deformation to the material [49, 50]. This phenomena is noted as rheological aging or physical aging and such materials are called soft glassy materials.

Therefore, soft glassy materials show continuously time varying rheological properties due to aging, without any initiation of flow or deformation. Drilling fluids (such as bentonite and laponite dispersion), foams and paints are examples of thixotropic materials that exhibit aging behavior. A number of biopolymer gels like cross-linked Calcium alginate, copper alginate, gelatine and xanthum gum show just thixotropic behavior. It is important to develop experimental and post-processing techniques to obtain time dependent rheological properties in order to better understand and quantify the behavior of thixotropic and aging complex fluids. Materials which show some kind of time dependent rheology can be also referred to as mutating materials in general [74].

For such experiments involving mutating materials, special care should be taken to obtain accurate rheological measurements at any specific fixed time. Therefore, Winter *et. al* [74] defined a 'mutation number' Mu_g to measure the the change in the rheological property g within the duration of the experiment. The mutation number is the ratio of the duration of the experiment Δt to the mutation time λ_{Mu}.

$$Mu_g = \frac{\Delta t}{\lambda_{Mu}} \tag{1.47}$$

The mutation time λ_{Mu} is then defined in terms of the rate of change in the material property as:

$$\lambda_{Mu} = \left[\frac{1}{g}\frac{\partial g}{\partial t}\right]^{-1} \tag{1.48}$$

For measuring the complex modulus at a particular time point, if one sinusoidal signal is used, then the experimental time is $\Delta t = 2\pi/\omega$. Therefore the mutation number can be written as:

$$Mu_g = \frac{\Delta t}{\lambda_{Mu}} = \frac{2\pi}{\omega}\frac{d\ln g}{dt} \tag{1.49}$$

For mutating materials, it has been reported that we require $Mu_g \leq 0.15$ to obtain accurate measurements [74, 18]. In recent years, there have also been significant advances in time resolved rheometry to obtain accurate measurements. Geri *et. al* employed an optimally windowed exponential chirp to rapidly obtain complex modulus across range of frequencies compared to the conventional frequency sweep techniques. The latter comprises of send-

ing a sinusoidal signal input for every frequency of interest [35]. This chirping technique reduces the mutation number for mutating materials and can be used to obtain accurate frequency information for a particular time point.

This chirping technique is relatively new in the field of rheometry and it is important to apply it to better investigate the thixotropic and aging behavior of mutating materials. In this work, we explore the applications of chirps in superposition flows using a biopolymer gel alginate and develop new time-resolved oscillatory rheometric techniques for fast mutating systems. Finally, using these techniques, we investigate and quantify the aging behavior of bentonite clay dispersions which are of high importance to the oil and gas industries.

1.6 Thesis structure

A common method of investigating the relaxation dynamics and microstructural alterations due to large deformations involves orthogonal superposition of a steady shear rate with a small amplitude oscillatory shear while monitoring shear dependent complex modulus. This experimental technique is referred to as orthogonal superpostion rheometry. In chapter 2, we extend this technique to monitor the temporal evolution of the rate dependent complex moduli (orthogonal moduli) for rapidly mutating materials to investigate the microstructural recovery dynamics. This is achieved by superposing several chirp signals in succession together with steady shear flow in orthogonal direction and the procedure is presented using a fast mutating alginate gel. We show using alginate gel, that the method of orthogonal superposition of chirp signal with steady shear flow can replace the conventional orthogonal superposition rheometry freuency sweeps to understand the relaxation dynamics and microstructural alterations at large deformations since it can reduce experimental time without the loss of accuracy in moduli measurements. We then construct the rate dependent relaxation spectrum for the alginate gel from measurements of the orthogonal moduli and explore the creation of shear on detecting flow-induced anisotropy using orthogonal chirp measurements.

The chirp signal can assist in rapidly determining frequency information across a range

of frequencies but still assumes the output response does not change significantly within the chirp period ($Mu_g \leq 0.15$). However, satisfying the constraint $Mu_g \leq 0.15$, can still be challenging for fast mutating systems. Therefore, it is important to develop advanced signal processing techniques to get accurate time resolved frequency information. In chapter 3, we utilize a special case of Short Time Fourier Transform (STFT) called the Gabor transform to extract accurate time-resolved frequency information using a sinusoidal signal input with a specified deformation frequency. We explore the different applications of Gabor transform in rheometry in chapter 3 and we refer to this new rheometry protocol as *Gaborheometry*.

Finally, in chapter 4, we use these time-resolved techniques to investigate and quantify the rheological aging taking place in bentonite dispersions. We conduct a range of experiments such as step strain, chirps, steady shear flow and oscillatory experiments at different age times and temperatures to probe the aging behavior. We model the linear response of 5 wt.% bentonite dispersion using mechanical models and material time domain transformation techniques [14, 49]. This helps us to quantify the slow down of relaxation dynamics, and the slow temporal evolution of the complex modulus as the clay ages and produces progressively more stable structures slowly and continuously with time.

Chapter 2

OrthoChirp: A fast spectro-mechanical probe for monitoring transient microstructural evolution during shear

2.1 Introduction

Many complex materials such as colloidal gels, polymer solutions and melts, fracking fluids which are of high importance to industrial applications undergo flow induced microstructural changes [79, 96, 100, 12]. Therefore, superposition rheometry involving superimposing a small amplitude oscillatory deformation to a unidirectional shear rate has been used to explore the flow induced rheological properties [105, 100, 12, 16]. This technique is used to determine the relaxation mechanism of materials under flow or large deformations [70, 99]. The superposition rheometry is of two types: Parallel superposition, where the oscillatory deformation is applied in the direction of unidirectional shear rate and orthogonal superposition (OSP), where the oscillatory deformation is applied in perpendicular direction to the applied unidirectional shear rate [100]. Parallel superposition and orthogonal superposition have been shown to be fundamentally different experimentally as well as from theoretical predictions [20, 105, 70]. Parallel superposition is more straight forward to execute and has been used to measure the shear induced changes [13]. However,

the strong cross coupling between the two modes of deformation, steady shear and oscillatory deformation can lead to unexpected results and makes the understanding of shear induced changes difficult [105]. Therefore, orthogonal superposition has been preferred to gain insights relating to the flow induced properties of the complex materials. With the advancements in devices for orthogonal superposition [98] and introduction of capabilities of orthogonal superposition measurements in commercial rheometers, there is an increasing interest in understanding the flow induced properties through orthogonal superposition experiments. There have been numerous reports of theoretical predictions and experimental evidence of change in relaxation time and mechanisms due to the applied shear rate or large non-linear deformations [45, 70]. These superposition techniques can also be used to verify the compatibility of the constitutive models [93].

The phenomena of flow induced anisotropy is well known and has been observed in various complex materials [97, 90, 65, 58]. However, measurements of flow induced anisotropy have not been addressed in rheology for a long time. Recently, Colombo et al. in [12], measured the anisotropy in colloidal gels using orthogonal superposition experiments. They made use of the thixotropy of the colloidal gels and measured the evolution of the complex modulus with time in orthogonal and parallel direction of the unidirectional shear rate immediately after the cesseation of shear. The difference in the transient evolution of the moduli in the orthogonal and parallel direction with respect to the previous unidirectonal shear flow direction clearly showed the phenomena of flow induced anisotropy in colloidal gels. However, for complex materials whose mutation time $\tau_{mu} = (\frac{1}{g}\frac{dg}{dt})^{-1}$ (where g is the property of interest [74]) is comparable to the experimental time ΔT, monitoring the transient evolution is challenging. In order to get good estimate of the property of interest, we need the mutation number $N_{mu} = \Delta T/\tau_{mu} << 1$. A conservative inequality to obtain accurate measurements would be $N_{mu} \leq 0.15$ [74, 18]. Therefore we show the full capabilities of optimally windowed chirps (OWCh) developed by Geri et al. [35] in orthogonal superposition rheometry, using a weakly associated physical gel, alginate in this work. We term the experimental protocol of super imposing OWCh deformation orthogonally to the unidirectional shear rate as *Orthochirp*. Apart from the rapid mutation comparable to the time scale of the experiment, these weakly associated physical gels have a modulus recov-

ery time in the order of 10 seconds which makes the utilization of conventional techniques to monitor the evolution of complex modulus more challenging. Optimal windowed chirps introduced by Geri et al. are used to obtain linear complex moduli for various frequencies accurately in rapid time [35]. In this work, we use orthochirp to monitor microstructural evolution during shear and to obtain the shear rate dependent orthogonal complex moduli ($G^*(\omega, \dot{\gamma})$) in quick time. We utilize the rate dependent orthogonal moduli to predict rate dependent spectrum in the orthogonal direction of applied large non-linear deformation (unidirectional shear). Also, we attempt to predict the rate dependent spectrum in the direction of applied large non-linear deformation (unidirectional shear) from the linear relaxation spectra and damping function using the method outlined by Curtis et al. in [16]. The distinction between the rate dependent spectrum in different directions informs us about the flow induced anisotropy in alginate gel and helps us understand the variation of relaxation mechanisms of the alginate gel in different directions under the application of large deformations.

2.2 Experimental method and materials

2.2.1 Material preparation

The 3.5 wt.% sodium alginate solution with water was prepared using the high viscosity alginic acid soldium salt from brown algae purchased from Sigma-Aldrich. To mix water and the alginate salt speed mixer was used. Immediately, after the addition of alginate salt to the water, the sample was mixed at 2000 rpm for 5 minutes. The sample was rolled overnight for swelling and the sample was heated at 60°C for few hours before mixing at 2000 rpm again for 5 minutes.

2.2.2 Orthogonal superposition setup and coordinate system

The oscillatory chirp motion perpendicular to the main flow direction was implemented by modifying an ARES-G2 rheometer (TA Instruments, Newcastle, Delaware, USA). An orthogonal chirp strain deformation in axial direction perpendicular to the steady shear

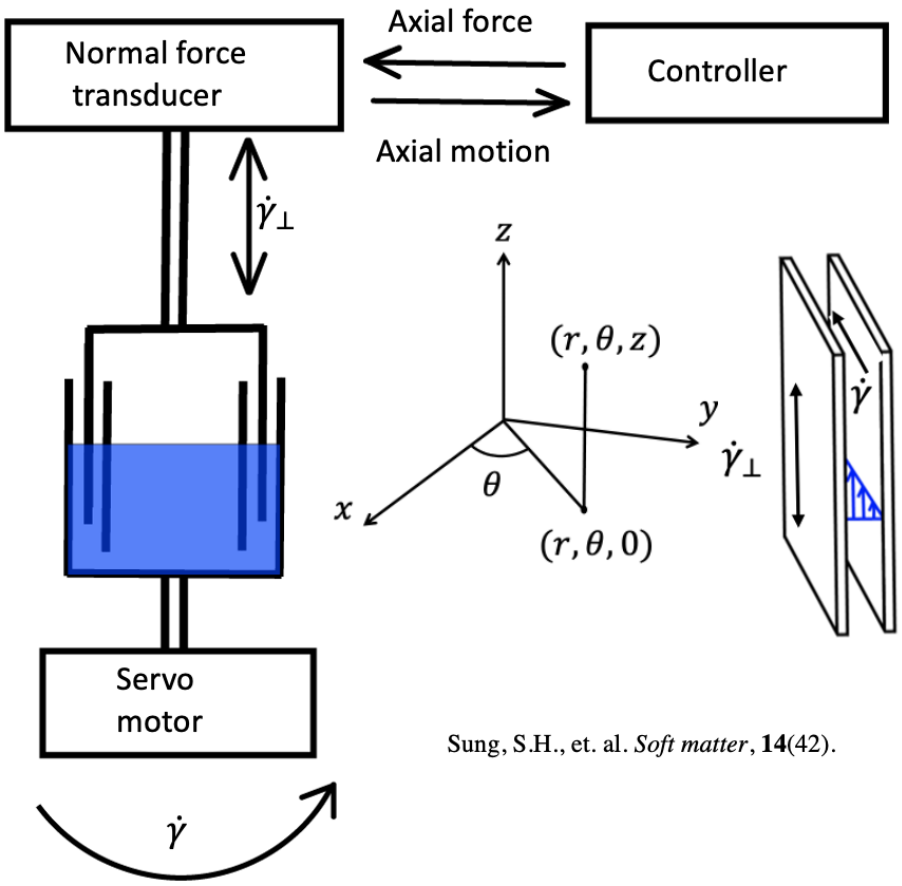

Sung, S.H., et. al. *Soft matter*, **14**(42).

Figure 2-1: Orthognal superposition setup for a double wall Couette cell. Small amplitude chirp is imposed in the axial direction, perpendicular to the direction of unidirectional shear rate in the azimuthal direction. Figure modified from [91]

flow in azimuthal direction was achieved by using a double wall Couette geometry. An oscillatory chirp shear strain deformation was applied by moving a hollow bob axially, whereas the tangential steady shear flow is obtained by rotating the double-walled Couette cup. The schematic figure of the orthogonal superposition setup is illustrated in Fig. 2-1. The details in constructing the orthogonal superposition set up are detailed in [91, 56]. According to the cylindrical coordinate system chosen and represented in Fig. 2-1, the axial direction in which the chirp strain signal is applied is rz direction. Similarly, the azimuthal direction in which the non-linear steady shear rate is applied is in the $r\theta$ direction.

2.3 Optimally windowed Chirps for Orthogonal Superposition

2.3.1 Introduction to Chirps

The Optimally Windowed Chirp introduced by Geri et al. employs a cosine tapered function called as Tukey window to a fast exponential chirp signal in order to maximize the signal to noise ratio [35]. The purpose of such windowing are mainly two fold: (i) to reduce the presence of side lobes in the frequency spectrum. The DFT of an exponential chirps (without any window) is equivalent to taking DFT of the product of a rectangular window and an exponential chirp. In the frequency space, this results in the convolution between a DFT of a chirp signal and a sinc type function ($\sin x/x$) which effects in oscillation of the frequency information contained in the chirp data (side lobes). (ii) to reduce the spectral leakage. The spectral leakage happens if periodicity of the signal is not satisfied. Periodicity requires the initial value and final value of the chirp signal to be the same ($x(0) = x(T)$). Windowing technique which is responsible for amplitude modulation aids in addressing these two important challenges in using a frequency modulated chirps to obtain

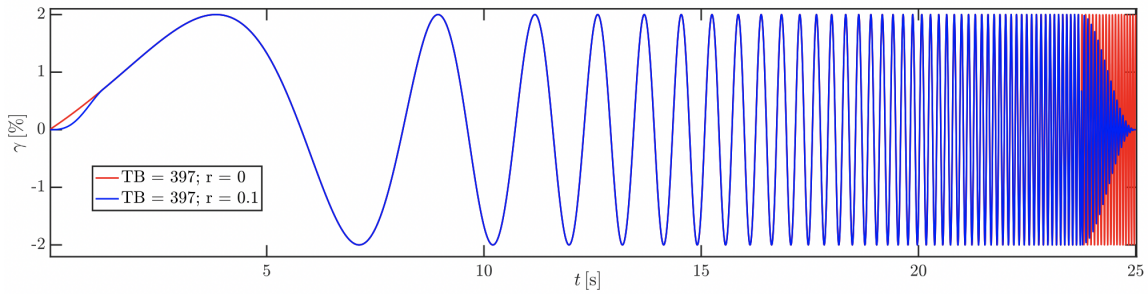

Figure 2-2: Optimally Windowed Chirp (OWCh) signals with $\omega_1 = 0.25$ rad/s, $\omega_2 = 100$ rad/s, $T = 25$ s and time bandwidth product $TB = T(\omega_2 - \omega_1)/2\pi = 397$. Red solid line represents the chirp with $r = 0$ and $\gamma_0 = 2\%$. Blue solid line represents the chirp with $r = 0.1$ and $\gamma_0 = 2\%$.

accurate data rapidly [41].

$$\gamma(t) = \gamma_0 \begin{cases} \cos^2[\frac{\pi}{r}(\frac{t}{T} - \frac{r}{2})] \sin\left[\frac{\omega_1 T}{\log(\omega_2/\omega_1)}[\exp(\log(\omega_2/\omega_1)\frac{t}{T}) - 1]\right] & \frac{t}{T} \leq \frac{r}{2} \\ \sin\left[\frac{\omega_1 T}{\log(\omega_2/\omega_1)}[\exp(\log(\omega_2/\omega_1)\frac{t}{T}) - 1]\right] & \frac{r}{2} < \frac{t}{T} < 1 - \frac{r}{2} \\ \cos^2[\frac{\pi}{r}(\frac{t}{T} - 1 + \frac{r}{2})] \sin\left[\frac{\omega_1 T}{\log(\omega_2/\omega_1)}[\exp(\log(\omega_2/\omega_1)\frac{t}{T}) - 1]\right] & \frac{t}{T} \geq 1 - \frac{r}{2} \end{cases} \tag{2.1}$$

Optimally Windowed Chirp (OWCh) is expressed in Eq. (2.2) where T is the duration of the signal and γ_0 is the amplitude of the signal $\gamma(t)$. The lowest and the highest frequencies of this chirp are ω_1 and ω_2 respectively. The window tapering parameter r regulates the amplitude modulation for the signal of time duration T. The time bandwidth of the signal is defined as $TB = T(\omega_2 - \omega_1)/(2\pi)$. Fig. 2-2 shows the plot of a chirp signal for a fixed time bandwidth and two different tapering parameters. The window tapering parameter $r = 0$ corresponds to the rectangular window and the tapering parameter $r = 1$ represents the Hann window. As the tapering parameter r increases, the amplitude modulation of the exponential chirp signal increases. Fig. 2-3 shows the spectrum of the chirp signal at different tapering parameters.

The amplitude spectrum follows a pink spectrum as the amplitude spectrum decreases as the square root of the frequency ($\omega^{-1/2}$). The ripples observed in Fig. 2-3 indicates the presence of side lobes for $r = 0$ (rectangular window). Windowing also reduces the contribution in frequency spectrum in both ends of the frequency regime. Geri *et al.* also

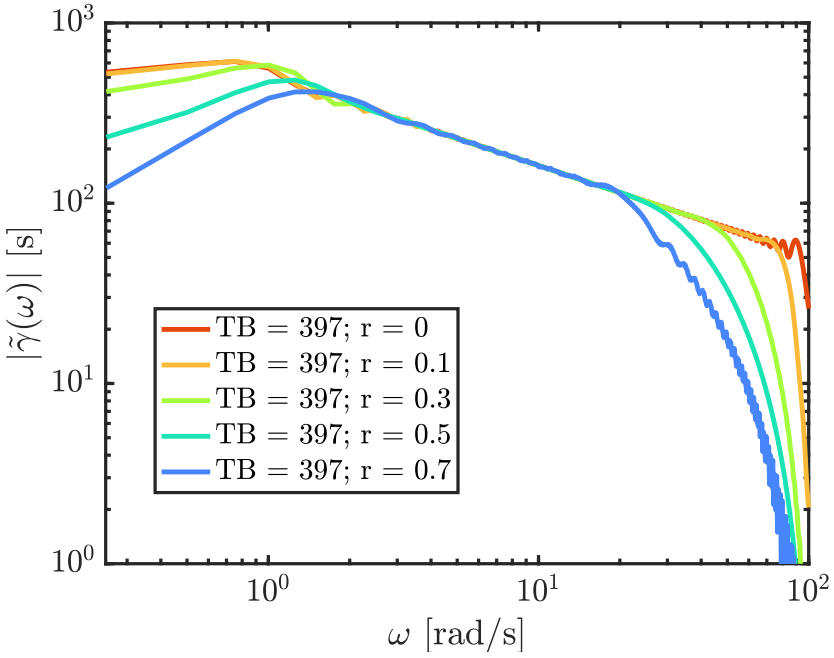

Figure 2-3: The amplitude spectrum of the Optimally Windowed Chirp (OWCh) constructed by $\omega_1 = 0.25$ rad/s, $\omega_2 = 100$ rad/s, $T = 25$ s and time bandwidth product $TB = T(\omega_2 - \omega_1)/2\pi = 397$ of for different values of r.

showed using numerical and experimental investigations, the optimal cosine tapered window needed to modulate the amplitude of the chirp signal is around 10% of the length of the chirp signal ($r = 0.1$). Therefore, Optimally Windowed Chirp signal with $r = 0.1$ has been used in this work for all of the following experiments.

2.3.2 Orthochirp inputs

The orthogonal input chirp deformation strain signal in the axial (rz) direction can therefore be written as:

$$\gamma_{rz}(t) = \gamma_0 \begin{cases} \cos^2[\frac{\pi}{r}(\frac{t}{T} - \frac{r}{2})] \sin\left[\frac{\omega_1 T}{\log(\omega_2/\omega_1)}[\exp(\log(\omega_2/\omega_1)\frac{t}{T}) - 1]\right] & \frac{t}{T} \leq \frac{r}{2} \\ \sin\left[\frac{\omega_1 T}{\log(\omega_2/\omega_1)}[\exp(\log(\omega_2/\omega_1)\frac{t}{T}) - 1]\right] & \frac{r}{2} < \frac{t}{T} < 1 - \frac{r}{2} \\ \cos^2[\frac{\pi}{r}(\frac{t}{T} - 1 + \frac{r}{2})] \sin\left[\frac{\omega_1 T}{\log(\omega_2/\omega_1)}[\exp(\log(\omega_2/\omega_1)\frac{t}{T}) - 1]\right] & \frac{t}{T} \geq 1 - \frac{r}{2} \end{cases} \tag{2.2}$$

The parameters of the orthogonal input chirp applied in the present study are taken to be: initial frequency $\omega_1 = 0.25$ rad/s, final frequency $\omega_2 = 100$ rad/s, chirp duration $T = 25$ s, time bandwidth product $TB = T(\omega_2 - \omega_1)/2\pi = 397$ and tapering parameter $r = 0.1$. The steady shear rate applied in the azimuthal direction is represented as:

$$\dot{\gamma}_{r\theta} = \dot{\gamma} \tag{2.3}$$

where $\dot{\gamma}$ is a constant value of the shear rate that is applied. The complex modulus under the orthogonal superposition of shear rate $\dot{\gamma}$ is represented by $G^*_\perp(\omega, \dot{\gamma})$. The complex modulus for different shear rates are obtained using orthochirp and we study the effects of shear rates to the material relaxation dynamics from the non-linear orthogonal rheological data.

2.3.3 Results from orthochirp

No orthogonal shear- Critical gel

First, the complex moduli without any shear superposition is measured for 3.5 wt.% alginate solution by orthogonal chirping in axial (rz) direction and is compared with the complex modulus obtained from the conventional discrete frequency sweep (DFS) from torque transducer ($r\theta$ direction) as shown in Fig. 2-4. The complex modulus data obtained from two different experimental methods are in good agreement with each other which shows that the conventional technique of superposing SAOS with steady shear rate can be replaced by orthochirp. There is a spike around $\omega = 20$ rad/s in orthochirp data due to the resonance with the axial force transducer. The complex modulus data of alginate without any shear rate superposition is a critical gel since the phase $\tan\delta = G''/G'$ remains constant with frequency. The obtained linear complex modulus of alginate is modeled using the critical gel model introduced by Winter [103].

$$G'(\omega) = S\Gamma(1-n)\cos(n\pi/2)\omega^n \tag{2.4}$$

$$G''(\omega) = S\Gamma(1-n)\sin(n\pi/2)\omega^n \tag{2.5}$$

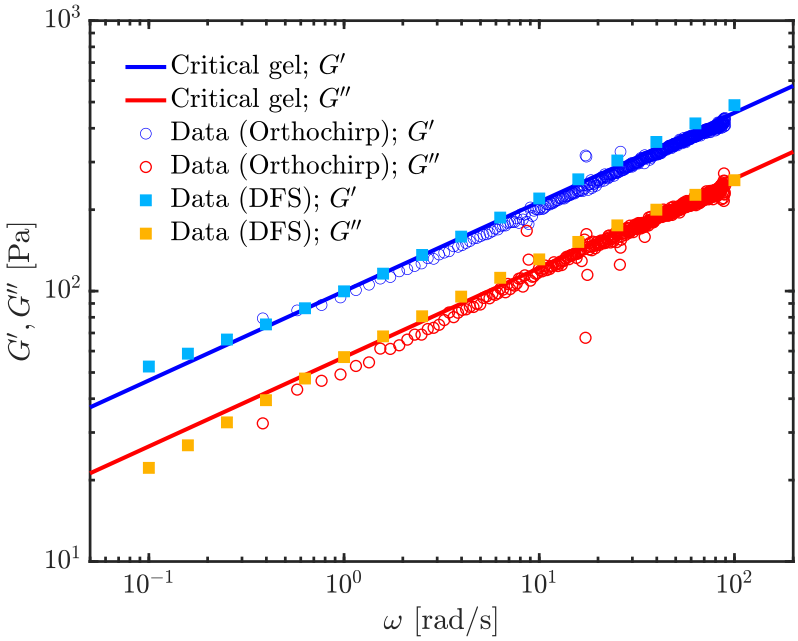

Figure 2-4: Comparison of G' & G'' obtained from chirping (T = 25 s, ω_1 = 0.25 rad/s, ω_2 = 100 rad/s, γ_0 = 2%) in the axial direction with no orthogonal shear rate ($\dot{\gamma}$ = 0 s^{-1}) with the data obtained from traditional SAOS experiments (input strain amplitude: 2%). The solid lines represent the critical gel model introduced by Winter fit indicating the alginate gel is a critical gel when no shear rate is imposed.

where S is the gel strength of the material with units of Pa·s^{-n} and n is the powerlaw relaxation exponent of the gel. For 3.5 wt.% alginate system, we find S = 85.3 Pa·s^{-n} and n = 0.33 as shown in Fig. 2-4.

With Orthogonal shear

Now, rate dependent experiments are carried out using orthochirps of time duration T = 25s, lowest frequency ω_1 = 0.25 rad/s, highest frequency ω_2 = 100 rad/s, strain amplitude γ_0 = 5% and tapering parameter r = 0.1. This chirp enables us to capture the orthogonal complex moduli data for almost three decades of frequency. A range of unidirectional shear rates ($\dot{\gamma}$ = 0 s^{-1}, 0.05 s^{-1}, 0.1 s^{-1}, 0.5 s^{-1}, 1 s^{-1}, 5 s^{-1}, 10 s^{-1}, 15 s^{-1}, 35 s^{-1}, 50 s^{-1}, 100 s^{-1}) are applied and the correspondent orthogonal complex modulus results are shown in Fig. 2-5. Both the orthogonal storage and loss modulus decreases as there is an increase in the applied perpendicular unidirectional shear rate. This is attributed to the

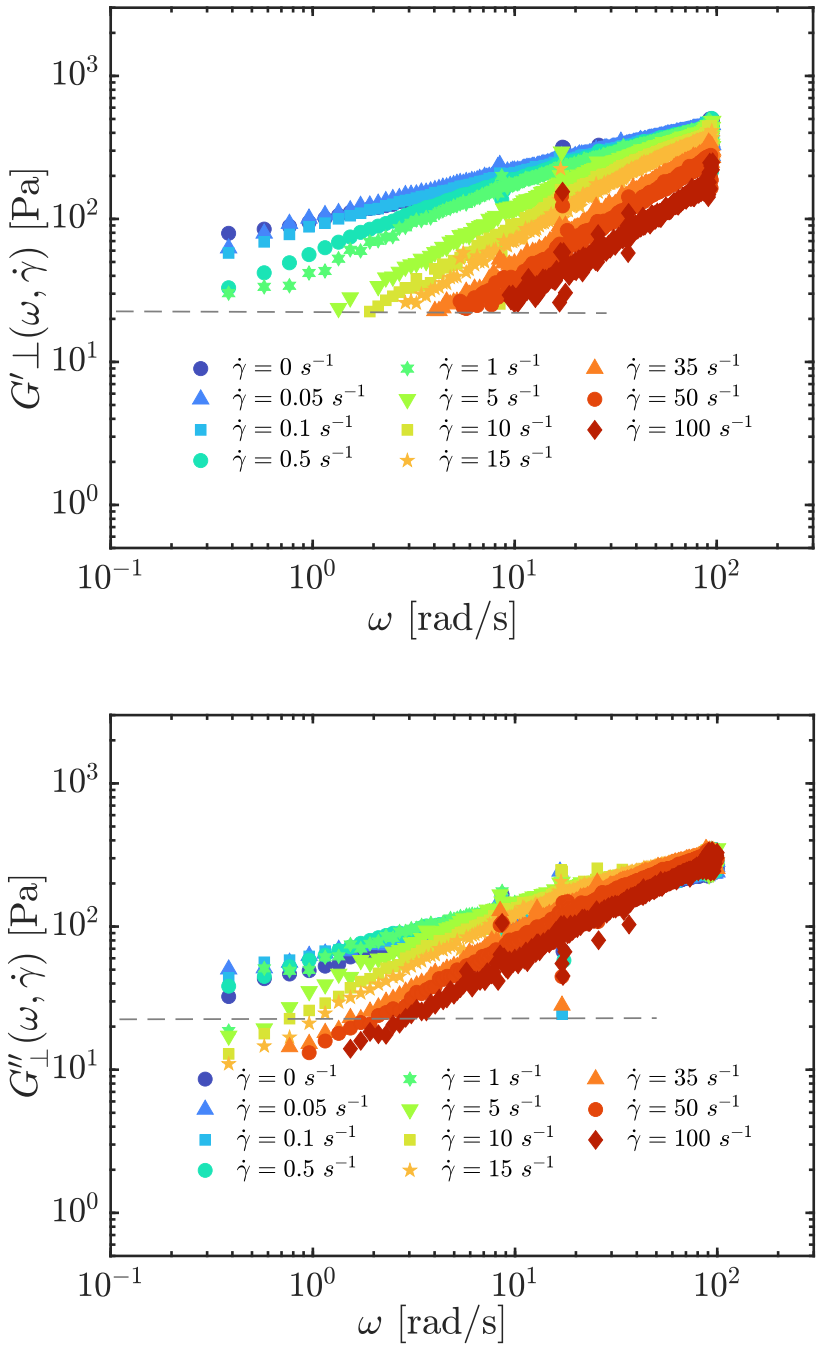

Figure 2-5: $G'_\perp(\omega,\dot{\gamma})$ & $G''_\perp(\omega,\dot{\gamma})$ obtained from imposing orthochirp on a unidirectional shear rate. The grey solid line shows the low torque resolution limit of the instrument.

breakdown of micro structure of the alginate gel as the shear rate increases. The application of unidirectional shear rate affects the gel structure and strong deviation from critical gel is observed. The resolution limit of the instrument limits the measurement of the modulus below 20 Pa and this restricts us to obtain data below 20 Pa.

Repeated Chirps for moduli recovery

To observe the moduli recovery for different frequencies, immediately after cessation of unidirectional shear rate $\dot{\gamma} = 10\ s^{-1}$, continuous chirps of duration $T = 6.25\ s$, lowest frequency $\omega_1 = 1\ rad/s$, highest frequency $\omega_2 = 100\ rad/s$, wait time $t_w = 1\ s$, strain amplitude $\gamma_0 = 2\%$ and tapering parameter $r = 0.1$ are applied repeatedly for 600 s as shown in Fig. 2-6. It is clear from Fig. 2-6, that the unidirectional shear effects are felt for the first 15 seconds as the results from the first two chirp signals be consistent with the orthogonal moduli data at unidirectional shear rate of $\dot{\gamma} = 10\ s^{-1}$ $\left(G'_{\perp}\left(\omega, \dot{\gamma} = 10 s^{-1}\right)\right)$. We observe the transient recovery state at around $t = 21\ s$ from the orthogonal complex modulus response of input chirp signal applied between the time $t = 14.5\ s$ to $t = 21.75\ s$ (third chirp from the continuous chirp signals applied for 600 s). The moduli for all frequencies are completely recovered at $t = 28\ s$ as seen from the orthogonal modulus response of input chirp signal applied between the time $t = 21.75\ s$ to $t = 28\ s$. The overlap of data obtained at $t = 100\ s$ and $t = 600\ s$ indicates that the microstructure of the material is recovered and no longer evolves with time. It is clear that the shear effects are no longer felt since there is no progressive evolution of complex modulus with time. From here, we can deduce that for the alginate gel used here, it takes around 28 s, to recover the complete microstructure when altered by large deformations. The changes in such small timescales for these fast mutating systems were previously difficult to extract. But with this new orthochirp technique, it is feasible to monitor changes in response of the material. For three values of angular frequency $\omega = 10, 30, 50\ rad/s$, we plot the value of the complex modulus obtained from every chirp signal against its corresponding time in Fig. 3-5. This illustrates the evolution for the moduli for $\omega = 10, 30, 50\ rad/s$ after the cessation of unidirectional shear rate $\dot{\gamma} = 10\ s^{-1}$. It is clear from Fig. 3-5 that the microstructure of the alginate is reduced by shear rate resulting in reduction of storage

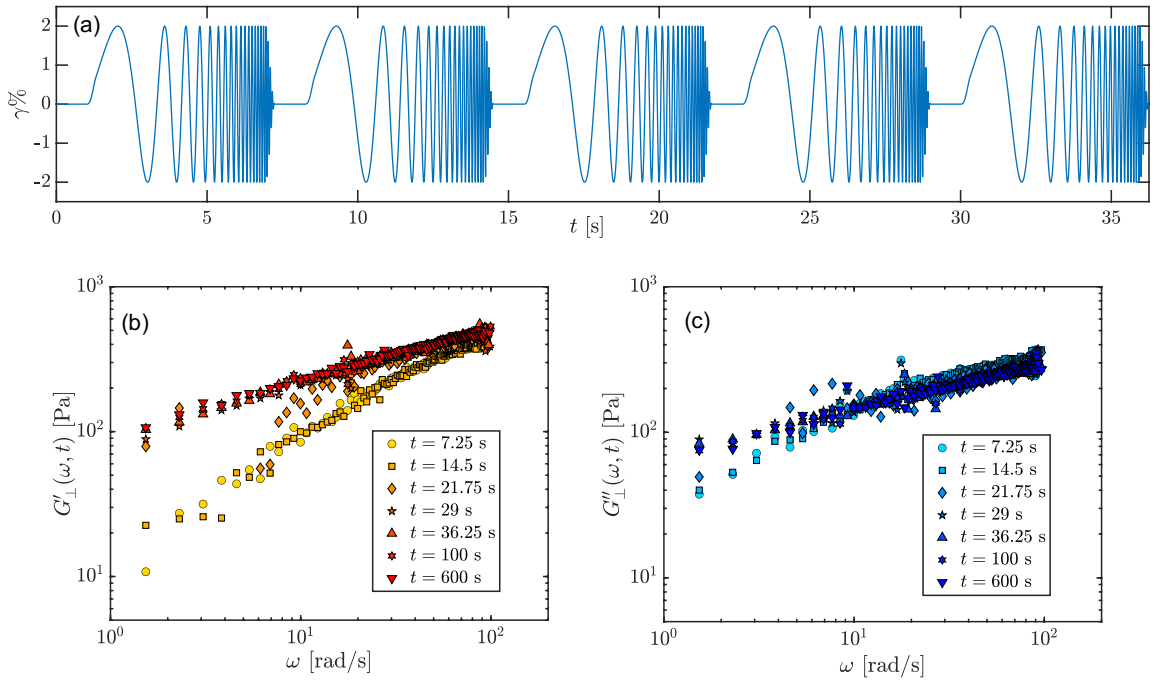

Figure 2-6: (a)A 6.25 *s* chirp is imposed with 1 *s* wait time (t_w) repeatedly for 600 *s* in order to track the recovery of the complex modulus with time for all different frequencies. For visual purpose the input signal shown in (a) is stopped at 36 *s*. (b) Recovery of storage modulus $G'_\perp$ with time after the cessation of shear at $t = 0$ s. (c) Recovery of loss modulus against time after the cessation of shear.

modulus. The microstructure is rapidly reconstructed in 28 s resulting in recovery of the storage modulus.

2.4 Orthogonal Superposition- Constitutive equations and modeling

2.4.1 Fractional Maxwell modeling of the OSP moduli

To understand the rate dependent orthogonal moduli data better, we consider modeling using spring-pot elements introduced in 1.4.3. The Fractional Maxwell Model (FMM) used by Jaishankar *et al.* [46] for describing the multiscale complex fluids is represented by two spring pots in series where the total stress of the system is the summation of response from

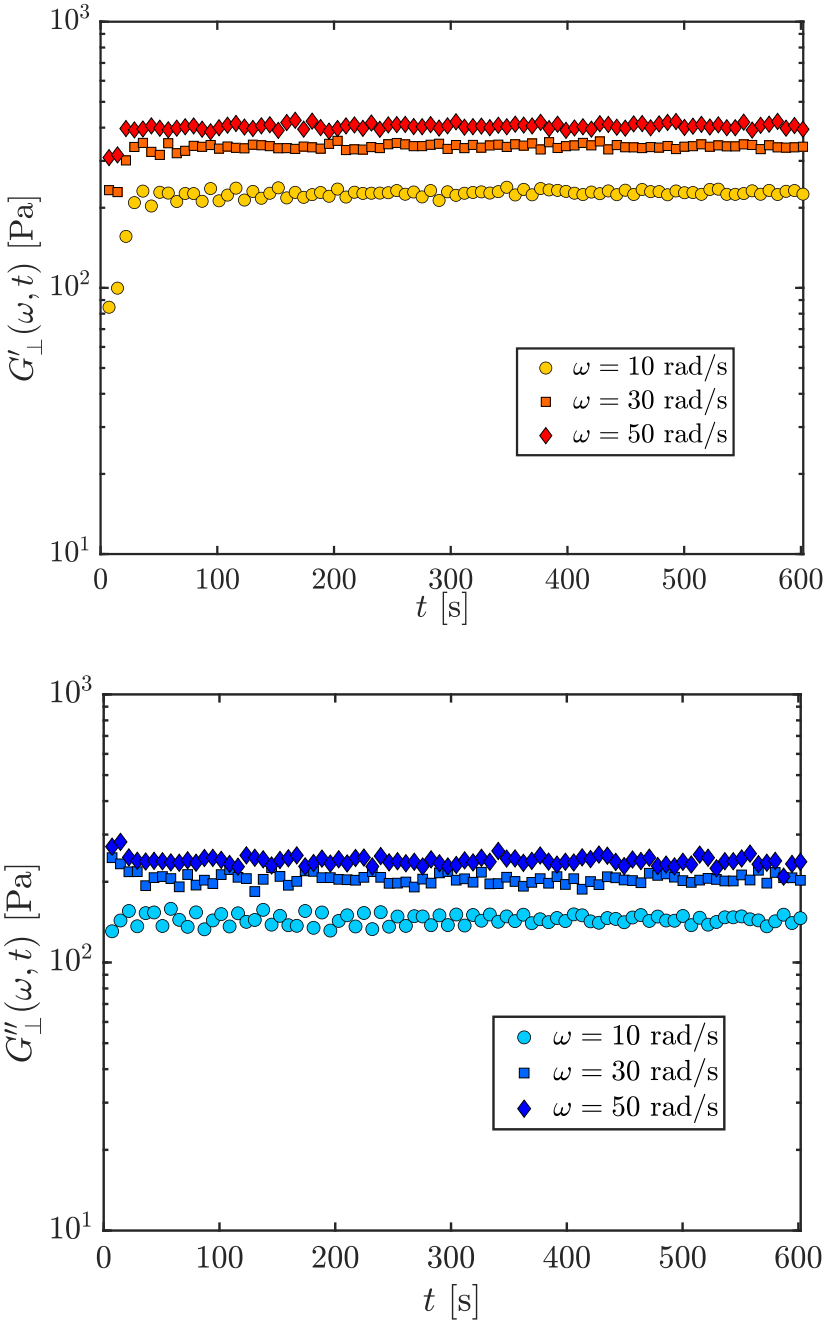

Figure 2-7: Evolution extracted from storage modulus and loss modulus with time is shown for three different frequencies. The modulus recovery time can be noted as around 28 s when the microstructure is reduced by a shear rate of 10 s^{-1}

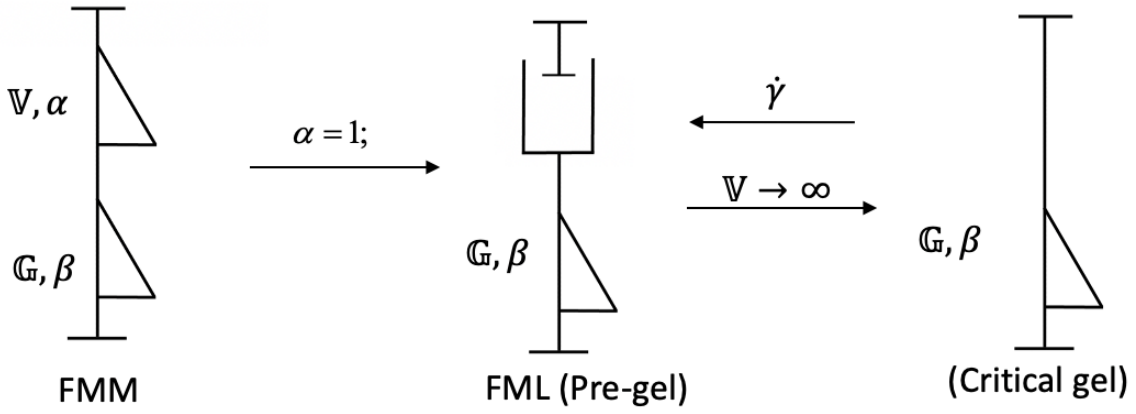

Figure 2-8: Mechanical model of Fractional Maxwell model at different limits.

each spring pots.

$$\sigma(t) + \frac{\mathbb{V}}{\mathbb{G}} \frac{d^{\alpha-\beta}\sigma(t)}{dt^{\alpha-\beta}} = \mathbb{V} \frac{d^{\alpha}\gamma(t)}{dt^{\alpha}} \tag{2.6}$$

The parameters α and β both need to obey the requirement $0 \leq \beta \leq \alpha < 1$ to be thermodynamically compliant. The special case of $\alpha = 1$ and $\beta = 0$ simplifies to the single mode linear Maxwell equation which is a series of a dashpot and a spring with $\mathbb{V}$ and $\mathbb{G}$ translating to viscosity η and spring modulus G respectively. We further simplify the Fractional Maxwell model by constraining the parameter $\alpha = 1$. It is interesting to note that the zero shear-rate viscosity η_0, which is a material function is equal to the model parameter $\mathbb{V}$ when $\alpha = 1$ [47]. This simplified three parameter model is known as the Fractional Maxwell Liquid (FML) and is used for the rheological modeling of complex fluids in pre-gel state [81]. Fractional Maxwell Liquid mechanically translates to a series of dash-pot and a spring pot [81]. For FML, Eq. (2.6) reduces to

$$\sigma(t) + \frac{\mathbb{V}}{\mathbb{G}} \frac{d^{1-\beta}\sigma(t)}{dt^{1-\beta}} = \mathbb{V} \frac{d\gamma(t)}{dt} \tag{2.7}$$

Following the procedure by [46], the relaxation modulus calculated from step strain for FML model can be derived as:

$$G(t) = \mathbb{G} t^{-\beta} E_{1-\beta,1-\beta}\left(-\left(\frac{t}{\lambda}\right)^{1-\beta}\right) \tag{2.8}$$

where the characteristic relaxation time constant for the FML model: $\lambda = (\mathbb{V}/\mathbb{G})^{1/1-\beta}$. The Fourier transform of Eq. (2.7) is taken to obtain the storage modulus and loss modulus.

$$\frac{G'(\omega)}{\mathbb{G}\lambda^{-\beta}} = \frac{(\omega\lambda)^{2-\beta}\cos\left(\frac{\pi\beta}{2}\right)}{(\omega\lambda)^{2(1-\beta)} + 2(\omega\lambda)^{1-\beta}\cos\left(\frac{\pi(1-\beta)}{2}\right) + 1} \tag{2.9}$$

$$\frac{G''(\omega)}{\mathbb{G}\lambda^{-\beta}} = \frac{\omega\lambda + (\omega\lambda)^{2-\beta}\sin\left(\frac{\pi\beta}{2}\right)}{(\omega\lambda)^{2(1-\beta)} + 2(\omega\lambda)^{1-\beta}\cos\left(\frac{\pi(1-\beta)}{2}\right) + 1} \tag{2.10}$$

The relaxation spectrum for FML model as converted by Sadman et al. [81] to FML form following the derivation of Palade et al. [78] for fractional model using Tschoegl's method of Stieltjes integrals [94] is:

$$H_0(\tau) = \frac{1}{\pi}\frac{\mathbb{V}\tau^{-1}\sin(\pi\beta)}{(\mathbb{V}/\mathbb{G})\tau^{\beta-1} + (\mathbb{G}/\mathbb{V})\tau^{1-\beta} + 2\cos(\pi(1-\beta))} \tag{2.11}$$

For shorter relaxation times $\tau \ll \lambda$, the linear relaxation spectrum follows:

$$H_0(\tau) = \frac{\mathbb{G}\sin(\pi\beta)}{\pi}\tau^{-\beta} \tag{2.12}$$

and for longer relaxation times $\tau \gg \lambda$, the linear spectrum follows:

$$H_0(\tau) = \frac{\mathbb{V}^2\sin(\pi\beta)}{\pi\mathbb{G}}\tau^{-(2-\beta)} \tag{2.13}$$

To represent critical gels whose phase (G''/G') is constant with frequency using FML model, the parameter $\mathbb{V}$ is set to diverge to infinity. This reduces the relaxation modulus and spectrum of FML model to a single power-law behavior which is to be expected for critical gels.

$$G(t) = \frac{\mathbb{G}}{\Gamma(1-\beta)}t^{-\beta} \tag{2.14}$$

$$H(\tau) = \frac{\mathbb{G}\sin(\pi\beta)}{\pi}\tau^{-\beta} \tag{2.15}$$

Fig. 2-8 depicts the elements of the mechanical model for Fractional Maxwell Model

(FMM), simplified three parameter model Fractional Maxwell Liquid (FML) which captures the behavior of complex fluids in pregel state and the even simplified model which is just represented by a spring-pot. Comparing the critical gel model obtained from the fractional Maxwell model with critical gel model by Winter, we observe that $\frac{\mathbb{G}}{\Gamma(1-\beta)}$ is equivalent to S, the gel strength of the critical gel in Winter's model. The power-law decay exponent β of the relaxation modulus and the spectrum of the critical gel is equivalent to n in critical gel model introduced by Winter [103]. The FML storage modulus and the loss model for a critical gel ($\mathbb{V} \to \infty$) evaluates to

$$G'(\omega) = \mathbb{G}\cos\left(\frac{\pi\beta}{2}\right)\omega^{\beta} \tag{2.16}$$

$$G''(\omega) = \mathbb{G}\sin\left(\frac{\pi\beta}{2}\right)\omega^{\beta} \tag{2.17}$$

Therefore, the complex viscosity is given by

$$\eta^*(\omega) = \frac{\sqrt{G'(\omega)^2 + G''(\omega)^2}}{\omega} = \mathbb{G}\omega^{\beta-1} \tag{2.18}$$

As discussed in 2.3.3, the alginate system behaves like a critical gel under applications of no large deformations or applied unidirectional shear rates. The application of large deformation or unidirectional shear rate aids in the structural breakdown of the gel structure altering the alginate to a pre-gel state as seen in Fig. 2-5. Therefore, we model the orthogonal superposition modulus for different unidirectional shear rates plotted in Fig. 2-5 using Fractional Maxwell Liquid (FML) model. We plot the parameters of FML model needed for fitting the orthogonal moduli for different shear rates in Fig. 2-9. We observe that the parameters $\mathbb{G}, \beta$ for modeling the orthogonal complex modulus are constant for different unidirectional shear rates. However, the characteristic relaxation time constant of the FML model for fitting the orthogonal complex modulus data changes with the imposed shear rate ($\lambda(\dot{\gamma})$). This indicates that the relaxation time of the material changes when there is an applied shear rate while the gel strength and the exponent of relaxation spectrum for smaller relaxation modes remains the same with shear rate.

From the Fig. 2-9, the FML parameters $\mathbb{G} = 151$ Pa$\cdot\ s^{0.33}$ and $\beta = 0.33$ are constant

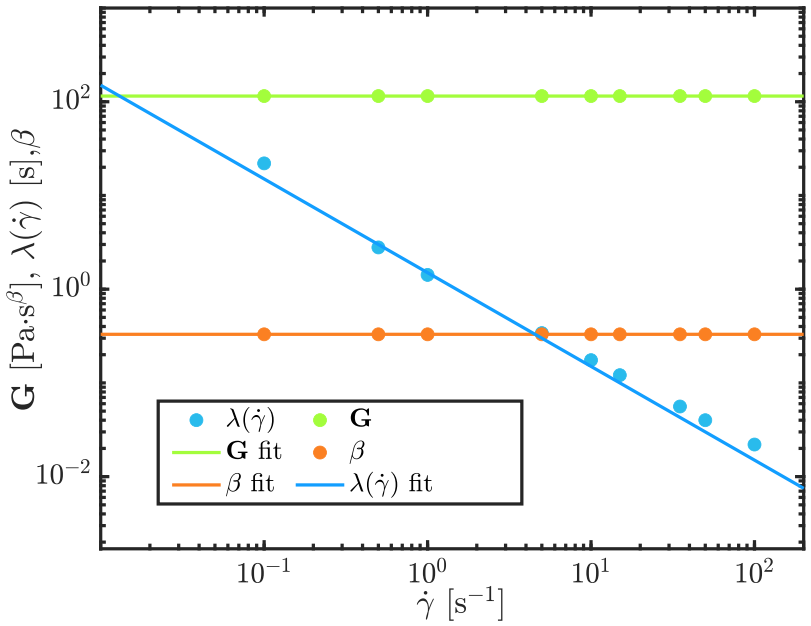

Figure 2-9: The evolution of fractional Maxwell liquid parameters with superposed shear rates for 3.5 wt.% alginate. $\mathbb{G} = 151$ Pa·s$^{0.33}$ and $\beta = 0.33$ are constant with shear rates, whereas the characteristic relaxation time is inversely proportional to the superposed shear rate $\left(\lambda(\dot\gamma) = \frac{1.5}{\dot\gamma}\right)$.

with shear rate, whereas the characteristic relaxation time of the FML model changes as $\lambda(\dot\gamma) = \frac{1.5}{\dot\gamma}$. Hence, the rate dependent orthogonal modulus modeled by FML for different superimposed shear rates can be expressed as:

$$\frac{G'_\perp(\omega,\dot\gamma)}{\mathbb{G}\lambda(\dot\gamma)^{-\beta}} = \frac{(\omega\lambda(\dot\gamma))^{2-\beta}\cos(\frac{\pi\beta}{2})}{(\omega\lambda(\dot\gamma))^{2(1-\beta)} + 2(\omega\lambda(\dot\gamma))^{1-\beta}\cos(\frac{\pi(1-\beta)}{2}) + 1} \tag{2.19}$$

$$\frac{G''_\perp(\omega,\dot\gamma)}{\mathbb{G}\lambda(\dot\gamma)^{-\beta}} = \frac{\omega\lambda(\dot\gamma) + (\omega\lambda(\dot\gamma))^{2-\beta}\sin(\frac{\pi\beta}{2})}{(\omega\lambda(\dot\gamma))^{2(1-\beta)} + 2(\omega\lambda)^{1-\beta}\cos(\frac{\pi(1-\beta)}{2}) + 1} \tag{2.20}$$

2.4.2 Lodge-type constitutive equations for OSP

The most commonly used constitutive equation for orthogonal superposition is the Lodge type model proposed by [105] written in terms of relaxation spectrum, which is dependent on rate of deformation tensor. Using the Lodge type model, the stress tensor $\boldsymbol{\sigma}(t)$ for an

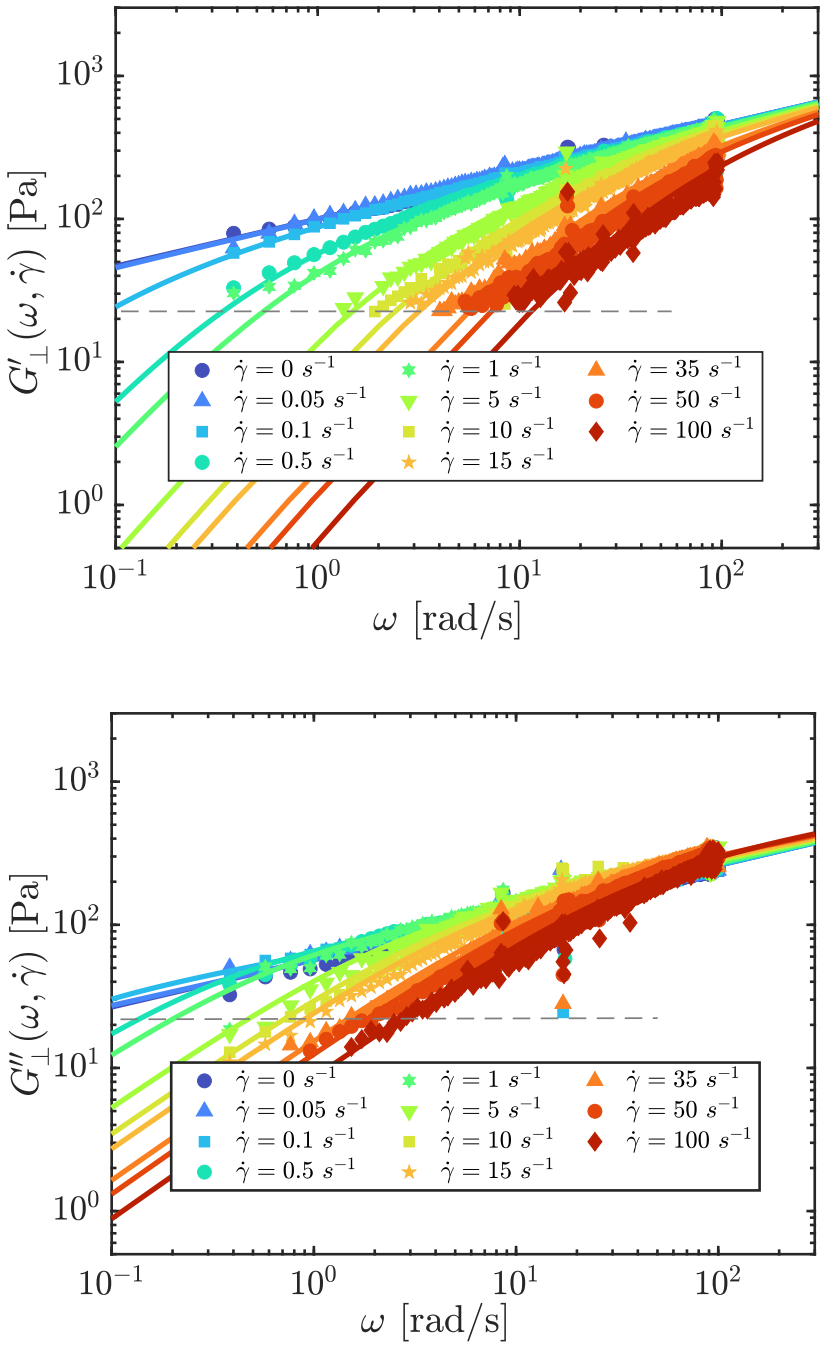

Figure 2-10: $G'_\perp(\omega,\dot{\gamma})$ & $G''_\perp(\omega,\dot{\gamma})$ obtained from imposing orthochirp on a unidirectional shear rate. The grey solid line shows the low torque resolution limit of the instrument.

isotropic complex fluids can be expressed as:

$$\boldsymbol{\sigma}(t) = -p\boldsymbol{I} + \int_{-\infty}^{t}\int_{-\infty}^{\infty} \frac{H(\tau, II_{2\dot{\gamma}})}{\tau} \exp\left(-\frac{(t-t')}{\tau}\right) d\ln\tau[\boldsymbol{C^{-1}} - \boldsymbol{I}]dt' \tag{2.21}$$

where $H(\tau, II_{2\dot{\gamma}})$ is the rate-dependent relaxation spectrum. $II_{2\dot{\gamma}}$ is the second invariant of the rate of deformation tensor $\dot{\boldsymbol{\gamma}}$. We follow the convention used by [100] and [17] and define $II_{2\dot{\gamma}} = \frac{1}{2}tr\left[(2\dot{\boldsymbol{\gamma}})^2\right]$. In Eq. [2.21], $\boldsymbol{C^{-1}}$ is the Finger strain tensor and $\boldsymbol{I}$ is the identity matrix. The rate of deformation tensor is given by

$$\dot{\boldsymbol{\gamma}} = \overrightarrow{\nabla}\boldsymbol{v} + \overrightarrow{\nabla}\boldsymbol{v}^T \tag{2.22}$$

For steady shear flow, the second invariant of rate of deformation tensor becomes:

$$II_{2\dot{\gamma}} = \dot{\gamma}^2 \tag{2.23}$$

When a small amplitude deformation is superimposed in the orthogonal direction (γ_{rz}) with amplitude γ_0 to the steady shear ($\dot{\gamma}_{r\theta} = \dot{\gamma}$), the second invariant of rate of deformation gets modified as:

$$II_{2\dot{\gamma}} = \dot{\gamma}^2 + O(\gamma_0^2) \tag{2.24}$$

The contribution from the deformation in rz direction is negligibly small and hence the rate dependent relaxation spectrum for small amplitude OSP can be expressed as:

$$H(\tau, II_{2\dot{\gamma}}) = H(\tau, \dot{\gamma}^2) \tag{2.25}$$

Therefore, the shear stress σ_{rz} and $\sigma_{r\theta}$ for OSP can be written as:

$$\sigma_{rz}(t) = \int_{-\infty}^{t}\int_{-\infty}^{\infty} \frac{H_{rz}(\tau, \dot{\gamma})}{\tau} \exp\left(-\frac{(t-t')}{\tau}\right) d\ln\tau\ \gamma_{rz}(t, t')dt' \tag{2.26}$$

$$\sigma_{r\theta}(t) = \int_{-\infty}^{t}\int_{-\infty}^{\infty} \frac{H_{r\theta}(\tau, \dot{\gamma})}{\tau} \exp\left(-\frac{(t-t')}{\tau}\right) d\ln\tau\ \gamma_{r\theta}(t, t')dt' \tag{2.27}$$

In Eq. (2.26), the rate dependent relaxation spectrum is noted as H_{rz} for clarity indicating that the rate dependent relaxation spectrum is measured from output stress response σ_{rz} in axial direction, perpendicular to the unidirectional flow or large deformation. Similarly, In Eq. (2.27), the rate dependent relaxation spectrum is noted as $H_{r\theta}$ since the spectrum is measured from output response $\sigma_{r\theta}$ which is in the direction of large deformations. For an ideal isotropic fluid, rate dependent spectra measured in orthogonal directions is equal ($H_{rz}(\tau, \dot{\gamma}) = H_{r\theta}(\tau, \dot{\gamma})$).

By applying Fourier transform on Eq. [2.26], we can evaluate the orthogonal complex modulus $G'_{\perp}(\omega, \dot{\gamma})$ and $G''_{\perp}(\omega, \dot{\gamma})$ in terms of rate dependent relaxation spectrum as:

$$G'_{\perp}(\omega, \dot{\gamma}) = \int_0^{\infty} H_{rz}(\tau, \dot{\gamma}^2) \frac{\omega^2\tau^2}{1 + \omega^2\tau^2} d\ln\tau \tag{2.28}$$

$$G''_{\perp}(\omega, \dot{\gamma}) = \int_0^{\infty} H_{rz}(\tau, \dot{\gamma}^2) \frac{\omega\tau}{1 + \omega^2\tau^2} d\ln\tau \tag{2.29}$$

We use the OSP complex modulus data obtained from orthochirp experiments which are plotted in Fig. 2-5 to compute the rate dependent relaxation spectrum. By substituting for $\gamma_{r\theta} = \dot{\gamma}(t - t')$ in Eq. (2.27), we can write the shear stress $\sigma_{r\theta}$ as:

$$\frac{\sigma_{r\theta}(\dot{\gamma})}{\dot{\gamma}} = \eta(\dot{\gamma}) = \int_0^{\infty} H_{r\theta}(\tau, \dot{\gamma}^2) d\tau \tag{2.30}$$

The orthogonal moduli $(G'_{\perp}(\omega, \dot{\gamma}), G''_{\perp}(\omega, \dot{\gamma}))$ which are modeled by FML using Eq. (2.19) and Eq. (2.19) as seen in Fig. 2-10 can be substituted in Eq. (2.28) and Eq. (2.29). We use Tschoegl's method of Stieltjes integrals to solve the inverse integrals in Eq. (2.28) and Eq. (2.29) to derive the expression for rate dependent relaxation spectrum ($H_{rz}(\tau, \dot{\gamma})$) in terms of the FML parameters:

$$H_{rz}(\tau, \dot{\gamma}) = \frac{1}{\pi} \frac{\mathbb{G}\lambda(\dot{\gamma})^{1-\beta}\tau^{-1}\sin(\pi\beta)}{\lambda(\dot{\gamma})^{1-\beta}\tau^{\beta-1} + \lambda(\dot{\gamma})^{\beta-1}\tau^{1-\beta} + 2\cos(\pi(1-\beta))} \tag{2.31}$$

This rate dependent spectrum $H_{rz}(\tau, \dot{\gamma})$ for shear rates ($\dot{\gamma} = 0\ s^{-1}$, $0.1\ s^{-1}$, $1\ s^{-1}$, $10\ s^{-1}$, $100\ s^{-1}$) are shown in Fig. 2-11. For a specified shear rate, at short relaxation times ($\tau \ll \lambda$), the rate dependent spectrum H_{rz} scales as $\tau^{-\beta}$ and at long time scales ($\tau \gg \lambda$) as $\tau^{2-\beta}$. We

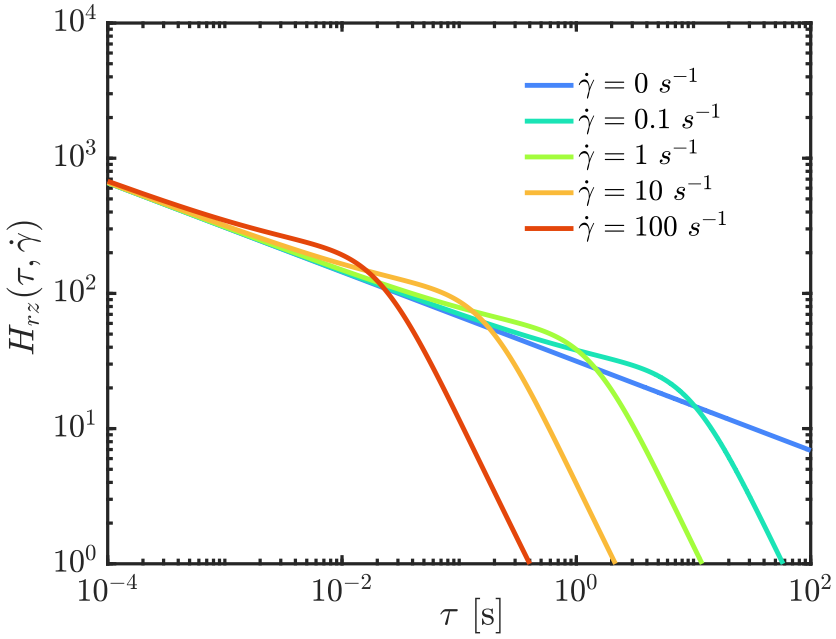

Figure 2-11: The rate dependent spectrum H_{rz} obtained from FML modeling of orthogonal moduli data at different unidirectional shear rates. There is a progressive reduction in the contribution to the spectrum at long time scales as the shear rate increases.

observe a point of inflexion in the relaxation spectrum at the FML characteristic relaxation time $\tau = \lambda(\dot{\gamma}) = 1.5/\dot{\gamma}$ following which the contribution of relaxation time scales to the spectrum is reduced. Therefore, due to the application of shear rate, the contribution of relaxation time scales greater than $1.5/\dot{\gamma}$ to the relaxation dynamics of weakly associated alginate gel is lessened. This implies that the unidirectional shear rate $\dot{\gamma}$ alters the relaxation dynamics of the alginate gel. The long relaxation time scales contribution to the relaxation dynamics of the alginate gel progressively reduces as the shear rate increases as illustrated in Fig. 2-11.

2.4.3 The KBKZ Approach to OSP

The computation of rate dependent spectra $H_{r\theta}$ from the output response in the direction of flow or large deformation cannot be achieved using parallel superposition of small chirp deformation to the flow. This is because of the non-linear cross coupling that takes place between the two steady shear flow and oscillatory deformation. Therefore, the response

spectrum from parallel superposition is not equal to the rate dependent spectra $H_{r\theta}$ that we are interested in. Therefore, to compute the rate dependent spectrum $H_{r\theta}$, we consider the general constitutive K-BKZ model [106] which is written as:

$$\boldsymbol{\sigma(t)} = \int_{-\infty}^{t} \left[\frac{\partial U}{\partial I_1} \boldsymbol{C^{-1}}(t,t') - \frac{\partial U}{\partial I_2} \boldsymbol{C}(t,t') \right] dt' \tag{2.32}$$

where $\boldsymbol{C}(t,t')$ and $\boldsymbol{C}^{-1}(t,t')$ are the Cauchy-Green strain tensor and Finger strain tensor respectively as introduced in 1.3.2. The invariants I_1 and I_2 are given by the traces of finger strain tensor ($\boldsymbol{C}^{-1}$) and Cauchy-Green strain tensor ($\boldsymbol{C}$) respectively. U is a potential function related to the strain energy of the material and depends on I_1, I_2 and $t - t'$. For step strain experiments and steady shear flow the potential function can be factorized to a temporal response, otherwise known as the memory function $M(t-t')$ and a simple potential $u(I_1, I_2)$ which only depends on the invariants [80]. Wagner further simplified the factorized K-BKZ by the assumption that the simple potential u is independent of second invariant I_2 to write the stress tensor as:

$$\boldsymbol{\sigma(t)} = \int_{-\infty}^{t} M(t-t') h(I_1, I_2) \boldsymbol{C^{-1}}(t,t') dt' \tag{2.33}$$

where $h(I_1, I_2) = \partial u(I_1)/\partial I_1$ is known as the damping function of the material. It relates to the survival probability of the physical network of chains depending on the deformation [102]. The memory function $M(t)$ is a Laplace transform of the linear relaxation spectrum with respect to $1/\tau$

$$M(t-t') = \int_{0}^{\infty} \frac{H(\tau)}{\tau} e^{-t/\tau} \frac{d\tau}{\tau} \tag{2.34}$$

and hence the Eq. (2.33) can be rewritten in terms of linear relaxation spectrum as

$$\boldsymbol{\sigma(t)} = \int_{-\infty}^{t} \int_{0}^{\infty} \frac{H(\tau)}{\tau^2} e^{-t/\tau} h(I_1, I_2) \boldsymbol{C^{-1}}(t,t') d\tau dt' \tag{2.35}$$

For simple steady shear flow, following [7], the invariants I_1 and I_2 are both equal and can be written as $I = \gamma^2 + 3 = \dot{\gamma}^2(t - t')^2 + 3$. Therefore, Eq. (2.35) can be expressed as

$$\boldsymbol{\sigma}(\boldsymbol{t}) = \int_{-\infty}^{t} \int_{0}^{\infty} \frac{H(\tau)}{\tau^2} e^{-t/\tau} h(\gamma) \boldsymbol{C^{-1}}(t, t') d\tau dt' \tag{2.36}$$

When a small oscillatory strain is imposed orthogonal to the shear rate, the damping function still remains the same because of the small amplitude nature of the superposed orthogonal strain and hence Eq. (2.36) holds appropriate for OSP. The damping function maybe defined as

$$h(\gamma) = \frac{G(t, \gamma)}{G(t)} \tag{2.37}$$

where $G(t, \gamma)$ is the strain dependent relaxation modulus and $G(t)$ is the linear relaxation modulus. We performed a series of increasing step strain experiments and obtained the relaxation modulus of 3.5 wt% concentration of alginate system as shown in Fig. 2.4.3. The relaxation modulus of 3.5 wt% alginate system for step strain amplitude $\gamma < 0.3$ is independent of the strain amplitude. As the amplitude increases, the modulus decreases systematically. The damping function values for each strain is found by collapsing all the plots to the linear relaxation modulus as shown in Fig. 2-13. The most commonly used damping functions used are of the form: $h(\gamma) = 1/(1 + a\gamma^2)$ and $h(\gamma) = e^{-\gamma/\gamma^*}$ [47, 102]. Both the damping function function fits are employed to the damping values computed in Fig. 2-13 with $a = 1$ and $\gamma^* = 1.5$. We prefer the exponential damping function since it enables us to derive analytical results using Eq. (2.36)

$$\boldsymbol{\sigma}(\boldsymbol{t}) = \int_{-\infty}^{t} \int_{0}^{\infty} \frac{H(\tau)}{\tau^2} e^{-t/\tau} e^{-\gamma/\gamma^*} \boldsymbol{C^{-1}}(t, t') d\tau dt' \tag{2.38}$$

From Eq. (2.38), we follow the steps carried out in [100] to obtain the expression for orthogonal moduli and the steady flow viscosity:

$$G'_{\perp}(\omega, \dot{\gamma}) = \int_{0}^{\infty} H_0(\tau) \left(\frac{\omega^2 \tau^2}{(\dot{\gamma}\tau/\gamma^* + 1)[(\dot{\gamma}\tau/\gamma^* + 1)^2 + \omega^2\tau^2]} \right) d \ln \tau \tag{2.39}$$

$$G''_{\perp}(\omega, \dot{\gamma}) = \int_{0}^{\infty} H_0(\tau) \left(\frac{\omega\tau}{(\dot{\gamma}\tau/\gamma^* + 1)^2 + \omega^2\tau^2} \right) d \ln \tau \tag{2.40}$$

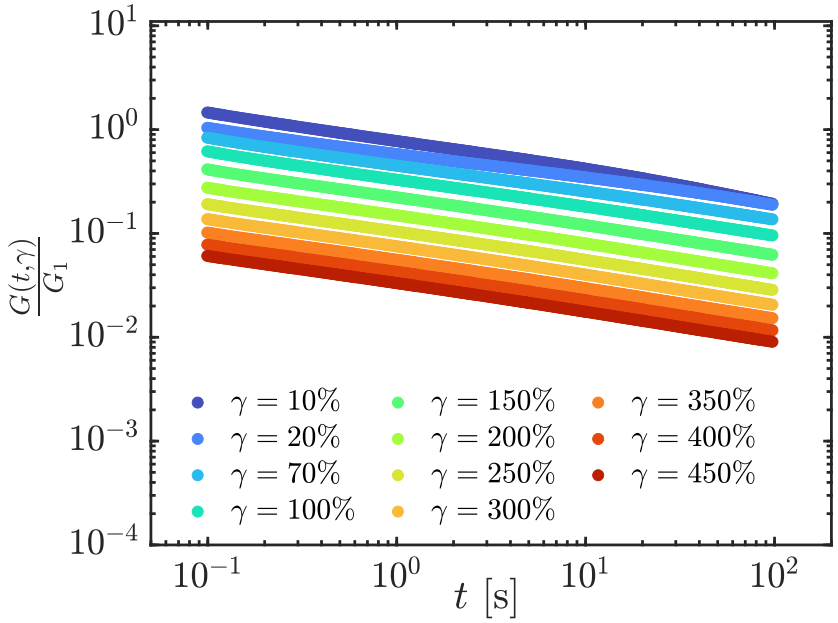

Figure 2-12: Experimental measurements of the relaxation modulus for various imposed strains. The modulus decreases by a constant factor across time as imposed step strain amplitude is increased. G_1 is the relaxation moduli $G(t = 1\text{ s}, \gamma = 10\%)$ which is used to normalize the relaxation modulus

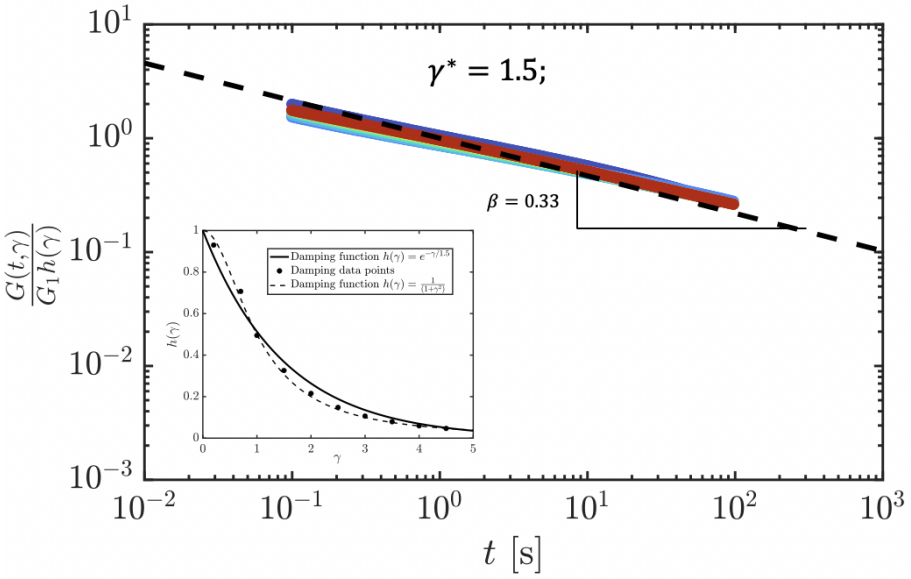

Figure 2-13: Relaxation modulus for various strains are collapsed to the linear relaxation moduli to form a mastercurve. The corresponding vertical shift factors are the damping values and are shown in the inset figure. The solid line fit to the damping values is an exponential damping function fit: $h(\gamma) = e^{-\gamma/\gamma^*}$ and the dashed line correspond to the damping function fit: $h(\gamma) = 1/(1+\gamma^2)$

.

$$\eta(\dot{\gamma}) = \int_0^{\infty} \frac{H_0(\tau)}{[1 + (\dot{\gamma}\tau/\gamma^*)]^2} d\tau \tag{2.41}$$

Substituting the linear relaxation spectrum H_0 of a critical gel in terms of FML parameters ($\mathbb{G}, \beta, \mathbb{V} \rightarrow \infty$) and the damping coefficient γ^*, we can obtain the analytical form of steady shear flow viscosity as:

$$\eta(\dot{\gamma}) = \mathbb{G}\beta \left(\frac{\dot{\gamma}}{\gamma^*}\right)^{\beta-1} \tag{2.42}$$

To find the rate dependent spectrum from Eq. (2.39), Eq. (2.40) and Eq. (2.41), Curtis et al. [16] defined a reduced relaxation time:

$$\tau_c = \frac{\tau}{1 + \dot{\gamma}\tau/\gamma^*} \tag{2.43}$$

The computation of rate dependent spectrum following the procedure detailed by Curtis et al. by measuring damping function provides us $H_{r\theta}$ since it is computed from output response in the direction of large deformations ($r\theta$). Substituting Eq. (2.43) in Eq. (2.39), Eq. (2.40) and Eq. (2.41), the $H_{r\theta}$ can be derived as:

$$H_{r\theta}(\tau, \dot{\gamma}) = \begin{cases} H_0\left(\tau(1 - \dot{\gamma}\tau/\gamma^*)^{-1}\right), & 0 < \tau_c < \gamma^*/\dot{\gamma} \\ 0, & \gamma^*/\dot{\gamma} < \tau < \infty \end{cases} \tag{2.44}$$

The damping coefficient is $\gamma^* = 1.5$ for the 3.5 wt.% alginate gel used here. Using the Eq. (2.44), the spectrum is computed and illustrated in Fig. 2-14 for various shear rates ($\dot{\gamma} = 0$ s^{-1}, 0.1 s^{-1}, 1 s^{-1}, s^{-1}, 10 s^{-1} and 100 s^{-1}). The contribution of long relaxation time scales $\tau > \gamma^*/\dot{\gamma}$ to rate dependent spectrum $H_{r\theta}$ is completely cut off. Therefore, there is no contribution of long relaxation modes $\tau > \gamma^*/\dot{\gamma}$ in the relaxation dynamics of alginate gel in $r\theta$ direction when a unidirectional shear rate is applied. Eq. (2.41).

2.5 Discussion

The rate dependent spectrum H_{rz} is perperdicular to the direction of applied large non-linear deformation obtained from the modeling orthogonal moduli data using fractional

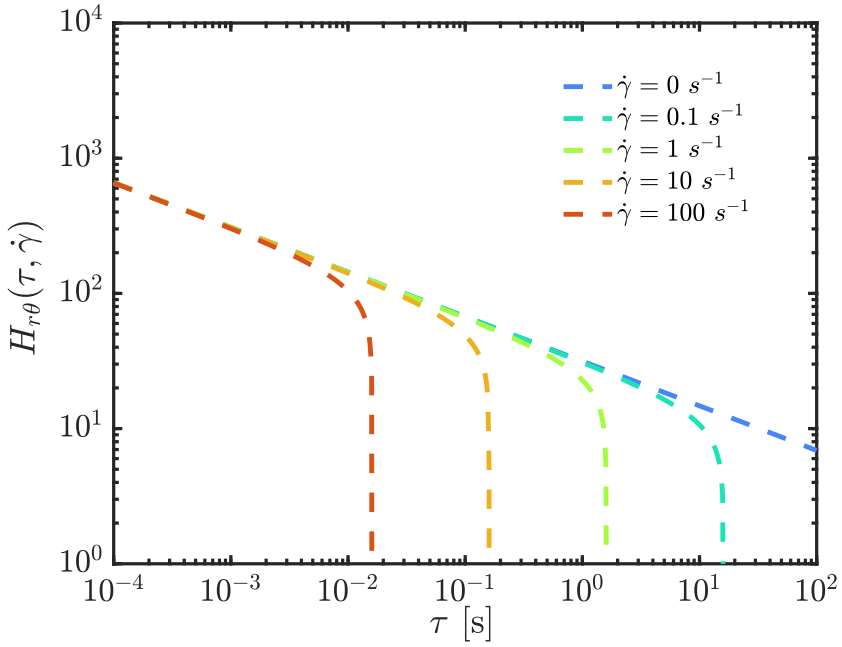

Figure 2-14: Rate dependent spectrum $H_{r\theta}$ measured in the azimuthal direction is obtained using the critical strain γ^* in the exponential damping function. There is a complete cut off in the spectrum for relaxation time scales greater than $\tau \geq \gamma^*/\dot{\gamma}$.

Maxwell liquid model and inverted using Tschoegl's method of Stieltjes integrals. H_{rz} is compared with the rate dependent spectrum $H_{r\theta}$ in the direction of applied large non-linear deformation extracted from damping function using the method outlined in [16] is shown in Fig. 2-15. The variation between the two rate dependent spectrum clearly demonstrates the flow induced anisotropy in the alginate gel. A closer look at the comparison between these two spectra in Fig. 2-15) informs us there is no relaxation mechanisms in the material whose time scale is greater than $\gamma^*/\dot{\gamma}$ in the direction of applied non-linear deformation (unidirectional shearrate) while in the perpendicular direction to the applied non-linear deformation, the longer relaxation time scales contribution ($> (\dot{\gamma})$) reduces but does not get completely cut off. This is in agreement with Fig. 2-16. The experimental data points of viscosity are in agreement with the area under $H_{r\theta}$ spectrum or its equivalent Wagner model while there is a significant difference when viscosity is calculated from area under the H_{rz} spectrum.

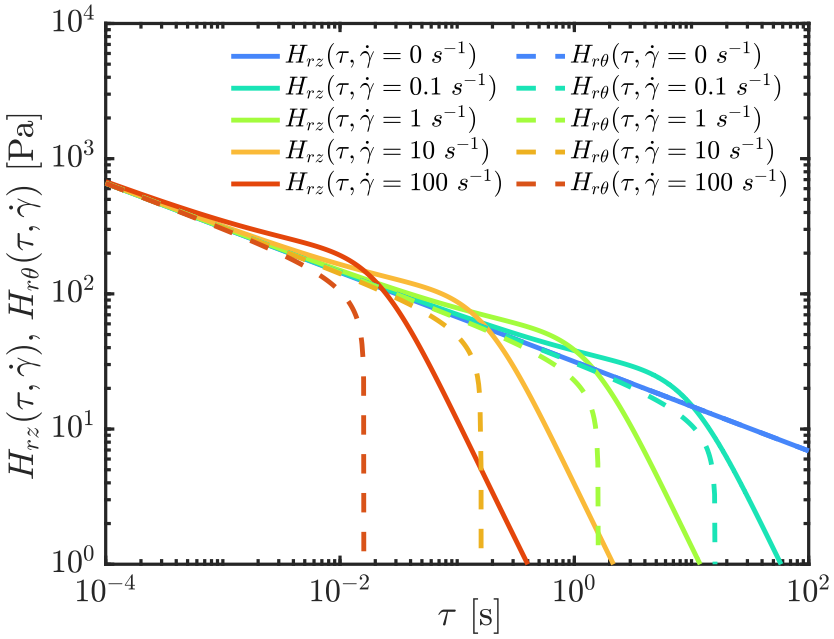

Figure 2-15: The distinction between rate dependent spectrum in the orthogonal direction of applied large deformation H_{rz} and $H_{r\theta}$ in the direction of applied large deformation indicate flow induced anisotropies in the alginate gel.

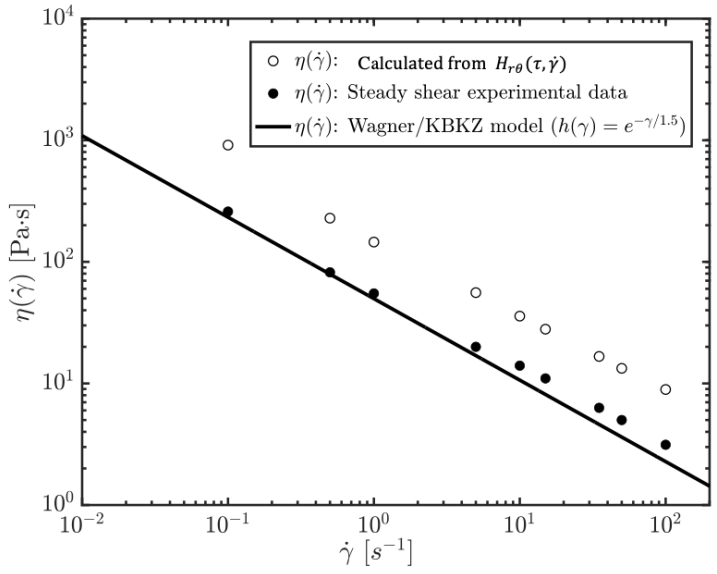

Figure 2-16: Comparison of steady shear viscosity and viscosity calclauted from obtaining the area under rate dependent spectrum ($H_{r\theta}(\tau,\dot{\gamma})$) obtained from orthogonal moduli data under shear. The discrepancy points towards flow induced anisotropies.

2.6 Conclusion

The use of optimally windowed chirps in orthogonal superposition rheometry has been demonstrated in this work using 3.5% high viscosity alginate gel. The orthogonal rate dependent moduli is obtained by employing optimally windowed chirp perpendicular to the unidirectional shear rate. The viscoelastic properties of the alginate gel acts as a critical gel [103] when there is no large non-linear unidirectional shear imposition. As a steady unidirectional shear is applied, the material behaves as a shear thinning viscoelastic pre-gel with characteristic time scale inversely proportional to the strength of the applied unidirectional shear.

Continuous chirps of short duration is applied immediately after the cessation of shear allow us to obtain the transient orthogonal moduli for different frequencies at different times. We observe the moduli for our alginate gel to recover in around $28s$ after cessation of shear. Transient responses on time scales of the order $O(10)$ s were unfeasible to probe previously because of the limitations of conventional SAOS frequency sweeps. The rate dependent spectrum in the direction of non-linear large deformation (unidirectional shear) and in the perpendicular direction have both been obtained using the techniques outlined in subsections 2.4.3 and 2.4.2 respectively. The distinction between the spectrum in different directions is attributed to the flow induced anisotropy in alginate gel. From the rate dependent spectra H_{rz} and $H_{r\theta}$, we can deduce that the application of shear completely cuts off the contribution of longer relaxation time scales $\tau > \gamma^*/\dot{\gamma}$ while in the perpendicular direction, the contribution of longer relaxation time scales beyond $\lambda(\dot{\gamma})$ is reduced. This flow induced anisotropy in alginate gel can also be noted from the variation in steady shear viscosity experimental data points and data obtained from the area under H_{rz} spectrum in Fig. 2-16.

Chapter 3

Gaborheometry: Applications of the discrete Gabor transform for time-resolved oscillatory rheometry

3.1 Introduction

There have been significant advances in the field of signal processing in the last 50 years whose utilization ranges to a variety of engineering and research applications such as acoustics, image processing, astronomy, data transmission, speech recognition and medical imaging such as CAT scans and MRI [19, 22, 31, 40, 48, 59, 92]. These advanced signal processing techniques have until recently been under utilized in the field of rheometry. However in recent years, there has been a significant trend in developing signal processing techniques relevant to soft material characterization such as Large Amplitude Oscillatory Shear (LAOS) [26, 26, 26, 30, 27, 29, 25, 28, 21, 77, 44], Medium Amplitude Oscillatory Shear (MAOS) [88, 68] and Medium Amplitude Parallel Superposition (MAPS) [63, 62]. These techniques help in probing the viscoelastic material properties of an unknown material which paves the way for understanding the flow behavior of the material at different stresses or strain state. For viscoelastic materials, these rheological measures are a function of frequency of the material deformation and aid in characterizing materials for

a range of applications in consumer industries, automotive sectors and oil and gas industries. However, the signal processing used to analyze these oscillatory techniques including conventional Small Amplitude Oscillatory Shear (SAOS) utilize discrete Fourier transform (DFT) which does not introduce any time resolution by itself. This makes it difficult to characterize mutating materials which are both time and shear rate or stress dependent.

There are several phenomena which are responsible for the mutating nature of viscoelastic properties in complex fluids. For example, in metal-ion crosslinked polymers, the metal ion coordinate bonds can be reversible [43, 66]. This results in build up of structural features over time when breakdown of the microstructure is initiated by large deformations such as high shear-rate or stress. Shear induced microstructural build up and breakdown (not necessarily by reversible coordinate bonds) over time is reflected in terms of the dependence of viscoelastic properties not just on frequency but also on elapsed time or waiting time. This phenomena is common in many complex fluids and such systems, which do not satisfy time translation invariance are widely characterized or known as thixotropic materials [69, 71, 60, 23]. In soft glassy materials, there is no need for shear or large deformations to induce structural build up. These materials are out of thermodynamic equilibrium and show time dependent slowing down of relaxation dynamics[50, 49, 51, 2, 3, 52, 85]. The mobility of the microscopic constituents due to the thermal energy induces slow steady structural evolution with time to form progressively more stable structures to reduce the free energy. This process of structural evolution with time observed in soft glassy materials is known as physical aging [83, 86, 84, 87, 1, 4, 39]. In the process of physical aging, the elastic modulus and relaxation time typically increases with time.

To quantify the rate of evolution in such mutating materials, Winter *et al*, introduced a dimensionless number they called the mutation number Mu_g as a measure to characterize the change in the property of the material within the experimental time. Here g indicates the property of interest and Mu_g is defined as the ratio between mutation time λ_{Mu} and the experimental time Δt required to obtain the material property of interest [74]. The mutation time λ_{Mu} is defined as the characteristic time constant for the change of material:

$$\lambda_{Mu} = \left[\frac{\partial \ln g}{\partial t}\right]^{-1} \tag{3.1}$$

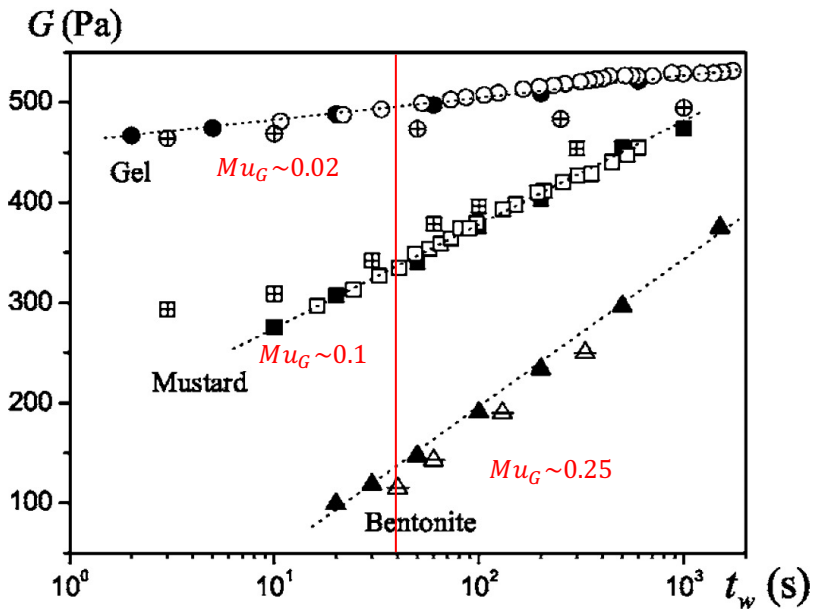

Figure 3-1: Time dependency of the elastic modulus for various thixotropic/ mutating materials. Image reproduced from [15]. t_w represent the elasped or waiting time after preshear at which the small amplitude oscillatory deformation is imposed to obtain the moduli data. The steeper slope for the bentonite data indicates a higher mutation number than the gel and mustard.

The experimental time Δt for an oscillatory shear experiment which takes a single cycle to complete is $\Delta t = 2\pi/\omega$. Therefore the mutation number can be written as:

$$Mu_g = \frac{\Delta t}{\lambda_{Mu}} = \frac{2\pi}{\omega}\frac{d\ln g}{dt} \tag{3.2}$$

In order to obtain accurate measurements, the property of the material should not change significantly within the duration of the experiment and therefore we require the criterion $Mu_g \leq 0.15$ [18].

In Fig. 3-1 we reproduce the data from [15] which shows the time dependency of the elastic modulus of several soft materials which are of high importance to various consumer and oil industries. The three materials shown in Fig. 3-1 are an unspecified gel, mustard and bentonite clay which is commonly used in the drilling industry. It is clear that the bentonite sample has the highest mutation number among the three systems. Satisfying the criterion $Mu_g \leq 0.1$ can be challenging for such rapidly mutating systems. The time dependency

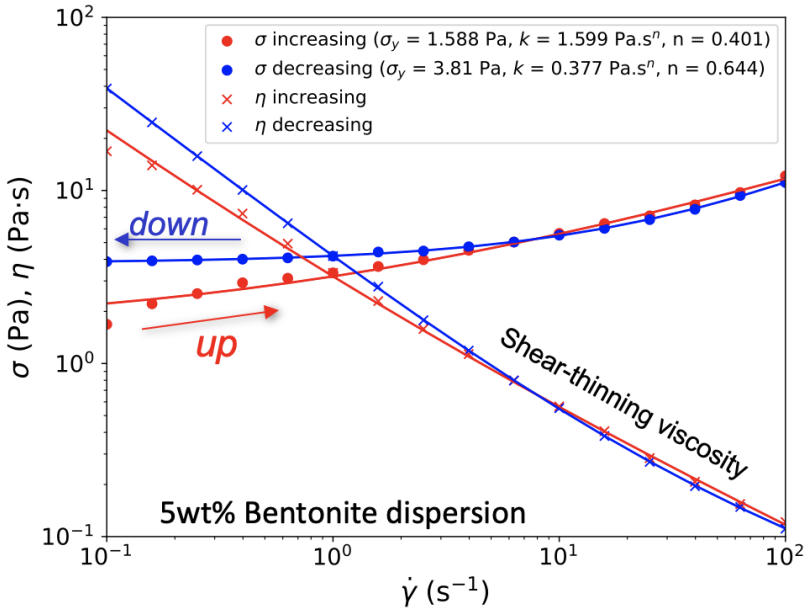

Figure 3-2: Evolution in the steady shear viscosity and shear stress for a 5% bentonite dispersion in deionized water. Blue color indicates the data for which the shear rate is increased from $\dot{\gamma} = 0.1$ to 100 s^{-1}. Red color indicates the data for which shear rate is decreased from $\dot{\gamma} = 0.1$ to 100 s^{-1}. The total elapsed time of sweep in one direction is 1800 s.

of bentonite's viscoelastic properties can be observed in the flow curve as well, as seen in Fig. 3-2. The flow curves can be well described by the Herschel Bukley model $\sigma = \sigma_y + k\dot{\gamma}^n$ and a systematic increase of the yield stress $\sigma_y(t)$ is observed with time. For such mutating materials, Geri *et al* introduced the Optimally Windowed Chirp (OWCh) which makes use of frequency modulated exponential Chirp signal in conjunction with Tukey windowing to replace standard SAOS techniques in order to enable rapid determination of the frequency response viscoelastic materials in the linear regime [35, 9]. This technique, which reduces the experimental time required to perform a frequency sweep results in a reduction of the mutation number Mu_g, and hence they have shown this can be used for time-evolving systems to obtain the frequency response characteristics at a given instant of time for a range of frequencies [36]. For rapidly mutating materials, even the usage of the Optimally Windowed Chirp techniques can be challenging since it can be difficult to satisfy the criteria $Mu_g \leq 0.15$.

A desirable feature of any new advanced signal processing techniques would be to

enable both time and frequency resolution of rapidly mutating materials which are of high interest to various industrial and biomedical applications. To this end, we introduce the Gabor transform for analysis of rheometric data. This is a special case of the Short Time Fourier Transform (STFT) and enables determination (within constranits discussed later) of both time and frequency resolution from oscillatory experiments. The Gabor transform uses a localized Gaussian function as a window in conjunction with a Fourier transform to provide both time and frequency resolution. The use of a Gaussian function helps facilitate derivation of analytical results on the errors incurred and helps us to understand the details of the process theoretically. The Gaussian window has been proven to have the minimum time-frequency uncertainty of available window functions providing a strong case to use this special case of the STFT, known as the Gabor transform for rheometric applications.

In this work, we start by briefly reviewing the discrete Fourier transform (DFT) and its limitations. Then, we introduce the Gabor transform and the computational details required such as selection of window length, amplitude correction in rheometry for its applications. We first demonstrate use of the Gabor transform to resolve the time dependent complex modulus for an aging Kelvin Voigt model and then proceed to use the algorithm developed to extract the time-dependent complex modulus of an aging 5 wt. % bentonite dispersion. We also discuss two other applications of the Gabor transform in rheometry: (i) extracting steady state frequency response as well as the transient response accurately from the initial oscillatory data recorded following the initial inception of oscillatory shear which helps us to obtain data with short duration experiments and reduces the need to wait long periods for the viscoelastic transient response to subside; (ii) accurately extracting and monitoring the evolution of the non-linear Fourier or Chebyshev coefficients in LAOS with increasing strain or stress amplitude at a specified deformation frequency. This latter application streamlines the LAOS tests by reducing the number of experiments required and the data post processing times that are required to obtain the non-linear Chebyshev-Fourier coefficients that characterize viscous and elastic non-linearities. We refer to the use of the discrete Gabor transform for rheometric applications as *Gaborheometry*. Finally we discuss importance of Heissenberg's time-frequency uncertainty principle [57, 11] in using Gabor transform which provides guidance in selecting the trade-off between selecting time and

frequency resolution and its importance in designing convenient and robust experimental protocols in rheometry.

3.2 Discrete Fourier transform in rheometry

3.2.1 Introduction to the Discrete Fourier Transform (DFT)

The complex modulus of a linear viscoelastic material can be defined for a periodic small amplitude oscillatory shearing deformation by

$$G^*(\omega) = G'(\omega) + iG''(\omega) = \frac{\tilde{\sigma}(\omega)}{\tilde{\gamma}(\omega)} \tag{3.3}$$

where $\tilde{\sigma}(\omega)$ is the discrete Fourier transform (DFT) of the stress signal and $\tilde{\gamma}(\omega)$ is the discrete Fourier transform of the strain signal [8]. The real part of the complex moduli is the storage modulus and the imaginary part is the loss modulus. The discrete Fourier transform for time signal of $x(t)$ considers the entire time signal and is defined as

$$\tilde{x}_{DFT}(\omega_k) = \sum_{n=0}^{N-1} x(t_n) e^{-i\omega_k t_n} \qquad k = 0, 1, 2, \ldots N-1 \tag{3.4}$$

where $x(t_n)$ is the input signal amplitude at each time t_n, N is the total number of points present in the digital signal or the number of time samples, dt is the time sampling interval and $t_n = n \cdot dt$ is the n^{th} sampling instant. The total duration of the signal is $T = (N-1)dt$. $\tilde{x}_{DFT}(\omega_k)$ is the complex valued spectrum of x at frequency ω_k, $\omega_k = k\Omega$ is the k^{th} frequency sample, $\Omega = 2\pi/(N \cdot dt)$ is the radian-frequency sampling interval and $f_s = 1/dt$ is the sampling rate. The kernel consists of complex information samples at discrete frequencies ω_k, between 0 and $\omega = 2\pi/dt$. But, the second half of the information in frequency domain does not contain new information and they correspond to the negative frequencies. Therefore, only $N/2$ frequency samples with true information is obtained in frequency domain from N discrete time samples. These different parameters are depicted schematically in Fig. 3-3. $\tilde{x}_{DFT}(\omega_k)$, the DFT at frequency ω_k , is a measure of the amplitude and phase of the complex information present in the input signal x at that frequency [89].

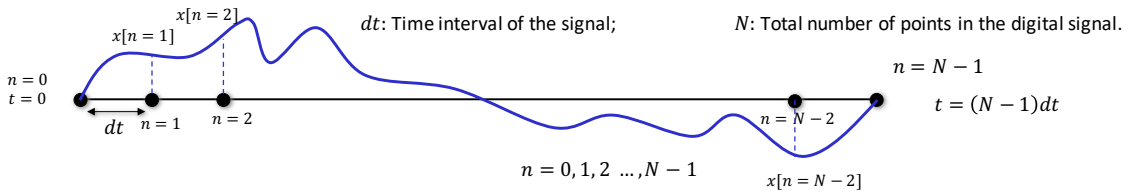

Figure 3-3: Digital signal is composed of N total points with a time interval dt. $x[n]$ corresponds to the digital signal at $x(n \cdot dt)$ where $n \in 0, 1, 2...N-1$

3.2.2 Limitations of DFT: No time resoultion and assumption of time translation invariance

The discrete Fourier transform considers the entire time signal in order to calculate the amplitudes of the different frequency components present in the time signal. The time-resolved frequency information is not obtainable from Eq. (3.4) using a discrete Fourier transform. To illustrate this, in Fig. 3-4 (a), we show the time signal comprised of two different frequencies. The signal is constructed by the follosing stepwise frequency

$$x(t) = \begin{cases} \sin(1t) & t < 20\pi \\ \sin(5t) & t > 20\pi \end{cases} \tag{3.5}$$

The Fourier transform of the signal constructed from Eq. (3.5) is shown in Fig. 3-4 (b). As expected, the Fourier transform correctly gives the information about the two different frequencies (1 and 5 rad/s) present in the time signal; however, the time resolved frequency information for locating the peaks at $\omega = 1 rad/s$ and $\omega = 5 rad/s$ are present in the signal is not clearly indicated. The small amplitude oscillations seen in Fig. 3-4 (b) are known as Fresnel ripples and indicate that the signal is not infinitely periodic and represents the step discontinuity of the frequency components in the signal. No time information capturing when a particular frequency is present in the time signal is present in the output of the Discrete Fourier transform.

The second limitation of the discrete Fourier transform is the assumption of time translation invariance (TTI). To illustrate this limitation, we construct a sinusoidal signal with a

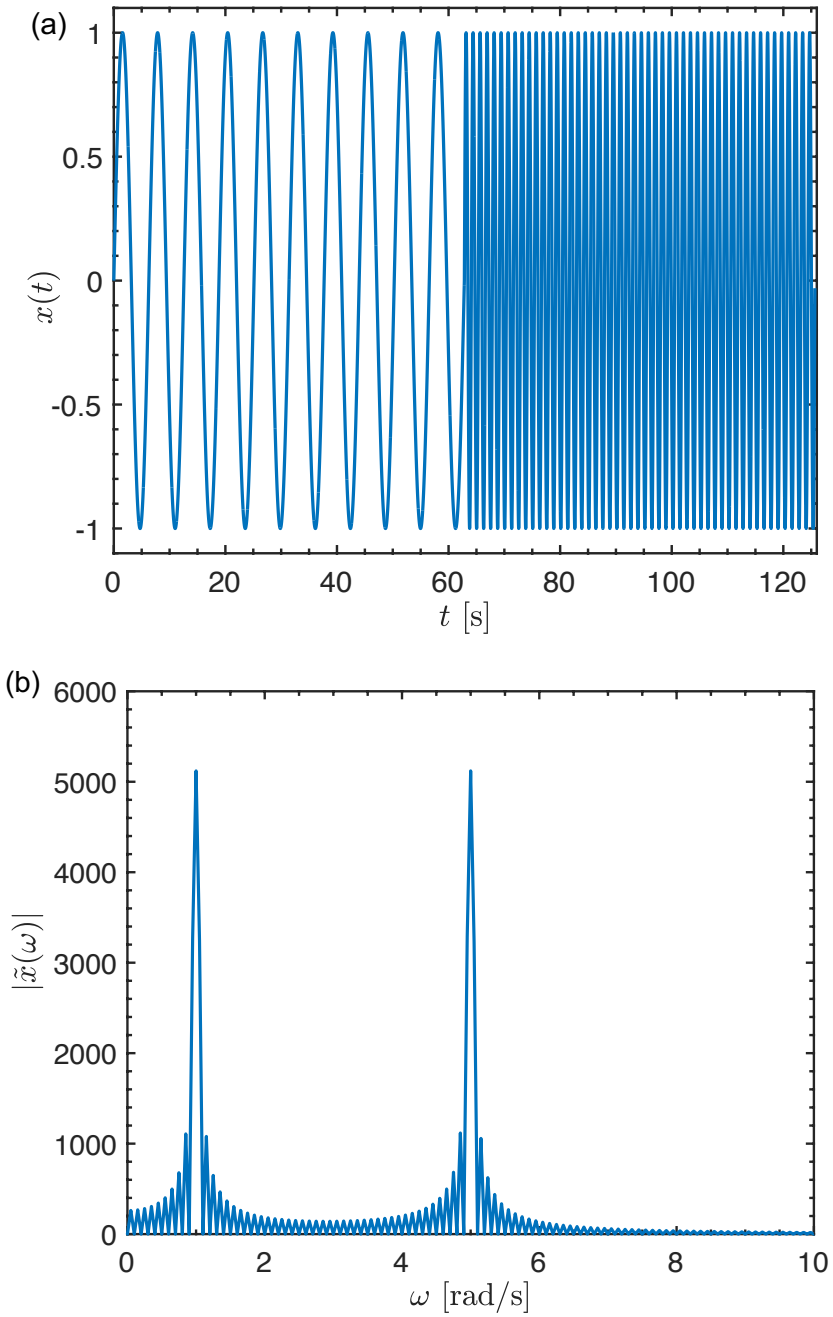

Figure 3-4: (a) A time series constructed according to Eq. (3.5). The total number of points $N = 10240$ and the duration of the time signal is $Ndt = 40\pi$. (b) Frequency spectrum following discrete Fourier transform of (a). The ripples observed in the frequency spectrum is because of the finite periodicity of the time signal and the time dependency in changing the frequency of the signal.

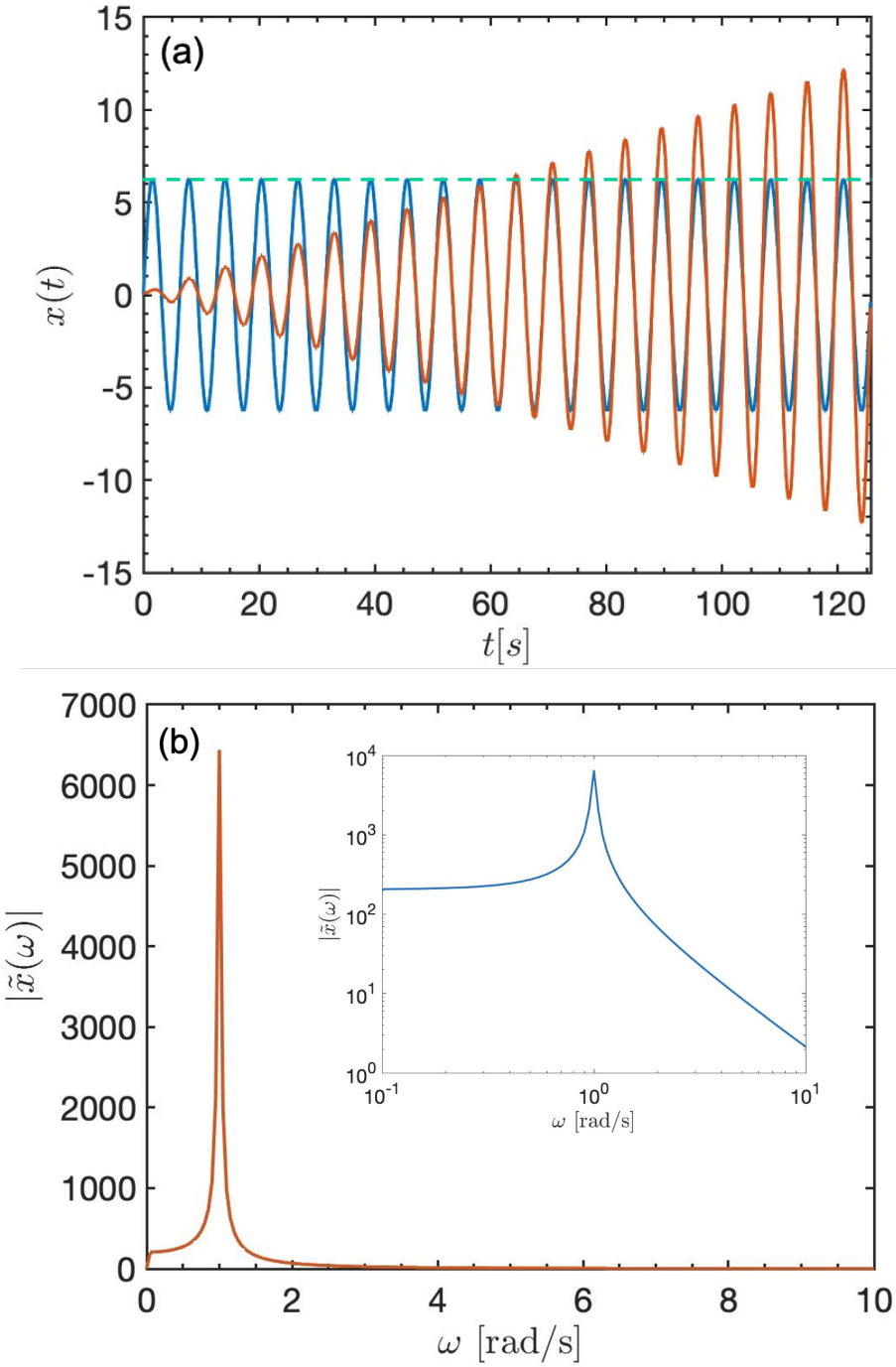

Figure 3-5: (a) The orange solid line represents the sinusoidal signal whose amplitude increases linearly with time according to Eq. (3.6). The blue solid line represents the signal constructed just from the peak value of frequency spectrum of Eq. (3.6). The total number of points $N = 20480$ and the duration of the time signal is $Ndt = 40\pi$. (b) The plot shows the frequency spectrum of the time signal in Eq. (3.6). The non-zero components observed in the inset figure apart from the peak frequency $\omega = 1$ rad/s are due to the time dependent amplitude in the sinusoidal signal $x(t) = 0.1t\sin(t)$.

strictly increasing amplitude

$$x(t) = 0.1t\sin(\omega_0 t) \tag{3.6}$$

where $\omega_0 = 1$ rad/s. The resulting time signal is shown in Fig. 3-5 (a) by orange solid line and the discrete Fourier transform of Eq. (3.6) is plotted in Fig. 3-5 (b). Unlike the DFT of a time invariant sinusoid, the DFT of the time signal in Eq. (3.6), is non-zero even at frequencies $\omega \neq \omega_0$, where $\omega_0 = 1$ rad/s for our example. This can be more clearly visualized by using a logarithmic scaling as shown in the inset figure Fig. 3-5 (b). The peak value of the discrete transform at $\tilde{x}(\omega = \omega_0)$ in Fig. 3-5 (b) equals the value of DFT at $\omega = \omega_0$ of the time invariant sinusoidal signal with frequency of ω_0 and mean amplitude of entire signal in Eq. (3.6) with duration T. The time invariant sinusoid with amplitude of $0.1T/2$ and frequency of ω_0 is shown in Fig. 3-5 (a) by the blue curve. Therefore, for thixotropic and aging materials, in which the output signal corresponding to the measured strain response to a constant amplitude sinusoidal stress input, using just the numerical value of DFT at the frequency of input signal in order to calculate the material property G^* will result in the mean value of G^* over the duration of the experiment, but does not provide us with the dependence of the complex moduli with time.

3.2.3 Piece-wise analysis

The current techniques followed for thixotropic and aging materials in which the modulus is both time and frequency analysis is piece-wise analysis. The output signal is broken into a number of different pieces. Each piece-wise signal corresponds to a particular age-time and are processed separately by discrete Fourier transform to obtain the time dependency in aging and thixotropic naterials. For fast mutating materials, this technique can be difficult to obtain accurate results.

As we have attempted to show from these examples, it is important to develop more advanced techniques which can accommodate time-varying signals that do not show time-translation invariance in-order to extract information about temporal variations in the complex modulus for thixotropic and aging materials. Recognizing the advancements in other multifrequency data-rich rheometric techniques such as OWCh and MAPS, we now wish

to seek time-resolved protocols which can capture and separate both time and frequency information for mutating soft material samples.

3.3 Gabor transform

3.3.1 Introduction to Gabor transform

The short time Fourier transform is used to obtain both time and frequency resolution of the time signal. In a short time Fourier transform, the time signal $x(t)$ is multiplied by a window function $w(t-\tau)$ and then a Fourier transform is taken [82].

$$\tilde{x}(\tau,\omega) = \int_{-\infty}^{\infty} x(t)w(t-\tau)e^{-i\omega t}dt \tag{3.7}$$

Here, τ and ω are the time and frequency of interest. $w(t-\tau)$ is the specific window function which localizes the time information in the short time Fourier transform.

The Gabor transform is a special case of short time Fourier transform in which the window function is given by a Gaussian function [34]. The Gaussian function $g(t-\tau)$ is multiplied into the signal $x(t)$ and then the Fourier transform is computed to provide both time t and frequency ω resolution. The Gabor transform can thus be written as

$$\tilde{x}(\tau,\omega) = \int_{-\infty}^{\infty} x(t)g(t-\tau)e^{-i\omega t}dt \tag{3.8}$$

where the Gaussian window function is given by

$$g(t-\tau) = \frac{1}{\sqrt{2\pi}a}e^{-(t-\tau)^2/2a^2} \tag{3.9}$$

Here a, which is the standard deviation of the Gaussian function sets the window length as shown in Fig. 3-6. As $a \to \infty$, the conventional Fourier transform is recovered and there is no windowing or modification to the original time signal $x(t)$ progressively. As a decreases, the window becomes narrower so that the localization improves.

For real discrete time signals such as the digitized strain or stress signals received from the A/D converter of a rheometer, a discrete Fourier transform of the product of the incom-

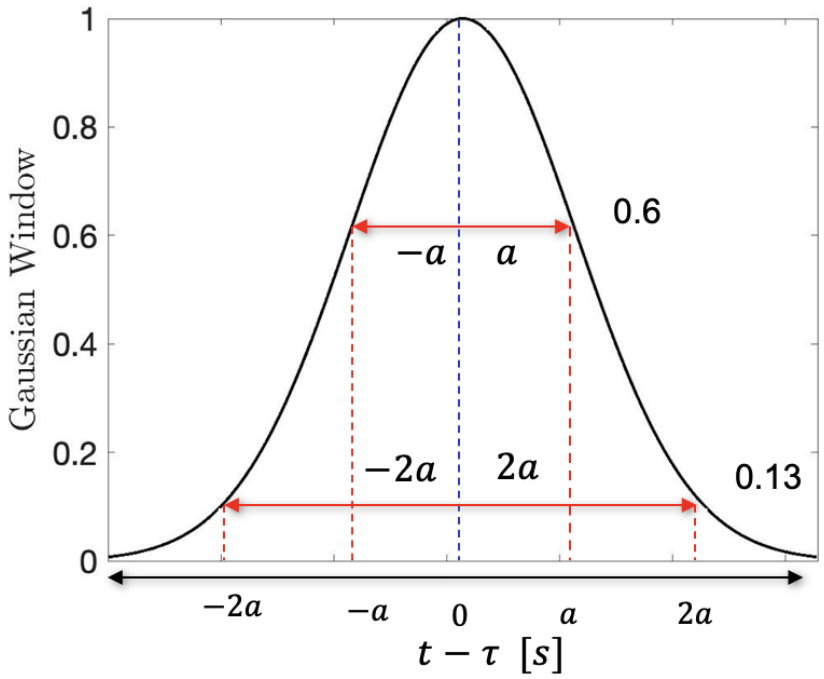

Figure 3-6: Gaussian window is plotted and a, the standard deviation of the Gaussian function is considered as the Gaussian window length. The value of the window at $t-\tau = a$ is $w = 0.6$ and $t - \tau = 2a$ is $w = 0.13$.

ing time signal with the Gaussian window is taken, as represented in Eq. (3.4) instead of a Fourier transform involving integrals.

3.3.2 Amplitude correction due to windowing

Although the Gabor transformation provides a time localization, the window function reduces the amplitude of the transformation variable $\tilde{x}(\tau, \omega)$. In rheometry we need precise values of the amplitude in order to correctly compute quantities such as the dynamic modulus so this amplitude reduction needs to be systematically corrected. To illustrate this, we again consider a sinusoidal signal $x(t) = \sin(\omega_0 t_n)$ with number of discrete points $N = 2048$, the total duration of the signal $T = 40\pi$ and $\omega_0 = 1$ rad/s as shown in Fig. 3-7 (a). A Gaussian window at $\tau = 60s$ is considered in Fig. 3-7 (b). The windowed signal which is the product of the time signal $x(t)$ and the Gaussian window is shown in Fig. 3-7 (c). The calculated amplitude spectra from the discrete Fourier transform of the windowed signal is different from the amplitude spectra of the time signal $x(t) = \sin(\omega_0 t_n)$ without any

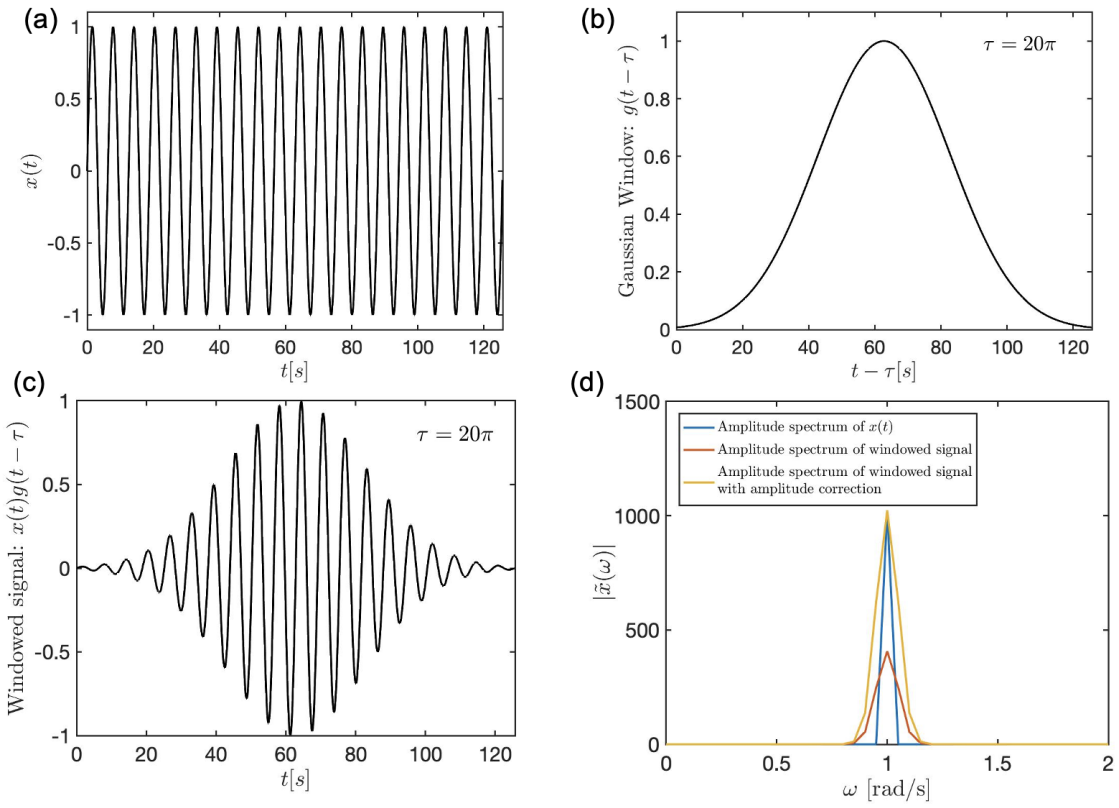

Figure 3-7: (a) The sinusoidal signal $x(t) = sin(\omega_0 t)$ is plotted where $\omega_0 = 1$ rad/s. (b) Gaussian window with $\tau = 20\pi$ is plotted with $a\omega_0 = 2.63$. (c) The windowed signal is the product of $x(t)g(t-\tau)$ is plotted for $\tau = 20\pi$. (d) Amplitude spectrum of $x(t)$ is represented using blue solid line. Amplitude spectrum of the windowed signal is represented using the red solid line and the amplitude spectrum of the windowed signal multiplied with the amplitude correction is shown as the yellow solid line.

windowing. This is shown by the difference between the red solid line which corresponds to the amplitude spectra of the windowed signal and the blue solid line which corresponds to the amplitude spectra of the raw time signal $x(t) = \sin(\omega_0 t)$ without any window in Fig. 3-7 (d). Therefore in order to get the correct value of the complex modulus from a discrete Gabor transform which includes windowing, we use an amplitude correction factor A_w [10] given by

$$A_w = \frac{N}{\sum_{n=0}^{n=N-1} w(t_n)} \tag{3.10}$$

where N is the total number of points in the discrete time signal , $t_n = n \cdot dt$ as defined in section 3.2.1 and $w(t_n)$ is the value of the window function at time t_n. Using this correction factor, we can now write the relationship between the peak magnitude in the amplitude spectra computed for the frequency of the signal $x(t)$ from the discrete Fourier transform and from the discrete Gabor transform.

$$\tilde{x}_{DFT}(\omega = \omega_0) = \tilde{x}_{STFT}(\omega = \omega_0) * A_w \tag{3.11}$$

The yellow solid line in Fig. 3-7 (d), shows the amplitude spectra of the discrete Gabor transform after correction. The peak value now coincides with the peak value of the time signal without any windowing. By using this procedure, the discrete Gabor transform (or any other windowed STFT) can be easily employed to obtain the correct value of complex moduli from the output stress or strain signal at the specified frequency of interest.

3.3.3 Estimation of optimal window length

It remains to understand how the selection of the window length affects our spectral and temporal resolution of our Gabor transform, and if there is an optimal value of the parameter a. In order to find the relationship between the window length and frequency of the time signal, a cosine signal $x_0 \cos(\omega_0 t_n)$ is considered. The discrete Fourier transform of

the cosine signal at angular frequency ω_0 yields:

$$\tilde{x}_{DFT}(\omega_0) = \sum_{n=0}^{N-1} x_0 \cos(\omega_0 t_n) e^{-i\omega_0 t_n} = x_0 N/2 \tag{3.12}$$

where N is the total number of points in the digital signal, . The discrete Gabor transform (DGT) of $A\cos(\omega_0 t)$ at $\tau = 0$ is just the discrete Fourier transform (DFT) of the time signal after the multiplication of Gaussian window:

$$\tilde{x}_{DGT}(\omega_k) = \sum_{n=0}^{N-1} x_0 \cos(\omega_0 n) \frac{1}{\sqrt{2\pi}a} e^{-n^2/2a^2} e^{-i\omega_k n} \tag{3.13}$$

In order to obtain the correct peak value at the frequency of interest $\omega_k = \omega_0$, the amplitude correction factor A_w is multiplied with the discrete Gabor transform. Therefore, Eq. (3.13) with $\omega_k = \omega_0$ becomes:

$$\tilde{x}_{DGT}(\omega_0) = x_0 N \frac{\sum_{n=0}^{N-1} \cos(\omega_0 n) e^{-n^2/2a^2} e^{-i\omega_0 n}}{\sum_{n=0}^{N-1} e^{-n^2/2a^2}} \tag{3.14}$$

Writing the cosine function in terms of $(e^{i\omega_0 t} + e^{-i\omega_0 t})/2$, Eq. (3.14) is simplified into:

$$\tilde{x}_{DGT}(\omega_0) = \left(\frac{x_0 N}{2}\right)\left(\frac{\sum_{n=0}^{N-1} e^{-n^2/2a^2}(1 + e^{-i2\omega_0 n})}{\sum_{n=0}^{N-1} e^{-n^2/2a^2}}\right) \tag{3.15}$$

We further simplify Eq. (3.15)

$$\tilde{x}_{DGT}(\omega_0) = \left(\frac{x_0 N}{2}\right)\left(1 + \frac{\sum_{n=0}^{N-1} e^{-i2\omega_0 n}}{\sum_{n=0}^{N-1} e^{-n^2/2a^2}}\right) \tag{3.16}$$

It is clear from Eq. (3.16) that in the limit $a \to \infty$ for $\tilde{x}_{DGT}$approaches the discrete Fourier transform $\tilde{x}_{DFT}$ result. However, in this limit we lose temporal resolution. In order to accuratley approximate the discrete Fourier transform as discrete Gabor transform, we require the error in the Eq. (3.16) to be small i.e.:

$$\frac{\sum_{n=0}^{N-1} e^{-n^2/2a^2} e^{-i2\omega_0 n}}{\sum_{n=0}^{N-1} e^{-n^2/2a^2}} \ll 1 \tag{3.17}$$

The imaginary part of Eq. (3.17) is zero, since $\sum_{n=0}^{N-1} e^{-n^2/2a^2} \sin(2\omega_0 n)$ is zero because we are considering an odd function. Therefore, considering the error in the real part of Eq. (3.17) we require

$$\frac{\sum_{n=0}^{N-1} e^{-n^2/2a^2} \cos(2\omega_0 n)}{\sum_{n=0}^{N-1} e^{-n^2/2a^2}} \ll 1 \tag{3.18}$$

The nature of the cosine function in Eq. (3.18) conveys that the error in discrete Gabor transform is oscillatory. After amplitude correction, the error oscillates around the correct value (obtained from the DFT) with a frequency which is two times the frequency of the test signal. For large N, the error term can be approximated as:

$$\frac{\sum_{n=0}^{N-1} e^{-n^2/2a^2} \cos(2\omega_0 n)}{\sum_{n=0}^{N-1} e^{-n^2/2a^2}} \approx \frac{\int_{-\infty}^{\infty} e^{-n^2/2a^2} \cos(2\omega_0 n) dn}{\int_{-\infty}^{\infty} e^{-n^2/2a^2} dn} = e^{-2a^2\omega^2} \tag{3.19}$$

We set a tolerance limit of 10^{-6} for the oscillatory error in the discrete Gabor transform

$$e^{-2a^2\omega_0^2} \leq 10^{-6} \tag{3.20}$$

From here, we obtain an inequality between the window length and the frequency of the time signal in order to neglect the oscillatory error present in the discrete Gabor transform and approximate the transformed result as the discrete Fourier transform of the frequency of interest:

$$a \geq \frac{2.63}{\omega_0} \tag{3.21}$$

However, we have also seen that as the window length increases, time resolution decreases. Hence, to achieve optimal time resolution and frequency resolution we select

$$a = \frac{2.63}{\omega_0} \tag{3.22}$$

to be the optimal window length. The relationship between the window length and time resolution is demonstrated in Fig. 3-8. Fig. 3-8 shows the amplitude spectra calculated from discrete Gabor transform Fig. 3-4 (a) for a $\omega_0 = 1$ rad/s. The results from different window lengths are shown. As the window length decreases from $a = 26.3$ s to the optimal window length $a = 2.63$ s, the time resolution gets better. However, when the window

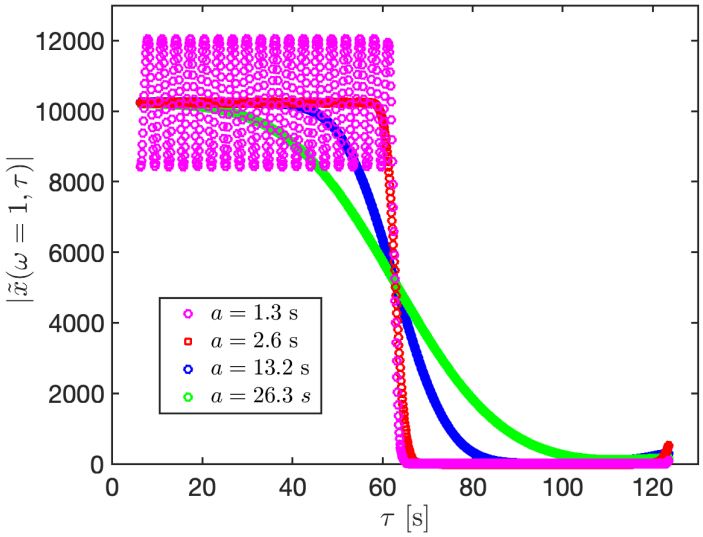

Figure 3-8: Time resolution of discrete Gabor transform at $\omega_0 = 1$ rad/s of the signal in Fig. 3-4 (a) for different window lengths. As the window length gets smaller, the temporal resolution gets better. But when the window length becomes less than $a = 2.63/\omega_0$, where ω_0 is the frequency of the imposed sinusoid, the oscillatory error which oscillates at $2\omega_0$ starts to dominate and is shown by the magenta data points.

length is reduced even further and the inequality in Eq. (3.21) is not satisfied, we observe the growth of an oscillatory error with a frequency of $2\omega_0$ as expected from Eq. (3.18). If a multiwave time signal [104] which has multiple frequencies are considered, the ω_0 in the Eq. (3.22) should be the lowest frequency present in the signal so that the inequality in Eq. (3.21) is obeyed for all frequencies present in the original time signal $x(t)$. The time frequency uncertainty involved in extracting time and frequency information using Gabor transform is discussed in Appendix B.

3.4 Applications of Gabor transform

3.4.1 Extracting time dependent complex moduli

In the previous subsections, the discrete Gabor transform was introduced to overcome the limitations of the discrete Fourier transform specifically the absence of time resolution and assumption of time translation invariance. Data processing techniques for amplitude correction and identifying the optimal window length were discussed to enable use the

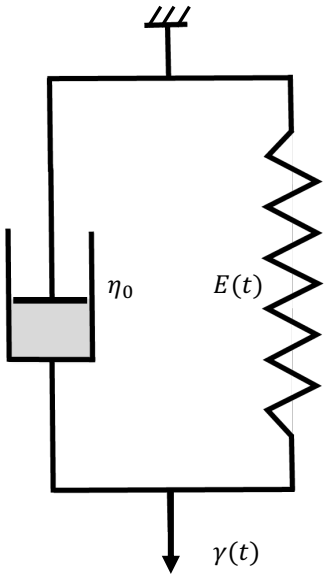

Figure 3-9: An aging or time-evolving Kelvin Voigt model is illustrated. It is a mechanical model with a dashpot and spring in parallel configuration representing the viscous and elastic mode respectively. The total output stress for an applied strain for the Kelvin Voigt model can be written as $\sigma(t) = E\gamma(t) + \eta_0\dot{\gamma}(t)$ where $E(t)$ is the modulus of the spring at time t and η_0 is the constant damping coefficient of the dashpot which is equivalent to the viscosity.

discrete Gabor transform to obtain accurate data. Now, we consider various applications of the discrete Gabor transform in rheometry. The discrete Gabor transform can be used for extracting time dependent complex moduli data for thixotropic and aging materials, or more generally known as mutating materials [74]. For such mutating materials, the time and frequency dependent complex moduli can be generally defined as:

$$G^*(\omega,\tau) = \frac{\tilde{\sigma}_{STFT}(\omega,\tau)}{\tilde{\gamma}_{STFT}(\omega,\tau)} \tag{3.23}$$

where $\tilde{\sigma}_{STFT}$ is the short time Fourier transform of the stress signal and $\tilde{\gamma}_{STFT}$ is the short time Fourier transform of the strain signal.

To demonstrate the aplpications of this idea, we consider an aging Kelvin Voigt model [15] as shown in Fig. 3-9 to demonstrate the capabilities of extracting time dependent moduli using Gabor transform. The Kelvin Voigt model [24] is a mechanical model in which the spring is in parallel with a dashpot as shown in Fig. 3-9. The aging Kelvin Voight model with a time-varying modulus and a constant viscosity has been used by Coussot [15]

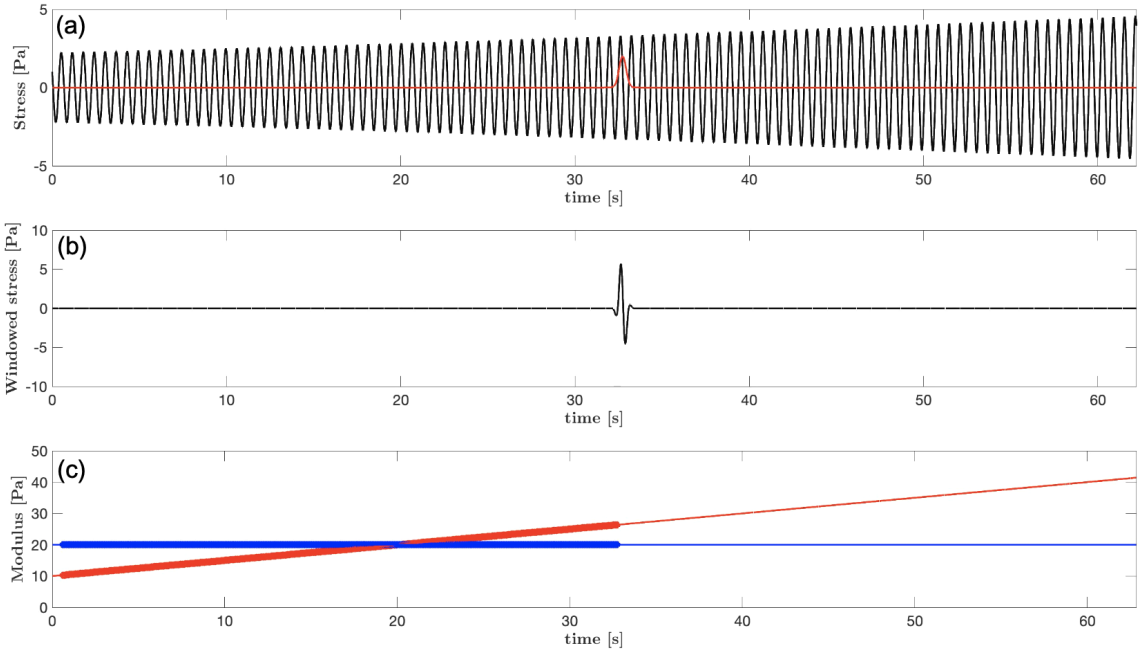

Figure 3-10: (a) The output stress from the aging Kelvin Voigt model given by Eq. (3.24) and Eq. (3.25) for an input of $\gamma(t) = \gamma_0 \sin(\omega_0 t)$ where $\gamma_0 = 0.1$ and $\omega_0 = 10$ rad/s is illustrated by the black solid line. The Gaussian with $a = 0.263$ s window which traverses across the output signal is represented by the red solid line at $\tau = 32$ s. (b) The windowed signal in time multiplied by the Gaussian window at $\tau = 32$ s is plotted (c) The time dependent complex moduli for $\omega_0 = 1$ rad/s is plotted. The red solid line and the red data points show reqpectively the analytical solution and data obtained from the discrete Gabor transform (DGT) for the storage modulus. Similarly, the blue solid line and the blue data points represent the analytical solution and the data for the loss modulus obtained from DGT.

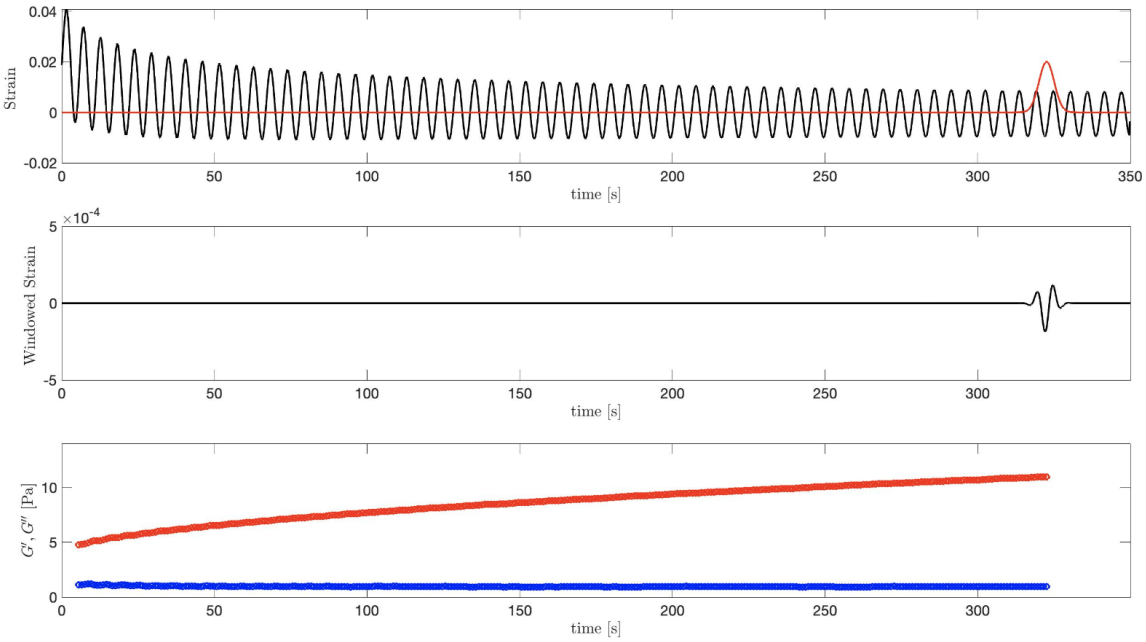

Figure 3-11: (a) The output strain from 5% bentonite dispersion for an input of $\sigma(t) = \sigma_0 sin(\omega t)$ is plotted using black solid line and the Gaussian window $a = 2.63$ s which traverses across the output time signal is represented by red solid line. (b) The windowed signal along time as Gaussian window progresses is plotted for $\tau = 320$ s. (c) The time dependent complex modulus for $\omega_0 = 1$ rad/s is shown. The red data points and the blue data points represent the storage and loss modulus data obtained from DGT respectively.

for modeling the aging behavior of Bentonite clay, and the constitutive response can be written in the form

$$\sigma(t) = E(t)\gamma(t) + \eta_0\dot{\gamma}(t) \tag{3.24}$$

For the purpose of demonstration, we set the viscosity $\eta_0 = 2\ Pa \cdot s$ and allow the modulus to be a linear function of time.

$$E(t) = 10 + 0.5t \tag{3.25}$$

The storage modulus and the loss modulus for time-varying Kelvin Voigt model can be expressed analytically as:

$$G'(\omega, \tau) = E(t) = 10 + 0.5t \tag{3.26}$$

$$G''(\omega, \tau) = \eta_0\omega_0 \tag{3.27}$$

An oscillatory strain signal of the form $\gamma(t) = \gamma_0 \sin(\omega_0 t)$ with $\gamma_0 = 0.1$ and $\omega_0 = 10\ rad/s$ is used as the input to the aging Kelvin Voigt model. The output stress is calculated from Eq. (3.24) and is plotted in Fig. 3-10 (a). The amplitude of the stress signal increases linearly with time since the modulus increases linearly with time. The phase of the signal also shifts with time due to the decreasing phase angle $\delta(t) = \tan^{-1}(\eta_0/E(t))\,\omega_0$ but this is difficult to discern from a plot such as Fig. 3-10.

To find the time dependent complex moduli from the output stress signal and the input strain signal using Discrete Gabor transform, Gaussian window of window length $a = 2.63/\omega = 0.263\ s$ is sent along the output signal as shown by the red solid line in Fig. 3-10 (a). The Gaussian window traverses the output stress signal and as it travels across the signal, the windowed stress i.e. the product of the stress $\sigma(t)$ and the Gaussian window $g(t - \tau)$ at every discrete time instant is calculated. The windowed stress is shown in Fig. 3-10 (b) at time $\tau = 32$ s. Thus time resolution is obtained by the moving Gaussian window. The time-resolved discrete Gabor transform corresponding to the discrete Fourier transform of this windowed signal at every discrete time instant is calculated. This process is also followed for the input strain signal as well, and using Eq. (3.23), the time-dependent complex modulus is obtained and is plotted in Fig. 3-10 (c). The storage modulus (red data points) and the loss modulus (blue data points) calculated using the discrete Gabor

transform (up to the point $\tau = 32$ s) are in excellent agreement with the analytical solution of the storage and loss modulus represented by red and blue solid line respectively in Fig. 3-10 (c).

We now consider application of the DGT to experimental data using a 5 wt.% Bentonite dispersion, a soft glassy material. Here, we consider an oscillatory stress input of $\sigma = \sigma_0 \sin(\omega t)$ is applied where $\sigma_0 = 0.1\ Pa$ and $\omega = 0.37\ rad/s$. The output oscillatory strain is shown in Fig. 3-11 (a). Following the same procedures mentioned for extracting time dependent complex moduli for the Kelvin Voigt model, we obtain the time dependent complex moduli for the Bentonite dispersion. The storage modulus (red data points) increases logarithmic with aging time as seen in Fig. 3-11 (c). This demonstrates the physical aging behavior of this soft glassy material. There is no dependence of loss modulus on aging time for bentonite, indicating that the material becomes more elastic or solid-like with time but it's linear viscous response remains the same.

3.4.2 Extracting transient modulus and compliance in startup of flow

Measuring the transient response during the start up of shear flow is common in stress controlled rheometry. The secular term (transient + offset from zero) is dominant at the inception of the oscillatory flow brings disorder to the signal and results in measurement errors of steady flow properties. Hence, the conventional procedure for measuring the steady state compliance J' & J'' is by waiting for the transient response to diminsh and then the data recording is started. This results in loss of initial transient data. Therefore, we demonstrate using discrete Gabor transforms to obtain the transient data as well as steady state data simultaneously with accuracy. To illustrate the approach, we consider a two mode Maxwell model which consists of two series of spring and dashpot in parallel as shown in Fig. 3-12 for which the analytical results for transient response for start up of oscillatory stress [42, 61]. The input to a two mode Maxwell model is given by $\sigma = \sigma_0 \sin(\omega t + \psi)$. The output strain for the start-up flow is:

$$\gamma(t) = \sigma_0 \Big(J'(\omega) \sin(\psi + \omega t) - J''(\omega) \cos(\psi + \omega t) \Big) + \sigma_0 \frac{cos(\psi)}{\omega(\eta_1 + \eta_2)} + \gamma_t \tag{3.28}$$

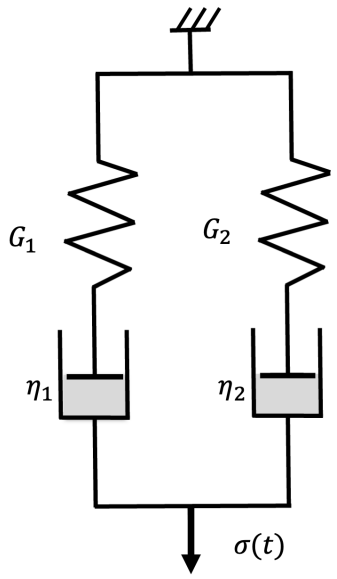

Figure 3-12: The two mode Maxwell model is a parallel combination of two sets of Maxwell models in parallel configuration. The relaxation times are $\tau_1 = \eta_1/G_1$ and $\tau_2 = \eta_2/G_2$.

Now, the transient term can be written as:

$$\gamma_t = \sigma_0 \frac{(\omega\lambda\cos(\psi) - \sin(\psi))\eta_1\eta_2(\tau_1 - \tau_2)^2}{(1 + (\lambda\omega)^2)(\eta_1 + \eta_2)^2(\tau_1\eta_2 + \tau_2\eta_1)} e^{-t/\lambda} \tag{3.29}$$

The retardation time for the two mode Maxwell mode is

$$\lambda = \frac{\eta_1\tau_2 + \eta_2\tau_1}{\eta_1 + \eta_2} \tag{3.30}$$

The secular term comprises of the offset from zero and the transient term in Eq. (3.28). The model parameters for the demonstration are chosen as follows: $\sigma_0 = 1\ Pa$, $\eta_1 = 1\ Pa \cdot s$, $\eta_1 = 10\ Pa \cdot s$, $\tau_1 = 10\ s$, $\tau_1 = 0.01\ s$, $\omega = 52\ rad/s$ and $\psi = 0$.

To evaluate the steady state and the transient terms, the Gaussian window with $a = 0.07$ s is translated along the time signal as illustrated in Fig. 3-13 (a) and the discrete Gabor transform is calculated. The contribution to the secular term at each τ corresponds to the DC ($\omega = 0$) component in the discrete Gabor transform and the complex compliance $J^*(\omega)$ is the component of discrete Gabor transform which corresponds to the frequency of the

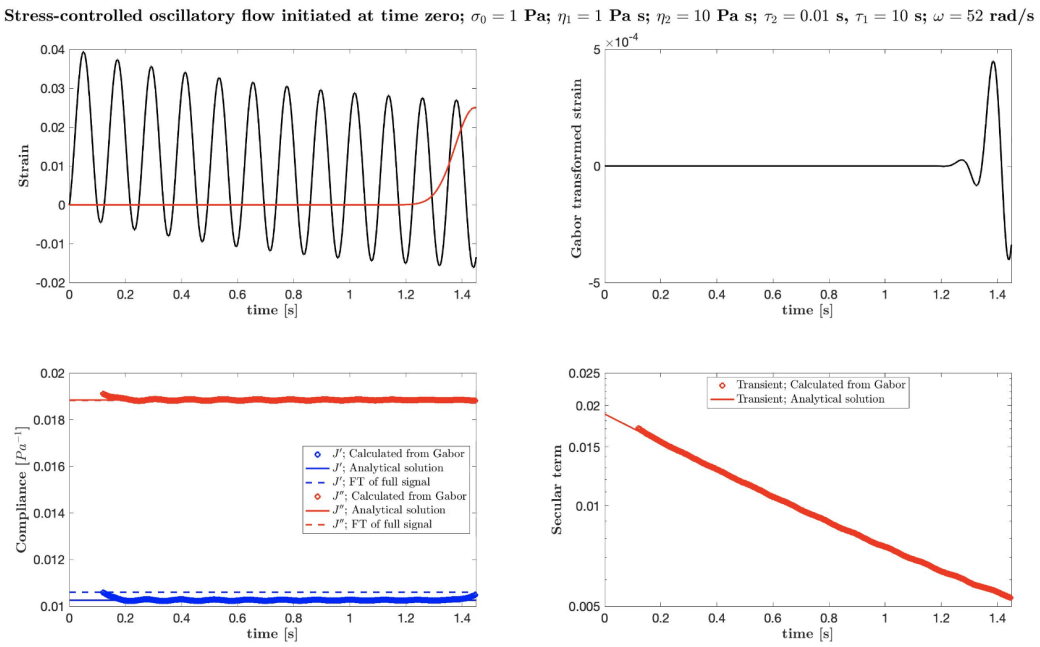

Figure 3-13: (a) The black solid line represents the output strain following initiation of small amplitude oscillatory stress at $t = 0$ with $\psi = 0$ and the red solid line shows the traversing Gaussian window ($a\omega = 3.6$) with time. (b) The windowed signal as the Gaussian window progresses in time is represented (c) The red and blue data points show the elastic and viscous compliance from DGT respectively. The red and blue dashed lines represent the elastic and viscous compliance calculated from DFT considering the entire time signal in (a). The red and blue solid lines represent the analytical solution for the elastic and viscous compliance respectively for the two mode Maxwell given by Eq. (3.28) with the specified parameters. (d) The secular term data obtained from DGT is shown using red data points and the analytical solution for the secular term is represented by red solid line.

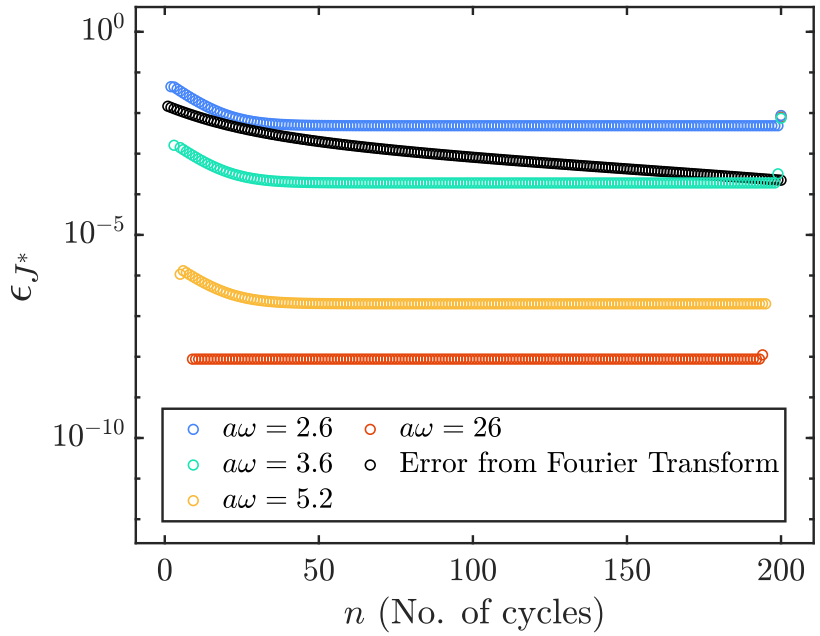

Figure 3-14: The error in calculating the complex compliance for different window lengths from DGT and from DFT decreases as the total number of cycles n considered for the calculation of the transform increases. The error converges quickly when using the DGT and the final convergence value varies systematically with the window length. As the window length increases, the error decreases but the temporal resolution for the initial transitient also decreases.

input time signal. Both the secular and the steady state terms are plotted in Fig. 3-13 (c) and (d) respectively. The error in the steady state compliance is defined as:

$$\epsilon = \left| \frac{|J^*| - J_{analytical}}{J^*_{analytical}} \right| \tag{3.31}$$

For different window lengths $a = 2.63 * m/\omega$, where $m = 1, 1.5, 2, 3$ and for a fixed value of $\omega = 52\ rad/s$, ϵ is calculated using the parameter values given above and the resulting error is shown in Fig. 3-14 as a function of number of cycles (n) of the output strain signal which is considered for the calculation of the steady state complex compliance. It can be observed from Fig. 3-14, that the error in discrete Gabor transform decreases more rapidly than the error from the discrete Fourier transform. The error plateau decreases as the window length is increased and there is more flexibility for the window length in this application since there is no time dependence here and hence time resolution is not given

importance.

3.4.3 Rapid extraction of non-linear Fourier/ Chebyhev coefficients

Another application of Gaborheometry is in the rapid construction of a Pipkin diagram for a complex fluid. In the linear viscoelastic regime, to obtain data across different frequencies, Optimally windowed Chirps (OWCh) can be used [35, 36]. In the medium amplitude regime, MAPS protocols have been developed recently [63, 64]. In the non-linear regime, the material functions for a complex fluid are functions of both frequencies and input strain amplitude. Therefore, the conventional techniques which have been used to probe the Pipkin diagram in this regime are Medium Amplitude Oscillatory Shear (MAOS) and Large Amplitude Oscillatory Shear (LAOS). In these methods, a sinusoidal signal with a user-specified amplitude and frequency is selected as input strain signal [25, 30].

$$\gamma(t) = \gamma_0 \sin(\omega t) \tag{3.32}$$

This corresponds to a single coordinate point in the Pipkin diagram represented schematically in Fig. 3-15. The output stress in the non-linear regime can then be written in terms of the Fourier series.

$$\sigma(t) = \gamma_0 \sum_{n:odd} G'_n(\omega, \gamma_0) \sin(n\omega t) + G''_n(\omega, \gamma_0) \cos(n\omega t) \tag{3.33}$$

where $G'_n(\omega, \gamma_0)$ and $G''_n(\omega, \gamma_0)$ are the elastic and viscous non-linear Fourier coefficients respectively. When $\gamma_0 \to 0$, (i.e. in the linear regime) we expect $G'_1(\omega, \gamma_0) = G'(\omega)$ and $G''_1(\omega, \gamma_0) = G''(\omega)$. The output stress can also be written in terms of Chebyshev polynomials [29, 25, 26, 28]

$$\sigma(t) = \gamma_0 \sum_{n:odd} e_n(\omega, \gamma_0) T_n(\gamma/\gamma_0) + \dot{\gamma}_0 \sum_{n:odd} v_n(\omega, \gamma_0) T_n(\dot{\gamma}/\dot{\gamma}_0) \tag{3.34}$$

where T_n is the nth order Chebyshev coefficient. The e_n coefficients are referred as the elastic Chebyshev coefficients and the v_n values are the viscous Chebyshev coefficients. The relationship between the elastic and viscous Fourier and the Chebyshev coefficients

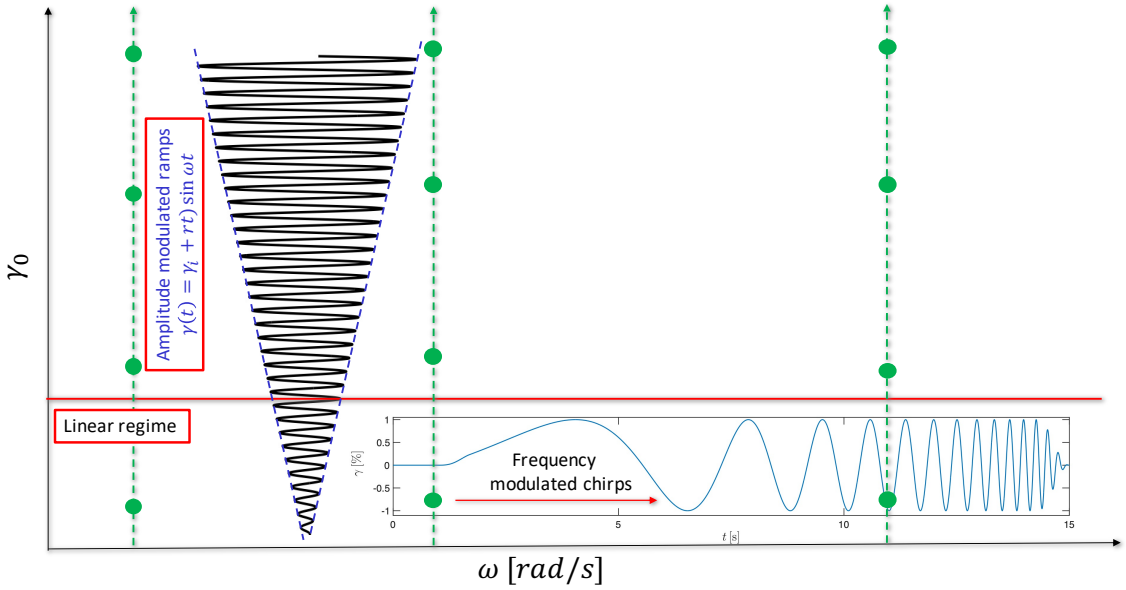

Figure 3-15: General representation of the Pipkin space for a complex fluid in terms of frequency ω and strain amplitude γ_0. Frequency modulated chirps serve as a quick way to obtain the linear frequency response. The conventional way of obtaining non-linear Fourier/ Chebyshev coefficients by specifying a single point γ_0, ω shown by each green point and then imposing a strain input of the from given in Eq. (3.32) can be time consuming. The quick way of obtaining non-linear Fourier/ Chebyshev coefficients for a specified deformation frequency using amplitude modulated ramps to construct the Pipkin diagram is illustrated.

are given by

$$e_n = G'_n(-1)^{(n-1)/2} \tag{3.35}$$

$$v_n = G''_n/\omega \tag{3.36}$$

These non-linear Fourier and Chebyshev coefficients can be determined for different input strain amplitudes and frequencies as shown by the green data points in Fig. 3-15. Therefore, for a particular frequency of deformation, in order to find the dependence of $G'_n(\omega, \gamma_0)$ or $G''_n(\omega, \gamma_0)$ on strain amplitude or just to plot these non-linear Fourier coefficients against strain amplitude, one can take many LAOS experiments at various amplitudes but probing the entire Pipkin diagram can be time consuming.

We thus consider using an amplitude modulated input signal to perform a slow amplitude sweep at a specified deformation frequency and then using Gaborheometry to extract the strain evolving Fourier coefficients as a function of input amplitude from a single experiment. This is schematically represented using the vertical oscillatory solid line in Fig. 3-15. This technique reduces the number of experiments required to probe the Pipkin diagram and the post processing time as well. Using Gaborheometry, we can obtain the dependence of these non-linear Fourier-Chebyshev coefficients on input strain amplitude for a specified deformation frequency from a single experiment i.e. values of $G'_n(\omega, \gamma)$ or $G''_n(\omega, \gamma)$ or equivalently e_n and v_n for a specified frequency can be plotted against strain amplitudes from a single experiment.

To demonstrate this technique, we consider a linear amplitude modulated input strain signal with modulation rate r.

$$\gamma(t) = \gamma_i\,(1 + rt/\gamma_i)\sin(\omega t) \tag{3.37}$$

where γ_i is the initial amplitude of the modulated signal. The Gaussian window which is passed over the time signal calculates the windowed signal over a window length set by the value of a. In a single oscillatory cycle, the input strain amplitude should not change significantly, so that we can approximate the oscillatory windowed output signal as a result

of an approximately constant input amplitude. Therefore, to obtain a relevant constraint, at any time instant t, we require

$$\frac{\gamma_i + r(t + (2\pi/\omega))}{\gamma_i + rt} \approx 1 \tag{3.38}$$

or equivalently

$$\frac{2\pi}{\omega}\frac{r}{\gamma_i + rt} \ll 1 \tag{3.39}$$

This dimensionless ratio controls the rate of change of the driving signal and may be considered as a dimensionless ramprate. The examples considered in sections 3.4.1 and 3.4.2 correspond to $r = 0$. We may set a tolerance limit and expect that the non-linear coefficients determined for a given amplitude $\gamma_i + rt$ at a particular time t, is accurate when

$$Mu_{amp} = \frac{2\pi}{\omega}\frac{r}{\gamma_i + rt} \leq 0.1 \tag{3.40}$$

To demonstrate this technique for obtaining the non-linear Fourier or Chebyshev coefficients from a single experiment, we consider the K-BKZ-Wagner constitutive model.

$$\sigma(t) = \int_{-\infty}^{t} M(t - t')h(\gamma(t, t'))\gamma(t, t')dt' \tag{3.41}$$

where $M(t - t')$ is the memory function and $h(\gamma)$ is the damping function which introduces the non-linearity when the strain amplitude increases. Here, we consider a damping function of $h(\gamma) = 1 + A\gamma^2$ where A is the leading order damping coefficient. Here, for demonstration purpose, we consider the memory function to simply follow single mode Maxwell response.

$$M(t - t') = \frac{\eta}{\lambda^2}e^{-\frac{t-t'}{\lambda}} \tag{3.42}$$

η being the zero shear viscosity and λ is the relaxation constant of the model material. The numerical values for all the parameters used in this KBKZ simulation are: $\eta = 1\ Pa \cdot s$, $\lambda = 2\ s$ and $A = -0.6$. The amplitude modulated input signal considered here is

$$\gamma(t) = (\gamma_i + rt)\sin(\omega t) \tag{3.43}$$

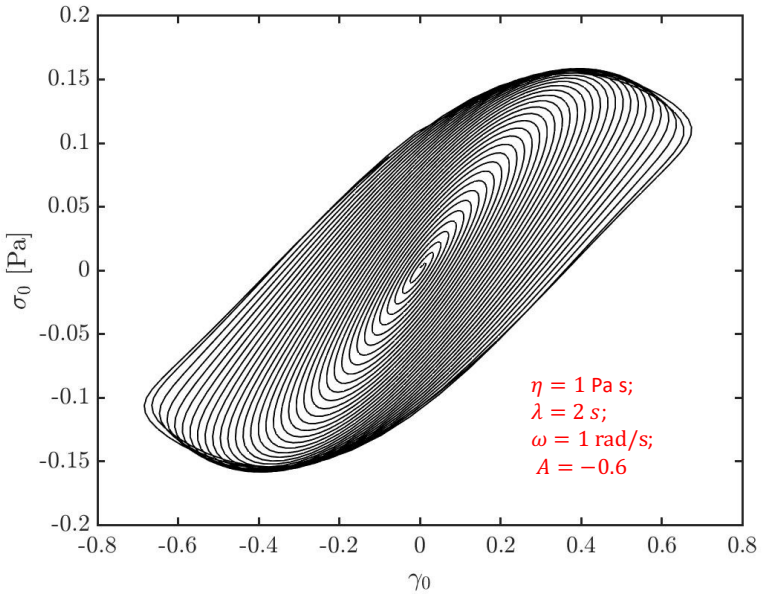

Figure 3-16: The Lissajous curve for an amplitude modulated input strain given by $\gamma = (\gamma_i + rt)\sin(\omega t)$ where $\gamma_i = 0.01$, $r = 0.003$ and $\omega = 1$ rad/s to a KBKZ-Wagner constitutive equation with a single mode Maxwell modulus characterized by parameters η and λ in the memory function and a simple quadratic damping function $h(\gamma) = 1 + A\gamma^2$ as the damping function.

Here we consider the initial strain amplitude is 1% or 0.01, $r = 0.003$, total time $t_f = 226$ s and the specified frequency of deformation is $\omega = 1\ rad/s$. The input strain in Eq. (3.43) is substituted in Eq. (3.41) with the specified memory functions and the damping function to obtain the output stress. The resulting continously varying Lissajous curve representing the response between the output stress and the input amplitude-modulated strain for the KBKZ-Wagner model with the specified parameters is shown in Fig. 3-16. As, we show above, this curve is all that is needed to calculate the evolution in the Fourier/Chebyshev coefficients evolution with strain amplitude.

The corresponding output stress time series is shown in Fig. 3-17 (a). The Gaussian window $g(t-\tau)$ with $a\omega = 2.63$ is sent along the time signal and the windowed signal at every time instant $t - \tau = 0$ corresponds to the input strain signal of amplitude $\gamma_i + r\tau$. The discrete Fourier transform of the windowed signal at every time instant τ which corresponds to the amplitude $\gamma_0 = \gamma_i + r\tau$ is calculated. The real and imaginary part of nth harmonic component of the calculated transform with the time resolution τ corresponds to

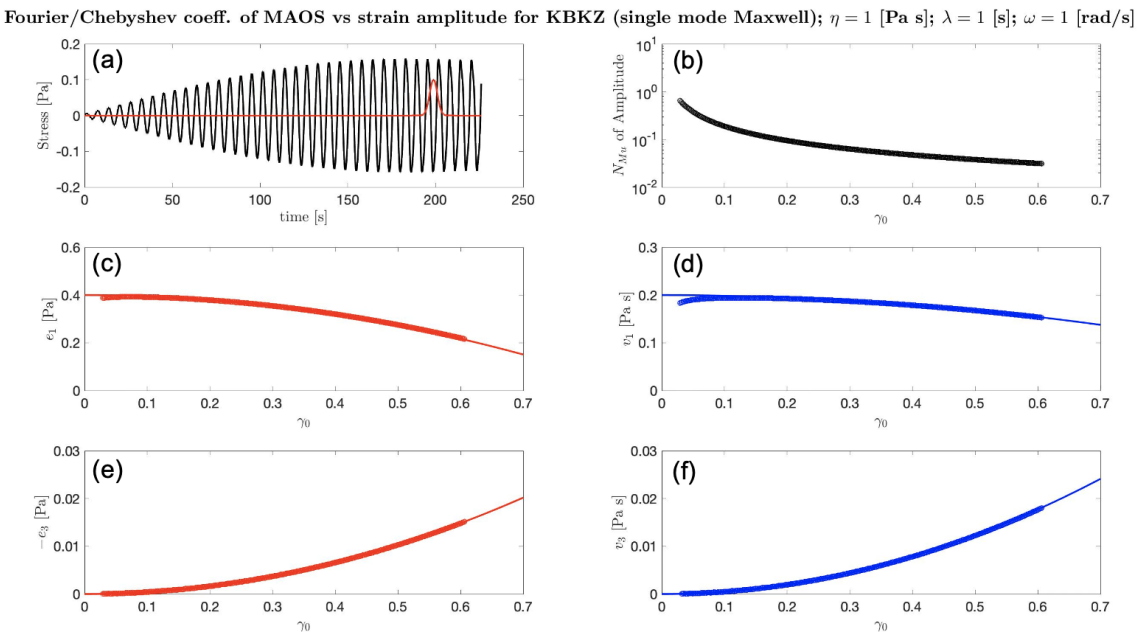

Figure 3-17: (a) Output stress represented by black solid line is from amplitude modulated strain input, $\gamma = (\gamma_i + rt)\sin(\omega t)$ where $\gamma_i = 0.01$, $r = 0.003$ and $\omega = 1$ rad/s to a KBKZ-Wagner constitutive equation with a single mode Maxwell with parameters η and λ as a memory function and $h(\gamma) = 1 + A\gamma^2$ as the damping function, where $A = -0.6$. The red solid line indicates the Gaussian window at $\tau = 200$ s which traverses across different stress amplitudes. (b) The plot shows the Mutation number of input amplitude at different strain strain amplitudes. (c) The plot represents e_1. The data points are obtained from DGT and the solid lines represents the analytical solution. (d) The plot represents v_1. The data points are obtained from DGT and the solid lines represents the analytical solution. (e) The plot represents e_3. The data points are obtained from DGT and the solid lines represents the analytical solution. (f) The plot represents v_3. The data points are obtained from DGT and the solid lines represents the analytical solution.

$G'_n(\omega, \gamma_i + r\tau)$ and $G''_n(\omega, \gamma_i + r\tau)$ respectively. These Fourier coeffecients can also be interchanged to the corresponding elastic and viscous Chebyshev coefficients using Eq. (3.35) and Eq. (3.36) respectively. The values of e_1, e_3 and v_1, v_3 computed obtained from the discrete Gabor transform are plotted as red and blue points respectively in Fig. 3-17 (c), (d), (e) and (f). The analytical solution for e_1, e_3, v_1, v_3 for the KBKZ-Wagner model with single model Maxwell kernel and a damping function of form $h(\gamma) = 1 + A\gamma^2$ has been derived by Martietti *et al.* [68]:

$$e_1(\omega, \gamma_0) = G_0 \frac{De^2}{1 + De^2} + G_0 A \gamma_0^2 \frac{9De^4}{(1 + De^2)(1 + 4De^2)} \tag{3.44}$$

$$v_1(\omega, \gamma_0) = \frac{G_0}{\omega} \frac{De}{1 + De^2} + G_0 A \lambda \gamma_0^2 \frac{9/2De^2}{(1 + De^2)(1 + 4De^2)} \tag{3.45}$$

$$e_3(\omega, \gamma_0) = G_0 A \gamma_0^2 \frac{9De^4(De^2 - 1)}{(1 + De^2)(1 + 4De^2)(1 + 9De^2)} \tag{3.46}$$

$$v_3(\omega, \gamma_0) = G_0 A \lambda \gamma_0^2 \frac{3/2De^2(1 - 11De^2)}{(1 + De^2)(1 + 4De^2)(1 + 9De^2)} \tag{3.47}$$

where $De = \lambda\omega$ and $G_0 = \eta/\lambda$. The analytical solution of e_1, e_3, v_1 and v_3 are plotted using red and blue solid lines in Fig. 3-17 (c), (d), (e) and (f). It is clear that the data points obtained using the Gabor transform techniques at each value of τ corresponding to a strain $\gamma_0 = \gamma_i + r\tau$ are in good agreement with the analytical solution for the non-linear Chebyshev or Fourier coefficients. Close inspection shows that there is a small but systematic deviation at early times which initially seems puzzling since the input strain amplitude is smallest here. This can be explained by considering the mutation number Mu_{amp} defined in Eq. (3.40). Because γ_i is small (0.01), initially the dimensionless ramp rate is large. When the dimensionless ramp rate plotted in Fig. 3-17 (b) becomes less than 0.1 as time evolves. This informs us to choose the ramp rate of amplitude modulation carefully in-order to get accurate results of the non-linear Fourier or Chebyshev coefficients using Gabor transform techniquesn from a single experiment for a specified deformation frequency.

3.5 Discussion

In this chapter, we have shown how the discrete Gabor transform, which is a special case of short time Fourier transform with a Gaussian window specified by standard deviation a can provide time resolution to non-ergodic systems. Important data processing techniques such as appropriate amplitude correction and optimal window length selection has been discussed to use the discrete Gabor transform techniques for rheometry. An important criteria while processing recorded oscillatory data using these discrete transform related techniques is periodicity. Periodicity of the time signal should be ensured before using discrete Fourier transform or discrete Gabor transform to avoid spectral leakage. In section 3.3.3, we also showed that the optimal window length selection is set $a = 2.63/\omega_0$ in order to obtain sufficient time and frequency resolution, where ω_0 is the lowest fundamental frequency present in the input signal. We observed that decreasing the window length in order to increase the time resolution can lead to significant oscillatory error with the error oscillating with twice the frequency of the input time signal. To obtain further increased time resolution, one potential option is to use a smaller window length, which is less than $a = 2.63/\omega_0$ and then passing the output of the discrete Gabor transform output through a low band pass filter with cutoff frequency less than $2\omega_0$ in order to filter out the oscillatory error in the output. Care of course must be exercised here to ensure the amplitude of the filtered signal is preserved (or corrected) or the computed modulus will be in error.

The applications of the discrete Gabor transform in rheometry shown here are: extracting time dependent complex moduli for mutating materials, extracting transient and steady state ocillatory terms from start-up of flow and obtaining the non-linear elastic and viscous Fourier or Chebyshev coefficients dependence on input amplitude for a specified frequency ω_0 by using an amplitude modulated (AM) signal to perform a slow amplitude sweep together with a Gaussian window (of optimal window size $a\omega_0 = 2.63$) to localize the time signal at each time τ with different amplitudes $\gamma_0(\tau)$. Note that we require Eq. (3.40) to be accurate to extract the nonlinear Fourier-Chebyshev coefficients. In the section 3.4.3, we demonstrated this technique using a non-mutating KBKZ-Wagner constitutive model. We observed that the dimensionless ramp rate plays an important role in the accuracy of the

non-linear measurements using the discrete Gabor transform technique.

Finally, we discuss here the potential of extending this technique for mutating materials as well. To explore this systematically, we consider a suitable "toy model" composed of a mutating non-linear model of Kelvin-Voigt form [26]:

$$\sigma(t) = f(\gamma, t)\gamma + g(\dot{\gamma})\dot{\gamma} \tag{3.48}$$

$$f(\gamma, t) = G_0 + G_\beta(t)\left(\frac{\gamma}{\gamma^*}\right)^2 \tag{3.49}$$

$$g(\dot{\gamma}) = \eta_0 - \eta_\beta\left(\frac{\dot{\gamma}}{\dot{\gamma}^*}\right)^2 \tag{3.50}$$

where $f(\gamma, t)$ is the non-linear elastic coefficient. γ^* is the critical strain beyond which non-linear elastic effects become significant. Similarly $g(\dot{\gamma})$ is the non-linear viscous coefficient, and $\dot{\gamma}^*$ is the critical strain rate beyond which the non-linear elastic effects become significant. In order to introduce time-dependence or rheological aging, we make G_β, which is the coefficient of non-linear response in $f(\gamma)$ a function of time where $G_\beta = c_0 + c_1 t$. Therefore, the non-linear elastic Chebyshev or Fourier coefficients and the non-linear viscous Chebyshev or Fourier coefficients results in:

$$e_1 = G_1' = G_0 + \frac{3}{4}\left(\frac{\gamma_0}{\gamma^*}\right)^2 G_\beta(t) \tag{3.51}$$

$$e_3 = -G_3' = \frac{1}{4}\left(\frac{\gamma_0}{\gamma^*}\right)^2 G_\beta(t) \tag{3.52}$$

$$v_1 = G_1''/\omega = \eta_0 - \frac{3}{4}\left(\frac{\dot{\gamma}_0}{\dot{\gamma}^*}\right)^2 \eta_\beta \tag{3.53}$$

$$v_3 = G_3''/\omega = -\frac{1}{4}\left(\frac{\dot{\gamma}_0}{\dot{\gamma}^*}\right)^2 \eta_\beta \tag{3.54}$$

where

$$G_\beta(t) = c_0 + c_1 * t \tag{3.55}$$

The parameters of the model are: $G_0 = 5\ Pa$, $\gamma^* = 2$, $\eta_0 = 7\ Pa \cdot s$, $\eta_\beta = 3\ Pa \cdot s$, $\dot{\gamma}^* = 3\ s^{-1}$ and $c_0 = 4$ Pa. The non-linear elastic properties of this hypothetical material changes

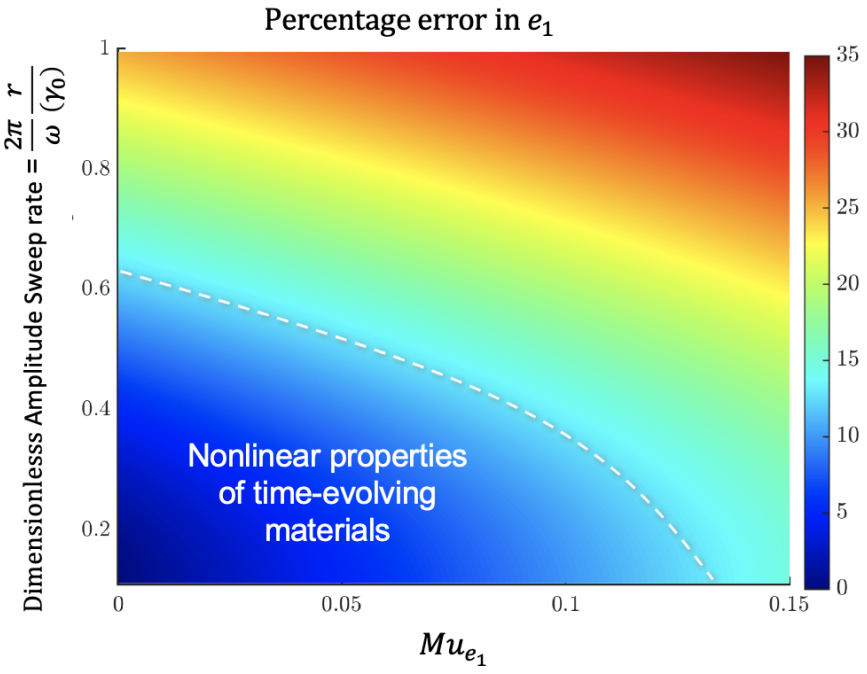

Figure 3-18: Error plot of e_1 for the non-linear Kelvin Voigt model for different mutation number of the material properties and various amplitude ramp rates (Mutation number of input amplitude). The dashed line indicates the 10% error contour. The area within the contour indicates the operability regime of DGT in using amplitude modulated ramps for mutating materials.

with time. We vary the parameter c_1 to find the dependence on mutation of the material and the measurement error in the non-linear Fourier or Chebyshev coefficients while using the Gaborheometry technique. We consider the error in e_1 for various mutation number for e_1 and various dimensionless ramp rate of the amplitude modulated signal. For the error in e_1, the initial state i.e. the value of e_1 at $t = 0$ is considered here as the correct or expected property. Therefore the mutation time of the property e_1 which is the characteristic time for the change of the material property is given as:

$$\lambda_{Mu} = \left[\frac{1}{e_1} \frac{\Delta e_1}{\Delta t} \right] \tag{3.56}$$

where Δe_1 is the change in property e_1 from its initial state and Δt is the time taken to reach the change in property. The experimental time taken to measure the interested data point using the discrete Gabor transform is Δt as well. Therefore, the mutation number for e_1 for this toy model is

$$Mu_{e_1} = \frac{\Delta e_1}{e_1} \tag{3.57}$$

We choose a amplitude modulated signal $\gamma(t) = (\gamma_i + rt)\sin(\omega t)$ with where $\gamma_i = 0.01$ to demonstrate the potential of Amplitude modulated (AM) sweeps for LAOS in mutating materials. The dimensionless rate of change or the mutation number of this AM signal can be written as

$$Mu_{Amp} = \frac{2\pi}{\omega} \frac{r}{\gamma_i + rt} \tag{3.58}$$

The variables c_1 in Eq. (3.55) and r in Eq. (3.58) are varied in order to simulate the error in e_1 for a range of mutation numbers for the model material and the dimensionless ramp rate given by Eq. (3.58) while using our discrete Gabor transform amplitude sweep technique. In Fig. 3-18 we show a contour plot the surface plot of the percentage error incurred by determining e_1 for various values of the mutation number Mu_{e_1} of the material and for a range of dimensionless ramp rate. It is evident that as the material mutation and the ramp rate also decreases towards zero, we obtain increasingly exact values of $e_1(\gamma_0)$. The dashed line in Fig. 3-18 shows the contour line corresponding to percentage error of 10%. The area within the contour line indicates the operability window within which we can use discrete

Gabor transform techniques to obtain the non-linear Fourier-Chebyshev coefficients even for a mutating material. We show here the glimpse of extending this technique to mutating materials but the details are yet to be explored.

There are three applications of discrete Gabor transform discussed in this chapter. But there are many more applications of this technique in rheometry which we leave for the readers to explore.

Chapter 4

Rheological Characterization of Bentonite Dispersions

4.1 Introduction

Bentonite dispersions are widely used as drilling fluids in oil and gas industries for their shear thinning and thixotropic properties. These materials exhibit soft glassy behavior [15] which makes them difficult to characterize rheologically. Bentonite is a discotic Montmorillonite clay with Na^+ cations on the surface. The chemical formula for Na^+-montmorillonite can be written as $Na_{0.33}[(Al_{1.67}Mg_{0.33})(O(OH))_2(SIO_2)_4]$. The chemical structure of bentonite dispersion comprises of tetrahedral structures with silicon and aluminum ions in the center and octahedral structures with aluminum and magnesium ions in the center. The corners of both the structures are comprised of oxygen atoms and hydroxyl groups [76, 38]. The octahedral structure is packed in-between two tetrahedral layers as shown in Fig. 4-1 and the surface of the tetrahedral layers comprises of Na^+ cations and water. The spacing between the two tetrahedral layers which comprises of exchangeable cations and water is generally 10-20 Å[67]. The bentonite clay particles (when not dispersed in water) are generally 6-200 μm in size [101]. The SEM images of Wyoming bentonite particles are shown in Fig. 4-2. Fig. 4-2 (a) shows the SEM scale with 2 μm and Fig. 4-2 (b) shows the SEM scale with 100 μm. These clay particles when dispersed in water exfoliate into disc-shaped platelets. The major axis of the platelets (large dimension) is approximately around

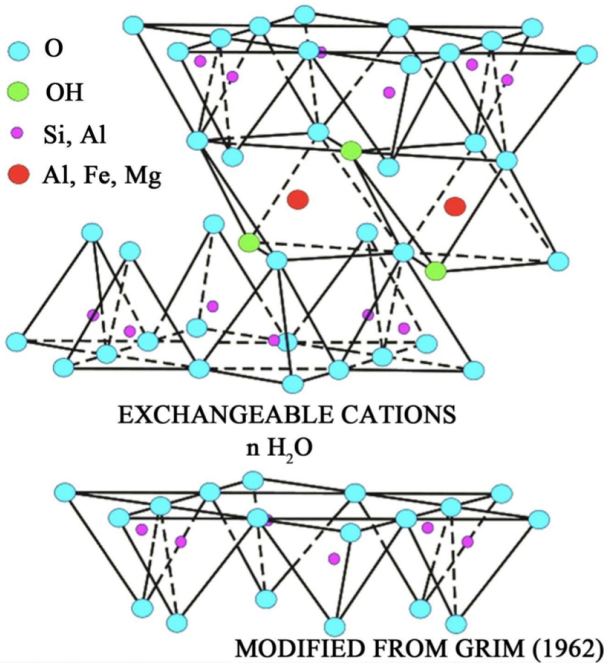

Figure 4-1: The physical chemical structure representation of Montmorillonite. Image reproduced from [76]

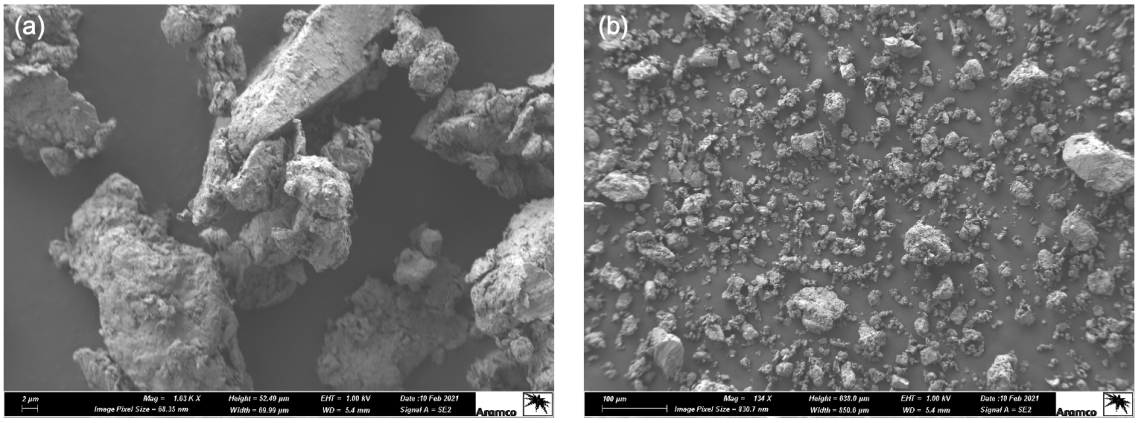

Figure 4-2: (a) SEM image of bentonite particles. The length scale shown in the left bottom corner represents the length scale for the figure which is 2 μm (b) EM image of bentonite particles with length scale as 60 μm. Image provided by A. Santra, Saudi Aramco.

300 – 500 nm and the minor axis of the platelets (small dimension) is generally in the range of 200 – 300 nm . The thickness of these plates are around 1 nm [53]. These individual platelets can be visualized from cryo TEM and SEM images of bentonite dispersions in Fig. 4-3. In aqueous dispersion, flocculation occurs and leads to the continuous formation

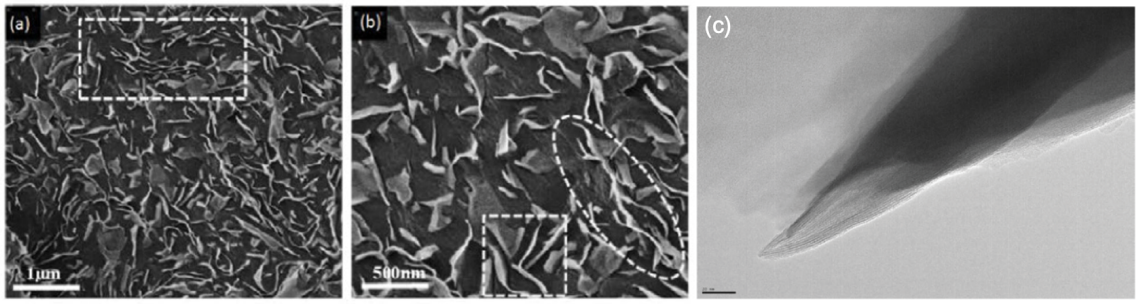

Figure 4-3: (a) and (b): Cryo SEM images of bentonite particles which show edge to face and edge to edge interactions. (c) TEM images of bentonite particles which show face to face interaction. Image reproduced from [53, 75, 101]

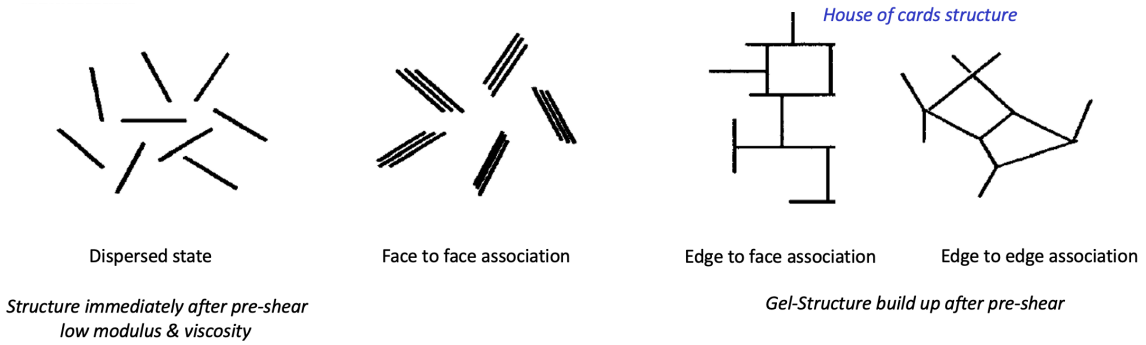

Figure 4-4: Different modes of association of the disc shaped particles in bentonite dispersion. Image reproduced from [67]

of colloidal gel structure. The gel structure slowly evolves with time as the particles under Brownian motion configure themselves to minimize the total system free energy. For plate/ disc like particles, there are three types of configurations possible: (i) Face to face association (FF) (ii) Edge to face association (EF) (iii) Edge to edge association (EE) [95]. These modes of association depend on the pH value and concentration of the dispersion. The EE and EF modes of association are predominant for small pH values (< 8.5), since the negative charges at the edges are low and for higher pH values (9.5), FF association is predominant. The FF association is the primary mode of association for higher salt concentration (Na^+) since the potential between the surfaces become attractive and for lower salt concentrations EE and EF modes of association is dominant [72, 54, 5, 67]. These different platelets configurations are shown in Fig. 4-4. The distribution of platelet modes of association influences the gel strength. When the platelets do not form any large scale

structure and are randomly oriented and distributed throughout the medium due to applied large deformations, this is referred to as the dispersed state. In this state, the elastic modulus of the material is the lowest because of the lack of structure to distribute the applied load. Aggregation is due to face to face association and since the FF configuration reduces the number of platelets or discs to form a gel structure, aggregation can result in decrease of the gel strength or elastic modulus [37]. Flocculation is best described by edge to face or edge to edge association [67]. Edge to face or edge to edge association are responsible for continuous gel-like structure. They continuously evolve with time resulting in a continuous increase of elastic modulus and a continuous slowing down of relaxation dynamics to minimize the free energy of the system [67]. This process is known as *rheological aging* and such materials which are out of thermodynamic equilibrium and show a progressive slowing down of the relaxation dynamics with time are known as soft glassy materials [50, 49, 51]. The disc shaped particles constituting the microstructure of bentonite dispersions are continuously in motion due to the thermal energy causing slow but steady structural evolution to form progressively more stable microstructures. In the process of physical aging, the elastic modulus and the relaxation time both increases progressively with time (i.e. the elastic solid-like character of this soft glassy material increases with time) [83, 84, 49, 87, 3, 39, 52]. By rejuvenating the materials (large deformations), the level of structure in the material can be reduced causing reversal of aging. In this soft glassy state, the storage modulus generally is significantly greater than loss modulus ($G' >> G''$ usually by one order of magnitude) and the storage modulus typically exhibits a weak power law dependence on frequency [2].

In this chapter, we investigate the aging behavior of bentonite dispersions by measuring a range of linear and non-linear bulk viscoelastic and rheological properties. First, we present the results and observation for creep experiments, stress relaxation experiments, frequency sweep (complex modulus response with frequency), time sweep for a specified deformation frequency (dependence of the complex modulus with time), flow curves (viscosity vs shear rate) conducted on 5 wt.% bentonite dispersion for different age times and temperatures to understand the physical aging process that take place in bentonite dispersions. Finally, we model the complex aging linear viscoelastic behavior of the bentonite

dispersions by time domain transformation techniques [14] and mechanical models at different temperatures which to help achieve a better understanding of aging dynamics and making forward predictions of bentonite's viscoelastic characteristics at an unknown time and temperature. This method of mechanical modeling of viscoelastic properties using time domain transformation can be extended to a range of material systems exhibiting soft glassy behavior.

4.2 Material preparation

The 5 wt.% bentonite dispersion in water was prepared using Wyoming bentonite. First, the bentonite powder were added to water and was mixed at 10,000 rpm for 30 minutes. The dispersion was placed in the roll mill for 1 day to ensure homogeneity . For every experiment, we followed the protocol of pre-shearing the smaple at 500 s^{-1} for 30 s in-order to have the same initial state between different experiments. The age time or the wait time t_w is considered as the time taken to start the experiment after the pre-shear and the time t is the total time elapsed after the end of preshear.

4.3 Experimental results

4.3.1 Creep experiments

Creep experiments at different applied stresses for the bentonite dispersion are performed at T = 25°C for wait time of t_W = 60 s and are shown in Fig. 4-5. Two types of critical stresses for a material can be defined using creep experiments. The first critical stress σ_{c_1} is the highest applied stress for which the shear rate is monotonously decreasing with time leading ultimately to a cessation of flow [15]. For any applied stress less than σ_{c_1}, monotonous decrease of shear rate and cessation of flow with time is observed. The value of the critical stress σ_{c_1} for 5 wt.% bentonite dispersion is σ_{c_1} = 1 Pa as indicated in Fig. 4-5. The second critical stress σ_{c_2} is defined as the smallest applied stress for which there is a monotonous increase of shear rate and asymptotic approach to a steady non-zero

shear rate, such that the material reaches steady flow at long time [15]. For any applied stress greater than σ_{c_2}, monotonous increase of shear rate leading to steady flow at long times. This second critical stress σ_{c_2} is generally considered as the yield stress of the material in the literature [15]. The σ_{c_2} for 5 wt.% bentonite dispersion is 2 Pa as seen in Fig. 4-5. For applied stress greater than σ_{c_2}, the material can be described as exhibiting

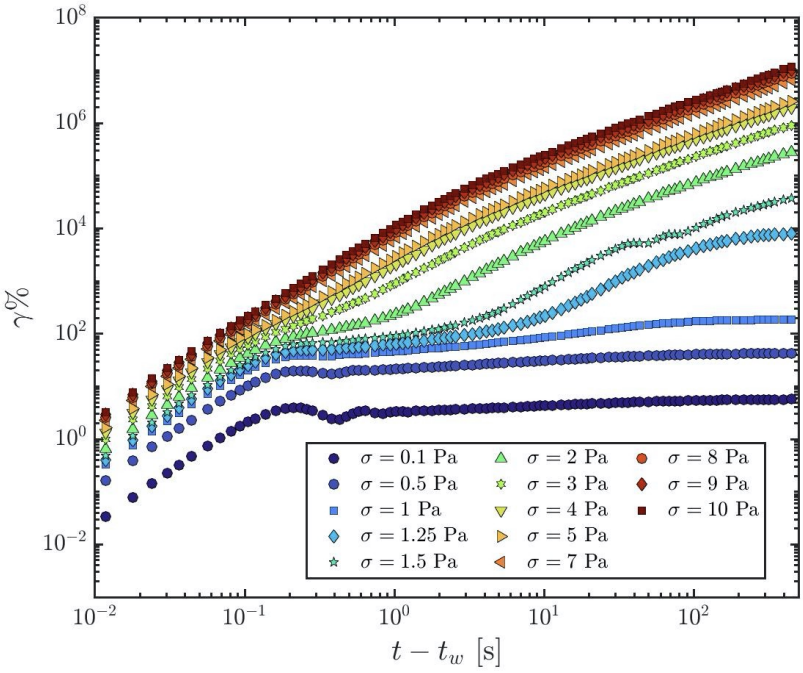

Figure 4-5: Creep experiments for various applied stress are shown. The wait time or age time t_w = 60 s. The critical stress, σ_{c_1} = 1 Pa and the second critical stress, σ_{c_2} = 2 Pa

viscoplastic liquid like behavior and for applied stress less than σ_{c_1}, the behavior of the material can be classified as solid-like behavior. Transient elastoviscoplastic response is observed between two critical stresses as shown in Fig. 4-5. The initial quadratic increase of strain at short times is due to the inertial effects from the rheometer [28]. From the same creep experiments, the apparent viscosity as a function of time for every applied stress σ_0 can be plotted by $\eta_{app}(\dot{\gamma}, t) = \sigma_0/\dot{\gamma}(t)$ as shown in Fig. 4-6. Viscosity bifurcation can be observed in Fig. 4-6 at σ_0 = 2 Pa. For higher values of applied stress greater than σ_{c_2}, steady state viscosity is reached at long times while the viscosity increases with time for applied stress smaller than σ_{c_2}. The dependence of the elastoviscoplastic response on age time or wait time for experiments is observed in Fig. 4-7 where the applied stress is 1 Pa.

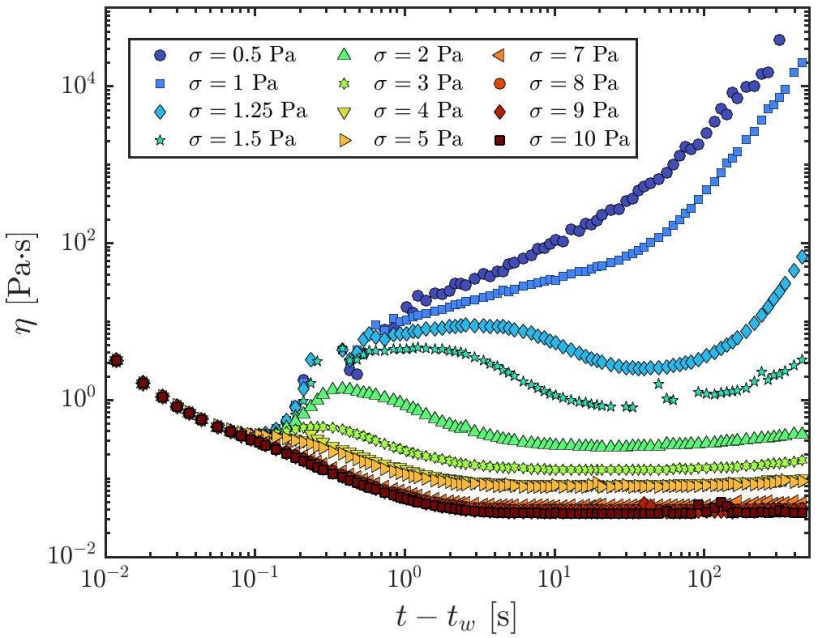

Figure 4-6: The plot of apparent viscosity η_{app} obtained from creep experiments by applying various constant shear stress is illustrated. This figure shows the viscosity bifurcation taking place at around σ_{c_2} = 2 Pa. The wait time here is t_w = 60 s.

The critical stresses, both σ_{c_1} and σ_{c_2} or the yield stress increases with age time and the dependence of creep curves with age time is illustrated in Fig. 4-7 when the applied stress is less than σ_{c_2} i.e. there is dependence on age time or wait time when the behavior of the material is elastic solid-like or the material is probed in its elastic solid-like regime. When the applied stress is greater than σ_{c_2}, i.e. when the behavior of the material is viscoplastic, there is no dependence of the rheological properties with age time. This can be observed from Fig. 4-8 where the apparent viscosity for different wait times is plotted from an applied stress of 10 Pa which is greater than σ_{c_2}. All the curves at different age times and wait times collapse with each other showing no age time dependence.

4.3.2 Flow curves at different temperatures

Flow curves for bentonite dispersion at different temperatures provide important rheological data which is used widely in the oil and gas industry as the drilling fluid undergoes different shear histories and experiences a wide range of temperatures during the drilling

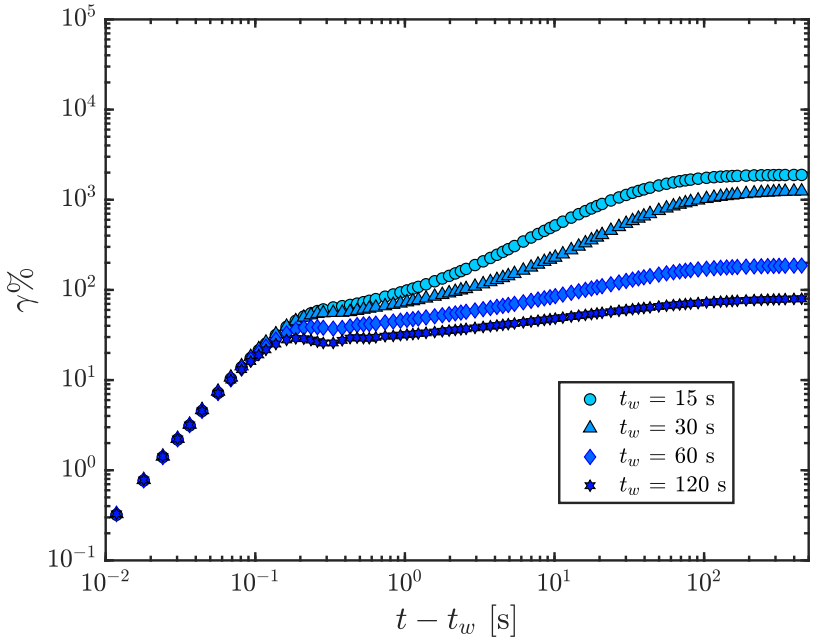

Figure 4-7: Creep experiments with applied stress of $\sigma = 1$ Pa is conducted for various wait times t_w. This figure shows the age time dependency when the applied stress is under σ_{c_2}.

process. In the oil and gas industry, the FANN 35 A rotational rheometer or viscometer [32] is used widely to obtain the flow curve. Therefore, we compare the results obtained from the more advanced lab rheometer DHR-3 (TA Instruments, New Castle DE) with the results from the industrial viscometer FANN 35 A. In the FANN 35 A, one degree of deflection in FANN 35 A corresponds to 0.511 Pa and conversion between rpm in FANN 35A and shear rate is: $\dot{\gamma} = 1.71\omega$ [32]. There are only six rpm settings available in the FANN 35 A viscometer and are tabulated as follows:

ω (rpm)	$\dot{\gamma}\ s^{-1}$
3	5.11
6	10.21
100	170.2
200	340.3
300	510.5
600	1021

Table 4.1: Conversion between rpm to shear rate in s^{-1} for FANN 35A

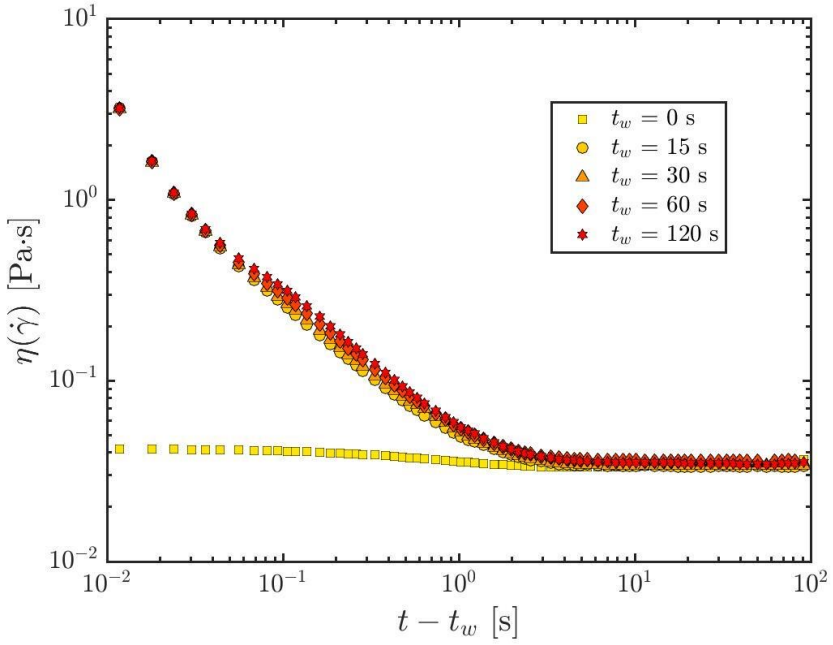

Figure 4-8: Creep experiments with applied stress of σ = 10 Pa is conducted for various wait times t_w. This figure shows the material is age time independent when the applied stress is greater than σ_{c_2}

The viscosity values determined for the six different shear rates from FANN 35A are in good agreement with the flow curve for the 5 wt.% bentonite dispersion obtained from DHR rhemoeter and are shown in Fig. 4-9. The shear thinning property of the bentonite dispersion observed in Fig. 4-9 makes bentonite highly desirable to be used as drilling fluids. Bentonite can suspend drill cuttings due to its high viscous property at low shear rates and also reduces the pumping power required because of the low viscous property at high shear rates.

The flow curve for the 5 wt. % bentonite is obtained for different different temperatures and Herschel-Bulkley model is used to obtain the yield stress from flow curve. The constitutive relationship for the Herschel-Bulkley model is represented by:

$$\sigma(\dot{\gamma}) = \sigma_y + k\dot{\gamma}^n \tag{4.1}$$

where σ_y is the yield stress and k and n are the consistency and shear thinning parameters. In Fig. 4-10 and Fig. 4-11 represent the stress vs shear rate and viscosity vs shear rate

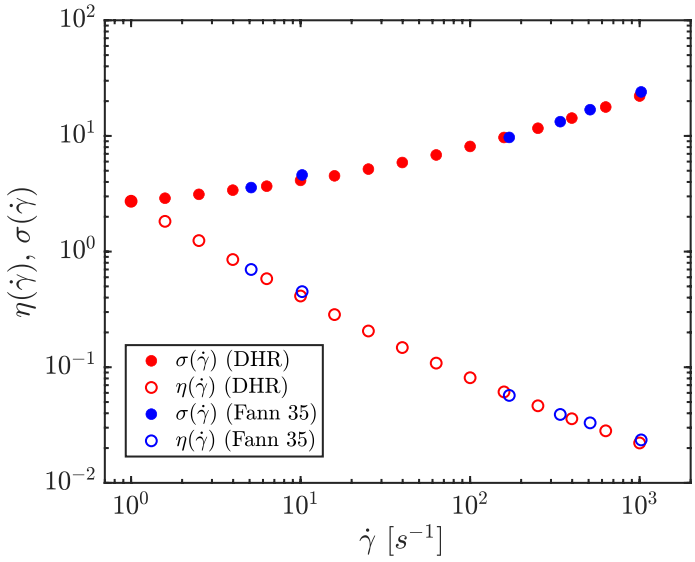

Figure 4-9: Comparison of steady shear viscosity between a FANN 35A viscometer and DHR-3 rheometer using a cone plate fixture of 60 mm diameter and 2° cone angle for 5 wt. % aqueous bentonite dispersion.

respectively for four different temperatures, T = 50°F, 77°F, 120°F and 149°F (or T = 10°C, 25 °C, 49 °C and 65 °C). In both figures, the shear rate is increased from 0.1 $^{-1}$ to 100 s^{-1} over a period of 1800 s, and data are represented by solid data points and the corresponding Herschel Bulkley fit is represented by solid lines. The shear rate is then decreased from 100 s^{-1} to 0.1 s^{-1} over a period of 1800 s from t = 2100 s to t = 3900s with 110 s for each shear rate $\dot{\gamma}$. The data points obtained in the down ramp are represented by hollow data points and the corresponding Herschel Bulkley fits are represented by dashed lines in both Fig. 4-10 and Fig. 4-11. From the Fig. 4-10, we can observe that at each temperature the yield stress of the bentonite dispersion increases with age time and also the yield stress of the bentonite dispersion increases with temperature. A strongly shear thinning property of the bentonite dispersion is observed for all temperatures. The dependence of yield stress with temperature is plotted in Fig. 4.3.4 for the data obtained from the solid Herschel Bulkley fit lines in Fig. 4-10 for the data obtained from the increasing shear rate ramp.

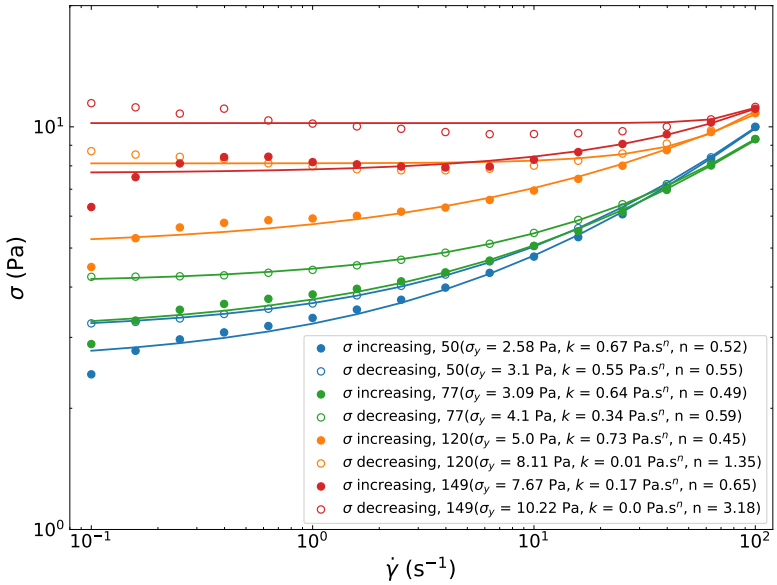

Figure 4-10: The stress vs shear rate curve usually called the flow curve is plotted for different temperatures (50°F ≤ T ≤ 149°F or equivalently T = 10°C, 25°C, 49°C, 65°C). The solid data points represent the data when shear rate is increased from $\dot{\gamma} = 0.1\ s^{-1}$ to $\dot{\gamma} = 100\ s^{-1}$ and the time evolved is from $t = 180$ s to $t = 1980$ s. The solid lines are the Herschel Bulkley fits. The hollow data points represent the data when shear rate is decreased from $\dot{\gamma} = 100\ s^{-1}$ to $\dot{\gamma} = 0.1\ s^{-1}$ and the time evolved is from $t = 2100$ s to $t = 3900$ s. The dashed lines are the corresponding Herschel Bulkley fits.

4.3.3 Dependence of complex modulus with time

We use the Gaborheometry protocol we developed in the last chapter to obtain the evolution of complex modulus with age time. The input is Small Amplitude Oscillatory Shear (SAOS) stress signal $\sigma(t) = \sigma_0 \sin(\omega t)$ where $\sigma_0 = 0.1$ Pa and the corresponding output is analysed using the Gaborheometry protocol to obtain the complex moduli evolution with time for the specified ω_0. For T = 37°C, the evolution of complex moduli with time is plotted for $\omega_0 = 0.37, 1, 3$ rad/s in Fig. 4-13. The storage modulus increases with time while the loss modulus shows no dependence with time. The oscillatory input for three different frequencies were started 20 seconds after the end of preshear and hence the wait time is $t_w = 20$ s. In order to understand if small amplitude oscillation affects the aging which takes place when there is no deformation imposed on the material, we also conducted the same SAOS experiment at different wait times for two different frequencies $\omega = 1, 5$ rad/s

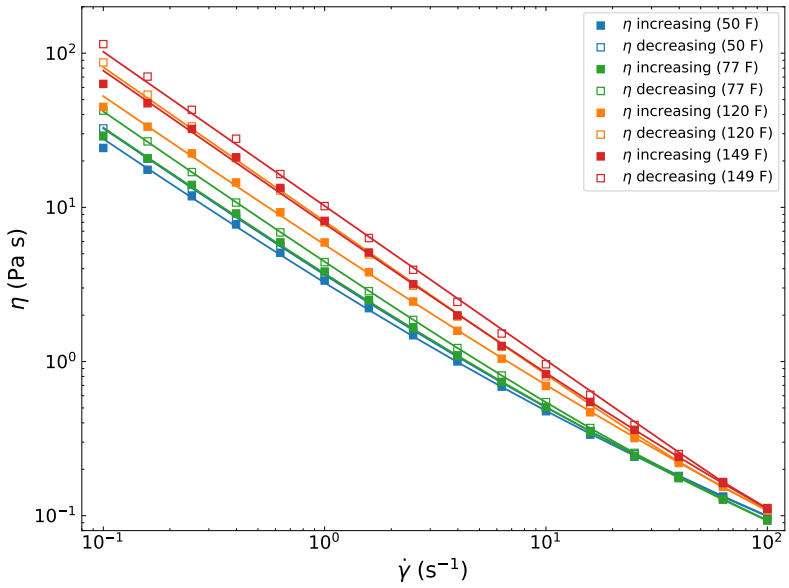

Figure 4-11: Plot of viscosity vs shear rate for different temperatures is shown (50°F ≤ T ≤ 149°F or equivalently T = 10°C, 25°C, 49°C, 65°C). The solid data points represent the data when shear rate is increased from $\dot{\gamma} = 0.1\ s^{-1}$ to $\dot{\gamma} = 100\ s^{-1}$ and the time evolved is from $t = 180$ s to $t = 1980$ s. The solid lines are the Herschel Bulkley fits. The hollow data points represent the data when shear rate is deccreased from $\dot{\gamma} = 100\ s^{-1}$ to $\dot{\gamma} = 0.1\ s^{-1}$ and the time evolved is from $t = 2100$ s to $t = 3900$ s. The dashed lines are the corresponding Herschel Bulkley fits.

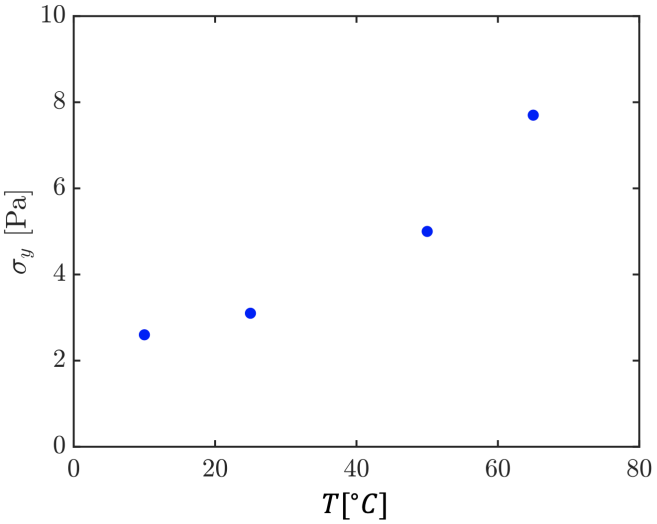

Figure 4-12: The yield stress obtained for various temperatures from the Herschel Bulkley fits (solid lines) for increasing shear rate data points (solid data points) from Fig. 4-10 is shown. The yield stress increases with temperature.

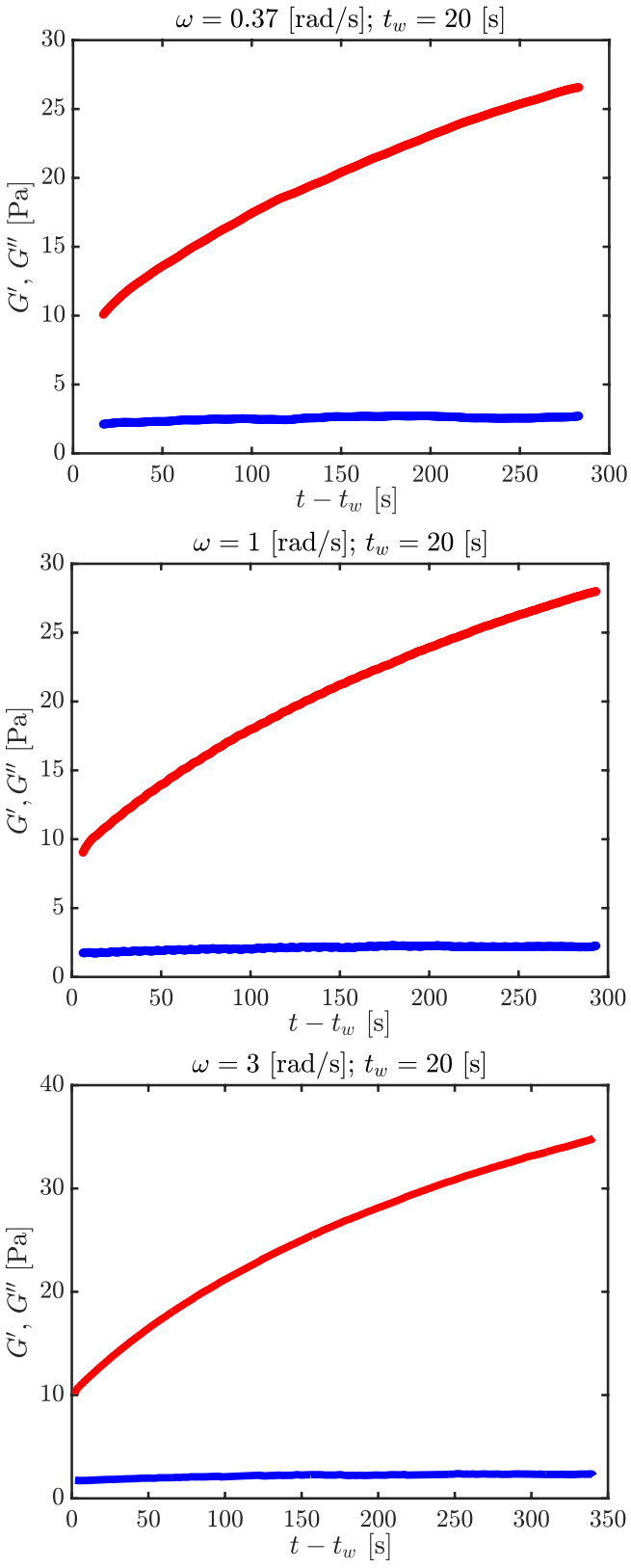

Figure 4-13: The dependence of the storage modulus and loss modulus with time for $\omega = 0.37, 1, 3$ rad/s at T = 37°C for a wait time of $t_w = 20$ s.

at T = 25°C. The results are illustrated in Fig. 4-14. The collapse of the storage moduli measured for different $t_w = 20, 50, 80$ s at both $\omega = 1, 5$ rad/s clearly demonstrates that small amplitude deformations do not result in reversal (or acceleration) of aging and therefore the complex moduli G' and G'' probed by small amplitude oscillations at any time t after the end of preshear correspond to the value of the complex moduli for the age time $t_w = t$. Note that age time equals elapsed time after pre-shear only for small oscillatory deformations and not for step strain experiments or large oscillatory deformations.

4.3.4 Frequency response of Bentonite at different wait times

The bentonite dispersion continuously ages and therefore it is not feasible to conduct conventional frequency sweep experiments in order to obtain the complex modulus ($G^*(\omega)$) of the material. Therefore we use Optimally Windowed Chirps in order to obtain snapshots of the frequency response at different age times [35, 36]. As we observed in Fig. 4-14, imposing small deformations does not affect the rate of aging and therefore we send a series of chirp signals each of duration T to obtain the frequency response at different age times. The input stress signal is given by

$$\sigma(t) = \sigma_0 \begin{cases} \cos^2[\frac{\pi}{r}(\frac{t}{T} - \frac{r}{2})] \sin\left[\frac{\omega_1 T}{\log(\omega_2/\omega_1)}[\exp(\log(\omega_2/\omega_1)\frac{t}{T}) - 1]\right] & \frac{t}{T} \leq \frac{r}{2} \\ \sin\left[\frac{\omega_1 T}{\log(\omega_2/\omega_1)}[\exp(\log(\omega_2/\omega_1)\frac{t}{T}) - 1]\right] & \frac{r}{2} < \frac{t}{T} < 1 - \frac{r}{2} \\ \cos^2[\frac{\pi}{r}(\frac{t}{T} - 1 + \frac{r}{2})] \sin\left[\frac{\omega_1 T}{\log(\omega_2/\omega_1)}[\exp(\log(\omega_2/\omega_1)\frac{t}{T}) - 1]\right] & \frac{t}{T} \geq 1 - \frac{r}{2} \end{cases} \tag{4.2}$$

where $T = 14$ s, $\omega_1 = 0.3$ rad/s, $\omega_1 = 5$ rad/s, $r = 0.1$ and $\sigma_0 = 0.1$ Pa. Chirp signals of duration 14 s are continuously sent to the material one after another for 300 s to obtain the frequency response of the bentonite dispersion at various age times. The age time of the material is taken to be the time at the start of the chirp signal. The storage and loss modulus as a function of frequency for different age times for temperatures T = 10°C and T = 25°C are presented in Fig. 4-15. Similarly, the frequency response at various age times for temperatures T = 10°C and T = 25°C is shown in Fig. 4-16. The storage modulus increases with age time and for a fixed age time, the storage modulus has a weak powerlaw

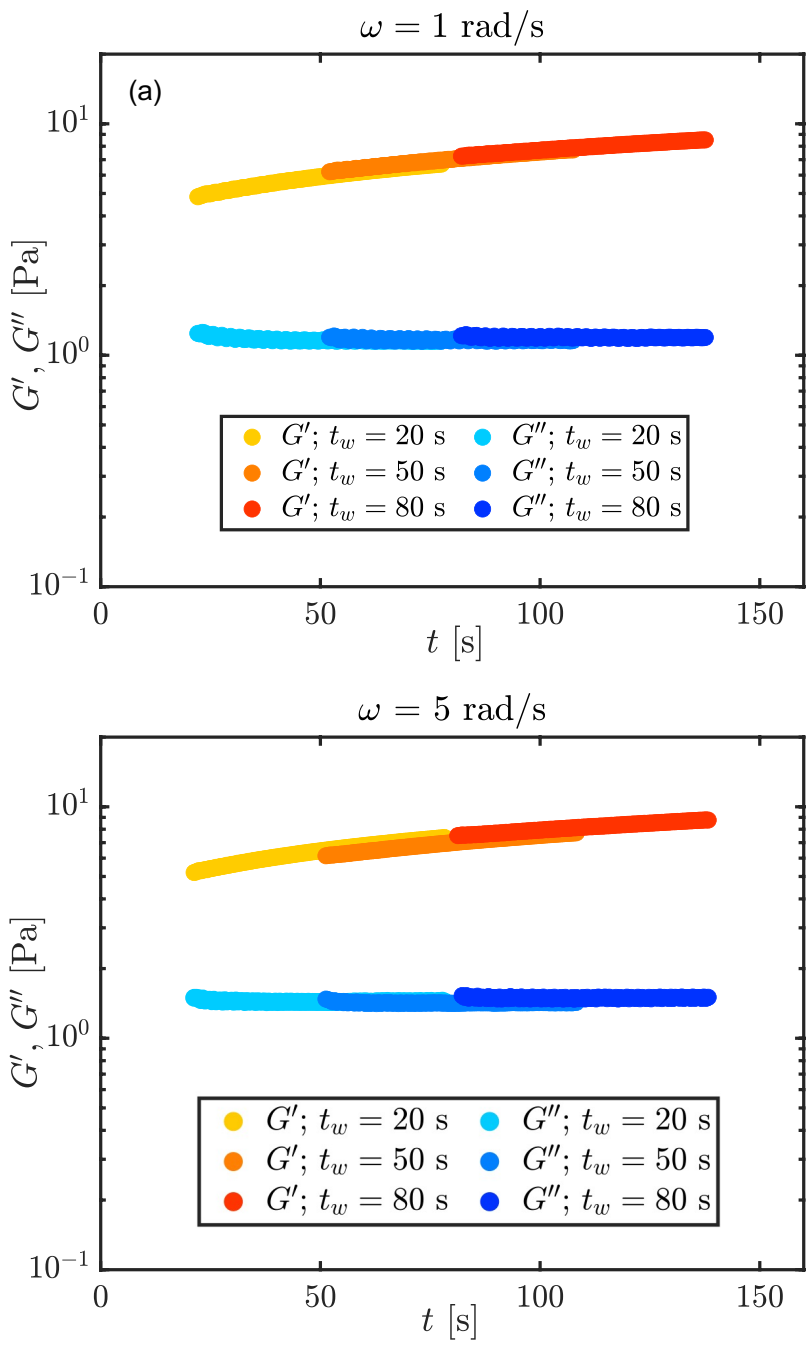

Figure 4-14: Imposing small amplitude deformations does not affect the rate of material aging. This is shown by illustrating the collapse of evolution of the complex moduli with time for different wait times for frequencies of 1 and 5 rad/s at T = 25°C.

dependence with frequency indicating soft glassy rheological characteristics. The storage modulus also increases with temperature as seen in Fig. 4-15 and Fig. 4-16. This can be attributed to the increase in the thermal energy density within the aging soft glass which

accelerates the systems exploration of more stable microstructural configurations resulting in a monotonic increase in the elastic or storage modulus. In Fig. 4-15 and Fig. 4-16, the storage modulus is represented by the red colored data points with intensity increasing as the age time increases. The blue data points represent the loss modulus and again the color intensity increases as the age time increases.

4.3.5 Stress relaxation for different temperatures

Stress relaxation experiments following imposition of a step strain help us understand the relaxation dynamics of a material and explore the relaxation spectrum of a material [87]. To understand the dependence of relaxation dynamics with age time and temperature, we use step strain experiments performed in a DHR-3 rheometer. The age time t_w for a stress relaxation experiment is considered as the time t (time elasped after preshear) at which the step strain is imposed ($t_w = t$ at the time of imposition of step strain). This is due to the fact that it is the microstructure existing at the time of application i.e. ($t = t_w$) of the applied strain that carries the imposed load. As time progresses, there is a continuous evolution of the microstructure of the material, but the newly formed microstructures at times t after the instantaneous application of the step strain do not contribute to sharing the applied load. Fig. 4-17 shows the measured relaxation modulus ($G(t - t_w, t_w)$) for T = 10°C and T = 25°C. The step strain amplitude imposed is $\gamma_0 = 2\%$. To select the imposed strain amplitude γ_0, we conduct step strain experiments for a range of strain amplitudes systematically and choose γ_0 such that the relaxation modulus G is independent of the imposed strain amplitude (linear regime). The relaxation modulus increases as the age time or the wait time increases because of aging. In Fig. 4-17 (a), one can also observe the increase of characteristic relaxation time with age time from noticing visually the decrease of decay rate of relaxation modulus with age time. This indicates the slow down of the relaxation dynamics with age time.

Similarly, the relaxation modulus for T = 37°C and T = 49°C are illustrated in 4-18. From Fig. 4-17 and Fig. 4-18, we can also note the increase of relaxation modulus with temperauture due to the increase of thermal energy density in the material which aids in a

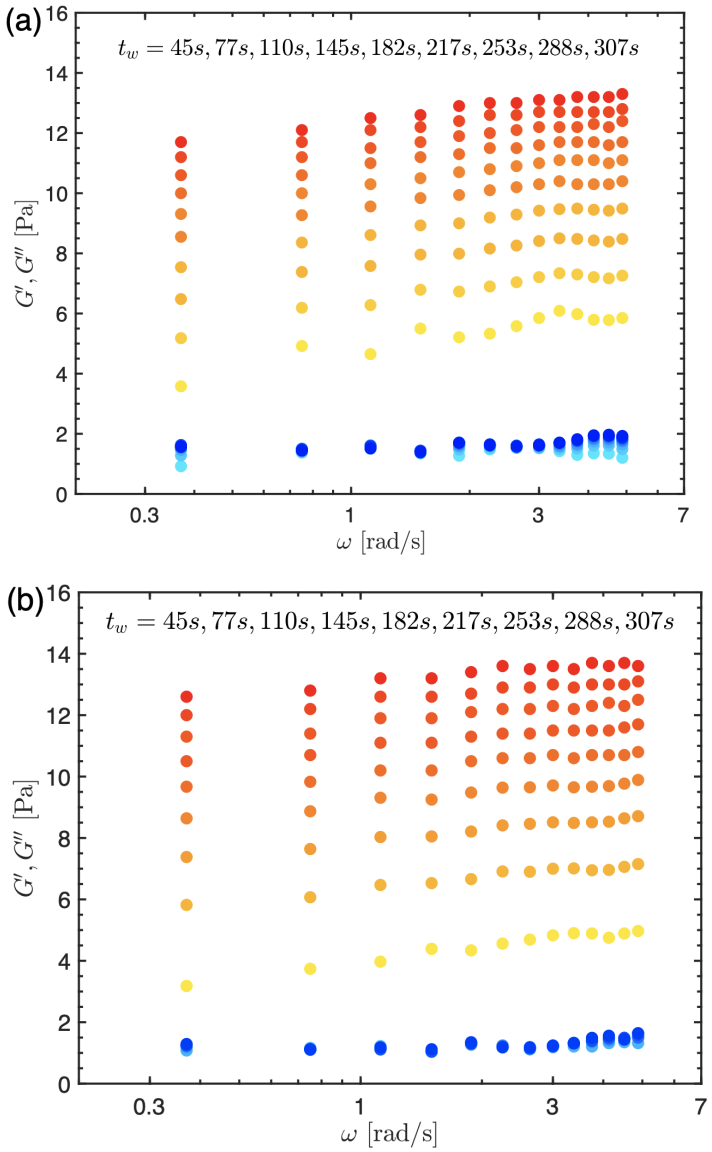

Figure 4-15: (a) Red shaded filled points represent the evolution in the storage modulus as a function of frequency for different wait or age times for T = 10°C. Blue shaded filled symbols represent loss modulus as a function of frequency for different wait or age times at T = 10°C. Both the red and blue color intensity increases with age time t_w. (b) same information as (a) but at T = 25°C.

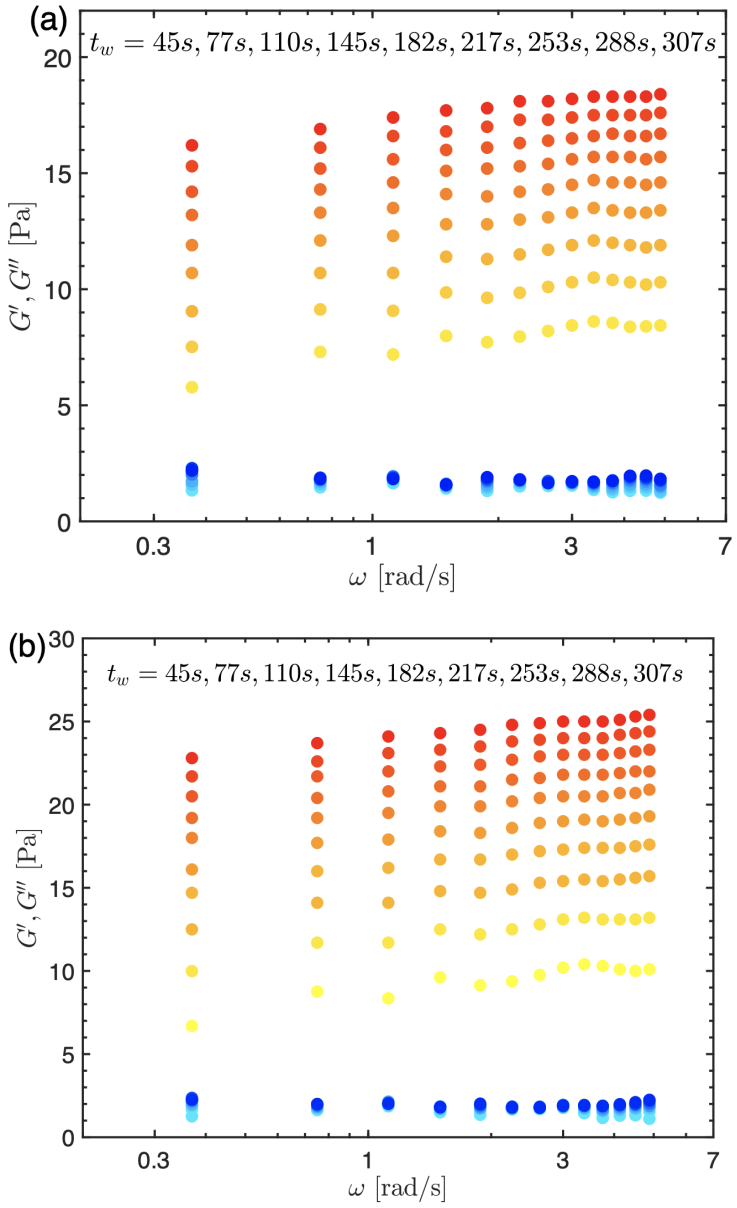

Figure 4-16: (a) Red shaded filled points represent storage modulus as a function of frequency for different wait or age times for T = 37°C. Blue shaded filled symbols represent loss modulus as a function of frequency for different wait or age times for T = 37°C. Both the red and blue color intensity increases with age time t_w. (b) same information as (a) but at T = 49°C.

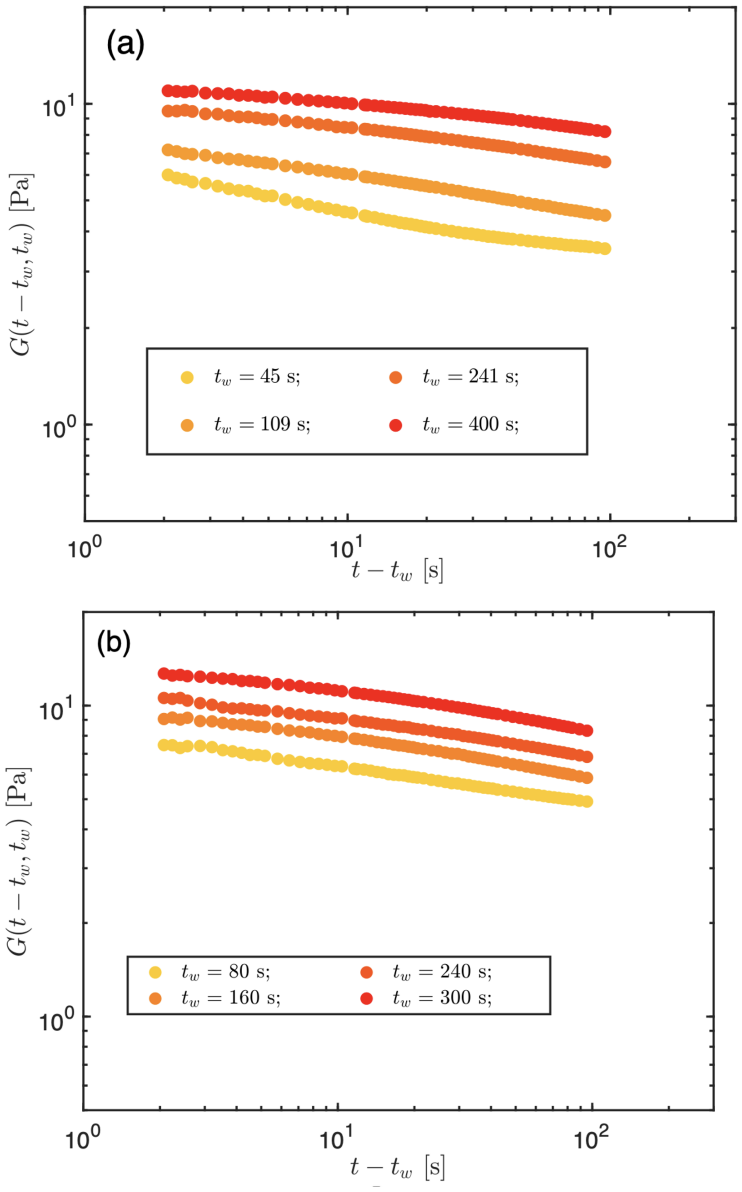

Figure 4-17: (a) Relaxation modulus for different wait or age times at T = 10°C. (b) Relaxation modulus for different wait or age times at T = 25°C. The step strain amplitude imposed for both (a) and (b) is γ_0 = 0.02.

faster rate of evolution of gel structure as it attempts to minimize the total free energy of the bentonite system.

4.3.6 LAOStress for bentonite

Large Amplitude Oscillatory Stress (LAOStress) experiments are often used to characterize the nopnlinear material behavior to large deformations [25, 29]. They can be also be used to find the dynamic yielding behavior of yielding materials [21]. The Lissajous curves for a range of input amplitudes can often visually indicate the different linear and non-linear regimes such as small, medium and large amplitude regimes. The Lissajous curves for different input stress amplitude and deformation frequency for an age time of t_w. = 300 s (we wait for time of 300 s after pre-shear with no loading $\sigma_0 = 0$ and then impose $\sigma = \sigma_0 \sin \omega(t - t_w)$) is shown in Fig. 4-19. For high frequencies, the moment of inertia of the rheometer geometry used can affect the measurement. To quantify such effects, Dimitrou et al. defined a non-dimensionless parameter known as Inertia number In [21]. The inertia number for a conical plate fixture (with radius R and angle θ_0) is defined as follows:

$$In = \frac{3I\omega^2\theta_0\gamma_0}{2\pi\sigma_0 R^3} \tag{4.3}$$

where I is the geometry moment of inertia and γ_0 is the amplitude of the strain response for imposed sinusoidal stress with amplitdue σ_0. In order to get accurate measurements it is important for the inertia number (In) to satisfy the criteria: $In < 0.05$. The light gray shaded Lissajous curves in Fig. 4-19 indicate the Inertia number is close to the criterion $In \approx 0.05$ and for the dark gray shaded Lissajous curves In exceeds 0.05 and the results are dominated by inertia and hence do not provide meaningful information without careful correction of inertial effects.

To extract information about yielding from these Lisssajous curves, we use the area criterion [21] for yielding which is defined as follows:

$$\phi = \frac{E_d}{(E_d)_{pp}} \tag{4.4}$$

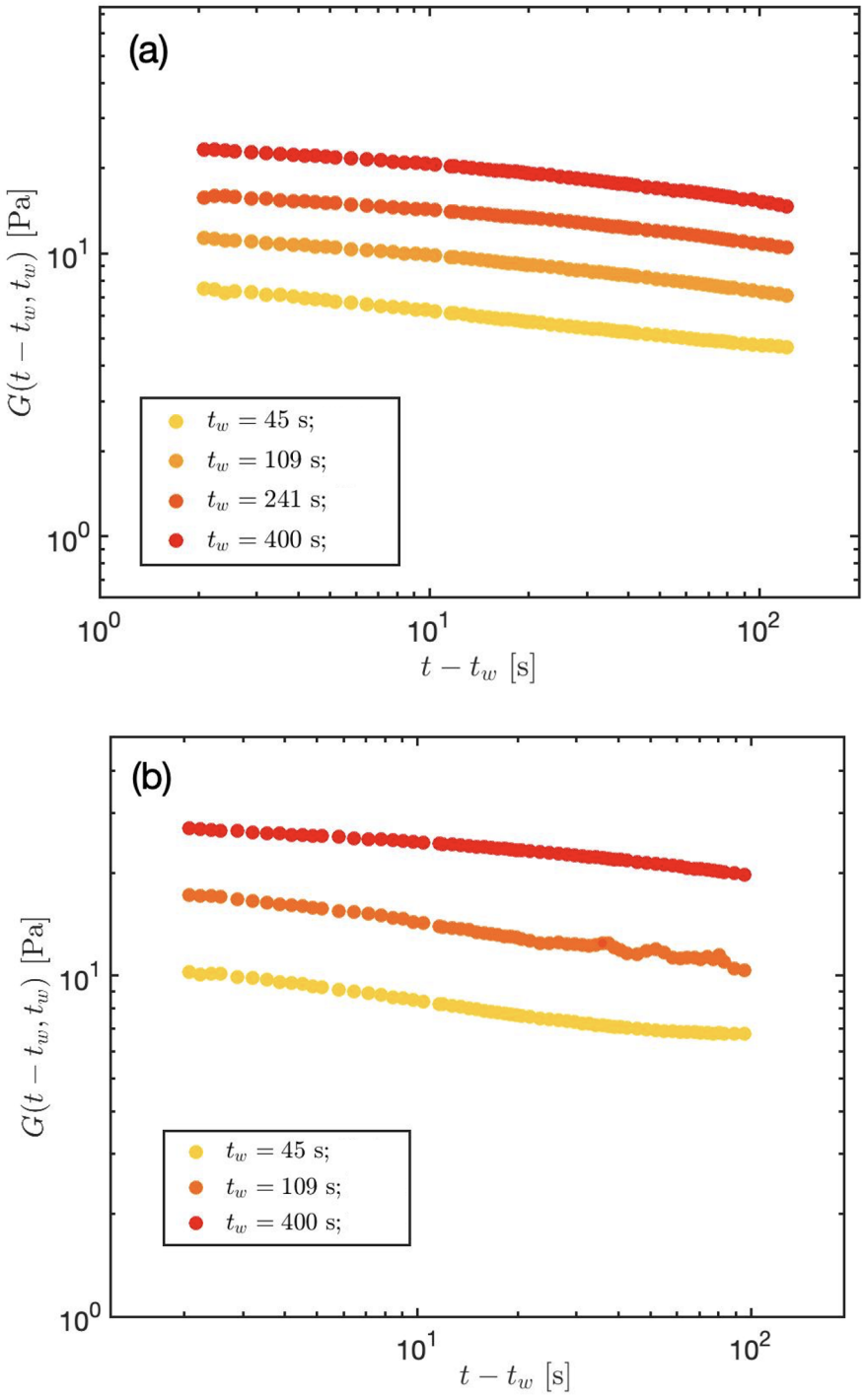

Figure 4-18: (a) Relaxation modulus for different wait or age times at T = 37°C. (b) Relaxation modulus for different wait or age times at T = 49°C. The step strain amplitude imposed for both (a) and (b) is γ_0 = 0.02.

where E_d is the energy dissipated in one cycle and $(E_d)_{pp}$ is the perfectly dissipated plastic energy.

$$E_d = \oint \sigma d\gamma \tag{4.5}$$

$$(E_d)_{pp} = (\sigma_{max} - \sigma_{min})(\gamma_{max} - \gamma_{min}) \tag{4.6}$$

The area criteria ϕ for perfect plastic, Newtonian and purely elastic material behavior are

$$\phi = \begin{cases} 1 & \rightarrow Plastic \\ \pi/4 = 0.785 & \rightarrow Newtonian \\ 0 & \rightarrow Elastic \end{cases} \tag{4.7}$$

The area criterion for yielding ϕ is illustrated for every Lissajous curve across frequency and input stress amplitude in Fig. 4-20. For low input stress amplitudes $\sigma \ll \sigma_y$ (yield stress), the responses are linear viscoelastic (and elliptical) and $\phi \rightarrow 0$ indicating linear viscoelastic solid response. This is the regime under which stress relaxation experiments were performed in section 4.3.5. It can be observed from the figure that the yielding is a function of frequency and for a fixed input stress amplitude, ϕ increases with frequency suggesting that yield stress decreases with the deformation frequency. The bentonite dispersion also acts most like a viscoplastic solid for large stresses and low frequencies (Top left of Pipkin diagram) and $In > 0.05$ affects the high frequency ($\omega = 3, 10$ rad/s) with large stress amplitude $\sigma_0 = 6$ Pa response.

4.4 Linear rheological modeling of bentonite

4.4.1 Equations in material time domain

We seek to develop a constitutive model based on the data obtained from chirp experiments and stress relaxation experiments reported in section 3.3.5 and 3.3.6 to enable prediction of the rheological aging of bentonite over a range of time scales and temperatures. A schematic diagram of the data considered for modeling the aging bentonite dispersion is visualized in Fig. 4-21. After cessation of pre-shearing, at $t = 0$, the chirp and step strain

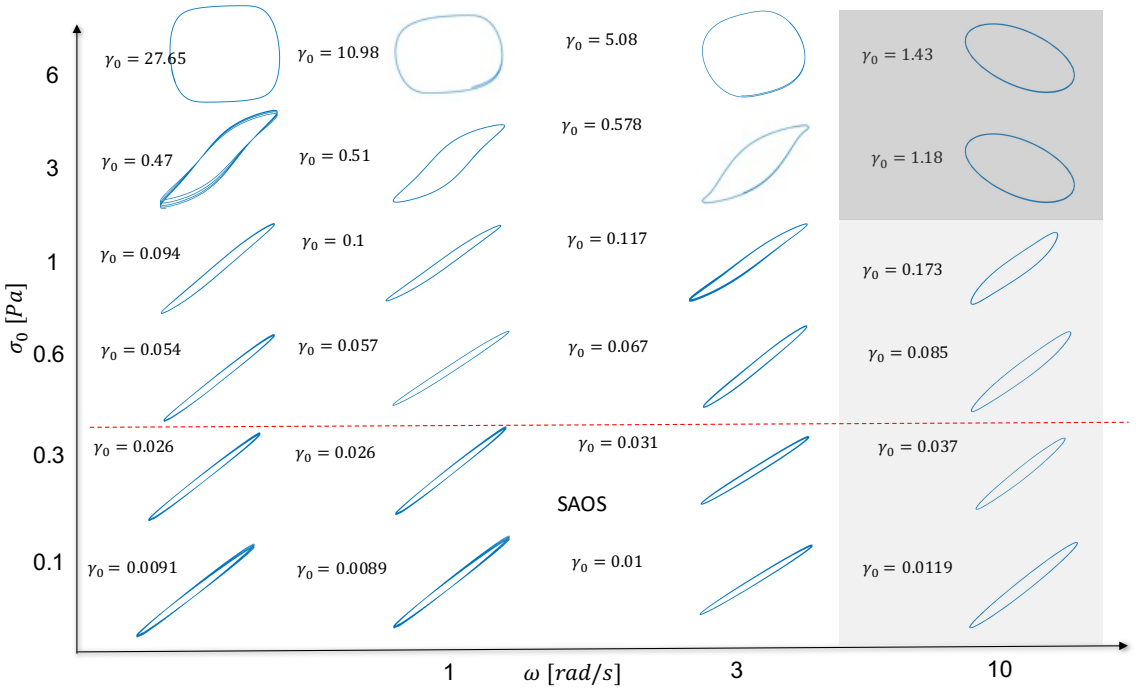

Figure 4-19: Lissajous curves for various input stress amplitude and deformation frequency at T = 25°C. The output strain amplitude increases with frequency for a given input stress amplitude.

experiments are conducted at a series of age times $t_{w(i)}$. The elastic modulus increases with age time and the characteristic relaxation time increases as well because of the progressive slow down of the relaxation dynamics with age time as seen in Fig. 4-17. The area under the relaxation modulus is the zero shear viscosity and as illustrated qualitatively in the Fig. 4-21, the viscosity of the bentonite gel increases with age time. In chirp experiments, the storage moduli increases with age time. Storage moduli shows weak powerlaw dependence with frequency and the power-law coefficient decreases with age time as well.

As a result of this progressive aging, it has been shown that for such aging systems the Boltzmann superposition principle does not hold [14, 49]. For non-ergodic systems in which the relaxation modulus is age-time dependent, the stress must be written in the form [33]:

$$\sigma(t) = \int_{-\infty}^{t} G(t - t', t')\dot{\gamma}(t')dt' \tag{4.8}$$

Joshi and coworkers have shown this aging effect can be understood as a change in the material's relaxation time scale, τ with the age time. we define a material or effective time

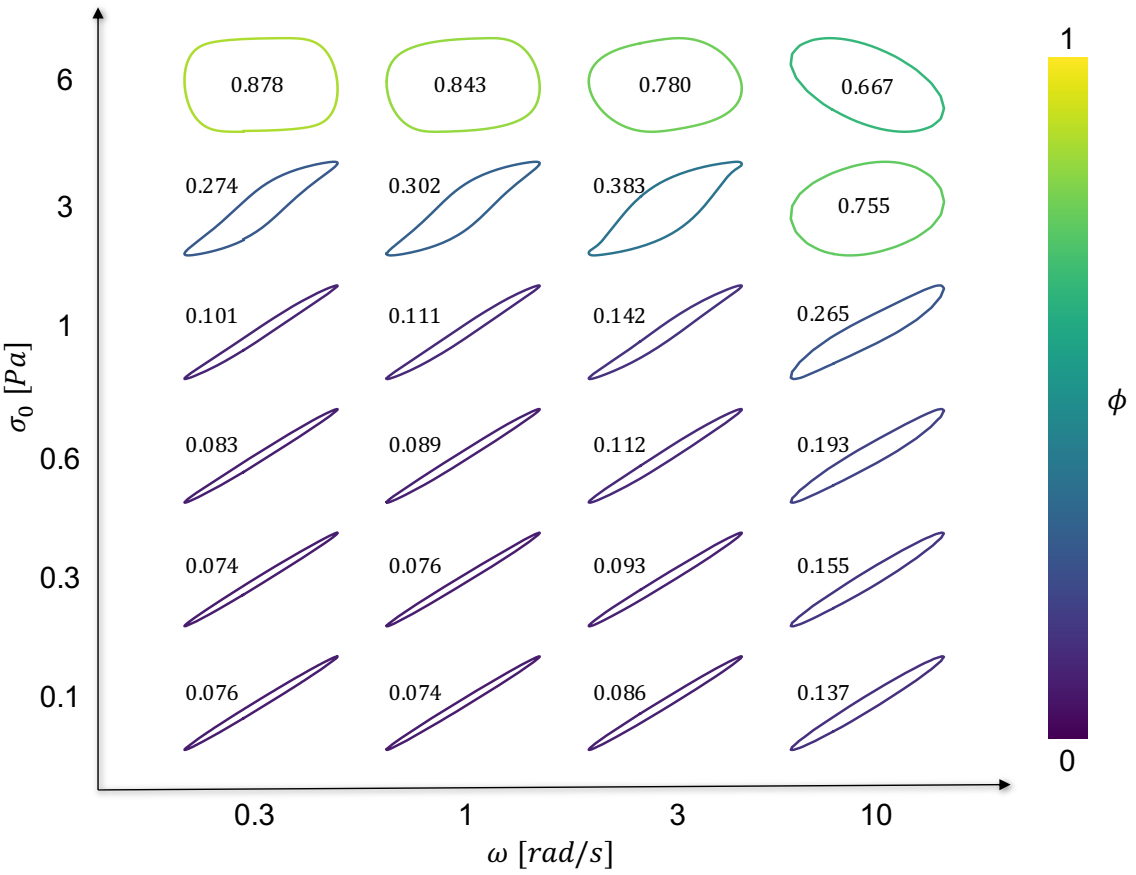

Figure 4-20: Area criterion for yielding ϕ for Lissajous curves for various input stress amplitude and deformation frequency. The area criterion ϕ increases with frequency for a given input stress amplitude. The Lissajous curves for input stress of amplitude σ_0 = 6 Pa, angular frequency ω = 3 rad/s and ω = 10 rad/s are dominated by inertial effects and hence do not provide meaningful information (the two top right curves).

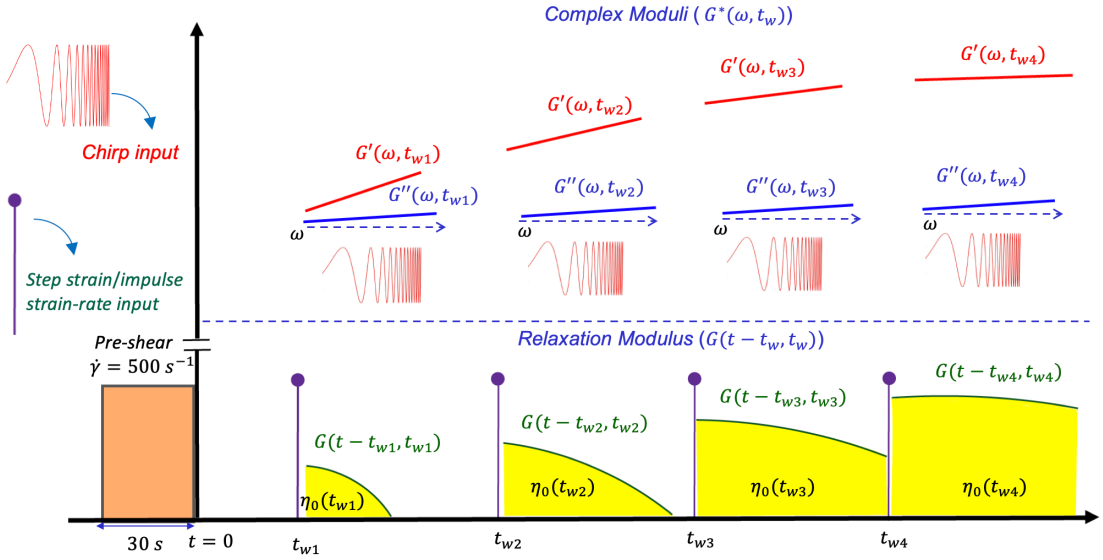

Figure 4-21: The experiments considered for modeling are represented schematically. After preshear, at different wait times step strain experiments and chirp experiments are conducted to obtain relaxation modulus and frequency response respectively. Due to aging, the modulus increases and the relaxation dynamics slow down with wait time. This phenomena can be observed in both the relaxation modulus and frequency response. This also leads to the increase of viscosity with age time.

ξ elapsed between laboratory time t and t_w in terms of the age time dependent relaxation time of the material as [14]:

$$\xi(t) - \xi(t_w) = \tau_0(t_R) \int_{t_w}^{t} \frac{dt'}{\tau(t')} \tag{4.9}$$

where t_w is the aging time or the wait time and $\tau_0(t_R)$ is a reference relaxation time at an arbitrarily chosen reference time t_R. A common model for describing evolution of the material relaxation time $\tau(t')$ is a power law with exponent μ [50, 49, 85, 83, 86, 84, 87]. Therefore, for a fixed temperature $\tau(t')$ can be written as:

$$\tau(t') = \tau_m \left(\frac{t'}{\tau_m} \right)^{\mu} \tag{4.10}$$

and τ_0 which is the relaxation time at t_R can thus be written as:

$$\tau_0 = \tau_m \left(\frac{t_R}{\tau_m} \right)^{\mu} \tag{4.11}$$

Here, t_R is again an arbitrary reference time of our choice. When $\mu = 0$, there is no aging taking place and the limits where $\mu > 1$ and $\mu < 1$ are called hyperaging and subaging respectively [2]. Details on signatures of hyperaging for soft glassy materials are presented in Appendix C. Simple aging is a special case where $\mu = 1$ [33]. Now, considering the time

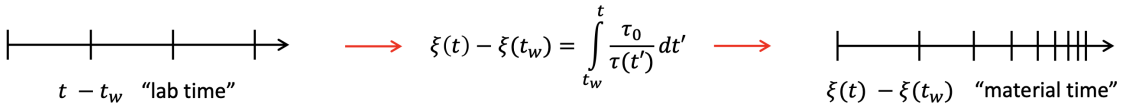

Figure 4-22: Lab time to material time domain to account for the changing relaxation dynamics with age time.

elapsed in material time domain, the output stress can be written in terms of the Boltzmann integral (discussed in chapter 1.3.1) with the effective relaxation modulus $\tilde{G}$ in the effective or material time domain [2, 49, 83]:

$$\sigma(\xi) = \int_{-\infty}^{\xi(t)} \tilde{G}(\xi - \xi') \frac{d\gamma}{d\xi'} d\xi' \tag{4.12}$$

where the elapsed time in the material domain can be written by combining Eq.(4.10) and

Eq.(4.11) in Eq.(4.9) as:

$$\tilde{t} = \xi(t) - \xi(t_w) = t_R^{\mu} \frac{t_w^{1-\mu} - t^{1-\mu}}{\mu - 1} \tag{4.13}$$

Following Shukla et al. in [87], the relaxation modulus in laboratory time $G(t - t_w, t_w)$ may be converted to the effective relaxation modulus $\tilde{G}$ in material time by scaling the relaxation modulus G in terms of material time and multiplying with a vertical shift factor $b(t_w)$:

$$\tilde{G}\left(\xi(t) - \xi(t_w)\right) = b(t_w) G\left(\xi(t) - \xi(t_w), t_w\right) \tag{4.14}$$

The vertical shift factor $b(t_w)$ shifts the time-dilated curves to a single master curve on the $\tilde{t} = \xi(t) - \xi(t_w)$ axis. To obtain the effective complex modulus $\tilde{G}^*$ in the effective frequency domain $\tilde{\omega}$, we use the interconversion formula between relaxation modulus and complex modulus defined in chapter 1.3.1 Eq. (1.19) but in terms of material domain variables $\tilde{t}, \tilde{\omega}$:

$$\tilde{G}^*(\tilde{\omega}) = i\tilde{\omega} \int_0^{\infty} \tilde{G}(\tilde{t}) e^{i\tilde{\omega}\tilde{t}} d\tilde{t} \tag{4.15}$$

Substituting Eq. (4.14) in Eq. (4.15), and using Eq. (1.19), we obtain

$$\tilde{G}^*(\tilde{\omega}) = b(t_w) G^*\left(\omega \left(\frac{t_w}{t_R}\right)^{\mu}, t_w\right) \tag{4.16}$$

Here we may also write the effective frequency $\tilde{\omega}$ in material domain in terms of laboratory frequency variable ω as:

$$\tilde{\omega} = \omega \left(\frac{\tau_m}{\tau_0}\right)^{\mu} = \omega \left(\frac{t_w}{t_R}\right)^{\mu} \tag{4.17}$$

This is a general framework for time-age time superposition. But, to fit the data of linear viscoelastic properties of bentonite, we need a mechanical model for $\tilde{G}^*(\tilde{\omega})$ or equivalently $\tilde{G}(\tilde{t})$.

4.4.2 Bentonite as a fractional Maxwell gel in material time domain

We propose to model the linear viscoelastic properties of bentonite in the material time domain by an aging fractional Maxwell gel model (FMG) in parallel with a non-aging viscous mode as illustrated in Fig. 4-23. The constitutive equation for the aging fractional

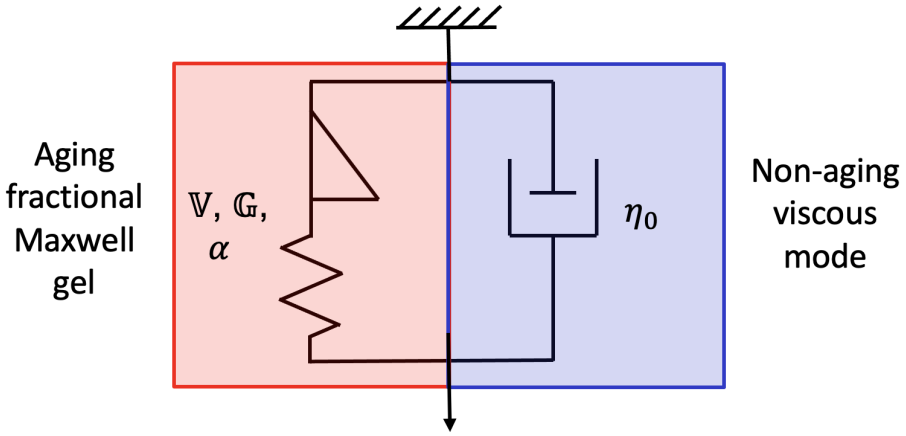

Figure 4-23: Proposed mechanical model for modeling aging linear viscoelastic response of 5 wt. % bentonite dispersion. The parameters of this model are $\mathbb{V}$, $\mathbb{G}$, α from aging FMG and η_0 from non-aging viscous mode.

Maxwell gel [55] in the material time domain can be written as

$$\tilde{\sigma}(\tilde{t}) + \frac{\mathbb{V}}{\mathbb{G}} \frac{d^{\alpha}\tilde{\sigma}(\tilde{t})}{d\tilde{t}^{\alpha}} = \mathbb{V} \frac{d^{\alpha}\gamma}{d\tilde{t}^{\alpha}} \tag{4.18}$$

where $\tilde{\sigma}$ is the stress in material time domain and $\mathbb{V}$, $\mathbb{G}$ and α are the FMG parameters. The the contribution to the total stress for the non-aging viscous mode is given by:

$$\sigma_v(t) = \eta_0 \dot{\gamma}(t) \tag{4.19}$$

where σ_v is the stress in the real time domain. Therefore, in the real time domain, the total stress can be written using Eq. (4.9), Eq. (4.12) and (4.14) as follows:

$$\sigma(t - t_w, t_w) = \tilde{\sigma}(\tilde{t})/b(t_w) + \sigma_v(t - t_w) \tag{4.20}$$

where $\tilde{t}$ is given by Eq. (4.9). Therefore to model the viscoelastic response of the bentonite dispersion in material time domain using the FMG model, the non-aging viscous mode should be first subtracted from the total real time response. The relaxation modulus in real time or lab time obtained Eq. above in material domain and changing variable can be

written as follows:

$$G(t - t_w, t_w) = \frac{1}{b(t_w)} \mathbb{G} E_{\alpha,1}\left(- \frac{\mathbb{G}}{\mathbb{V}} \tilde{t}^{\alpha} \right) \tag{4.21}$$

where $\tilde{t} = t_R^{\mu} \frac{t_w^{1-\mu} - t^{1-\mu}}{\mu - 1}$ is the dilated time in the material time domain. Similarly, the frequency dependent complex moduli in the laboratory time domain can be written as

$$G^*(\omega, t_w) = \frac{1}{b(t_w)} \frac{\mathbb{V}(i\tilde{\omega})^{\alpha}}{1 + \frac{\mathbb{V}}{\mathbb{G}}(i\tilde{\omega})^{\alpha}} + i\eta_0\omega \tag{4.22}$$

where $\tilde{\omega} = \omega \left(\frac{t_w}{t_R} \right)^{\mu}$. Based on our observation in superposing the time dilated relaxation modulus $G(\tilde{t}, t_w)$ to a master curve $\tilde{G}(\tilde{t}$ using vertical shift factors $b(t_w)$ for the data we obtained, we assume:

$$b(t_w) = \left(\frac{t_w}{t_R} \right)^n \tag{4.23}$$

Therefore, the linear viscoelastic model for bentonite dispersion is a six parameter model. Three parameters $\mathbb{V}, \mathbb{G}, \alpha$ parameterize the aging FMG model. The aging exponent μ describes the dilation of time in conversion of lab time to effective material time Eq.(4.13) or the real frequency to the effective frequency Eq.(4.17). The vertical shift factor $b(t_w)$ introduces the parameter n. The parameter η_0 is the viscosity of the non-aging viscous mode. The algorithm to calculate the 6 parameters for the bentonite dispersion is illustrated in Fig. 4-24

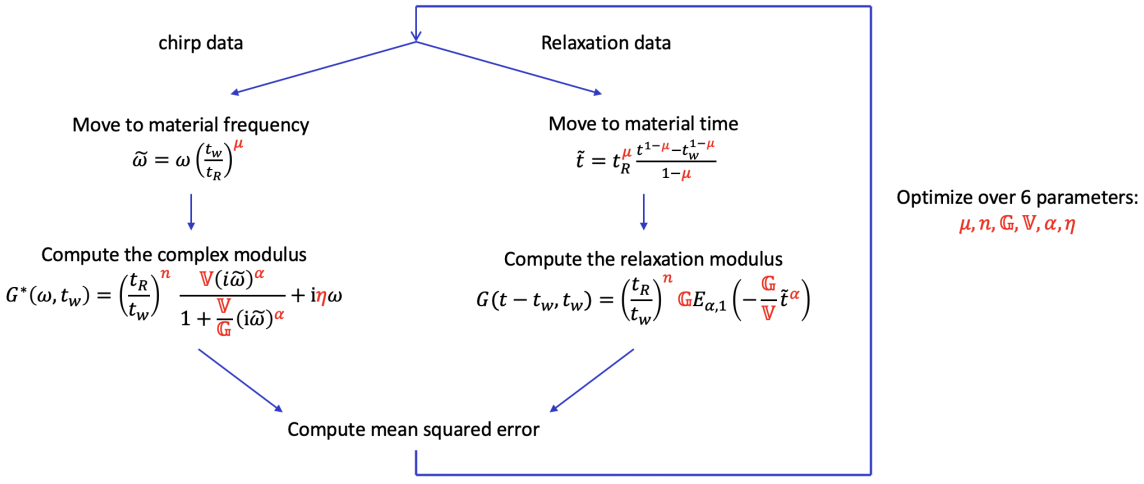

Figure 4-24: Algorithm to obtain the six parameters $\mathbb{V}, \mathbb{G}, \alpha, n, \eta_0, \mu$ for modeling the linear viscoelastic response of 5 wt.% bentonite dispersion.

4.4.3 Results from the model

The results of the model for the data from chirp and stress relaxation experiments are presented in this section. The model fits for the experiments conducted at $T = 10°C$ are presented in Fig. 4-25. The six parameters used to fit the data points are $\mathbb{G} = 19.1$ Pa; $\mathbb{V} = 29.9$ Pa·s$^{\alpha}$; $\alpha = 0.19$; $n = 0.21$; $\mu = 1.62$; $\eta_0 = 0.15$ Pa·s which are obtained by global optimization following the algorithm illustrated in Fig. 4-24. The constrained optimization is carried out by using a matlab defined function 'fmincon' which uses interior point method to minimize the Loss function.

We subtract the non-aging viscous response from the complex moduli data obtained in real time and then use the obtained value of μ to shift the stress relaxation data points from real time to material time domain using Eq. (4.13) and the data points in chirp experiments from real frequency domain to effective or material frequency domain using Eq. (4.17). After shifting the data points to the material time and frequency domain, employing the obtained value of n which enables us to calculate the vertical shift factor $b(t_w)$, we use Eq. (4.14) and Eq. (4.16) to vertically shift the relaxation modulus and complex moduli respectively to superpose on each other. With these transformations, the data collapse perfectly into a master curve as illustrated in Fig. 4-26 for $\mu = 1.6$ and the arbitrary reference time chosen is $t_R = 300$ s.. The solid lines are the FMG fits to the mastercurve using the obtained parameters $\mathbb{G}, \mathbb{V}, \alpha$.

To model the data from chirps and stress relaxation experiments for other temperatures, the FMG fractional exponent is constrained to be $\alpha = 0.19$ which allows us to perform Temperature superposition of the data for various temperatures. More discussion on temperature superposition is discussed in section 4.5. The non-aging viscous mode is constrained to be constant as well in order to reduce the number of parameters involved in optimization. We follow the same procedure but with two constrained parameters for other temperatures and obtain the model parameters $\mathbb{G}, \mathbb{V}, n, \mu$. for different temperatures. The model fits for relaxation data and frequency response data for T = 37°C and T = 49°C are shown in Fig. 4.4.3 and Fig. 4-28 respectively.

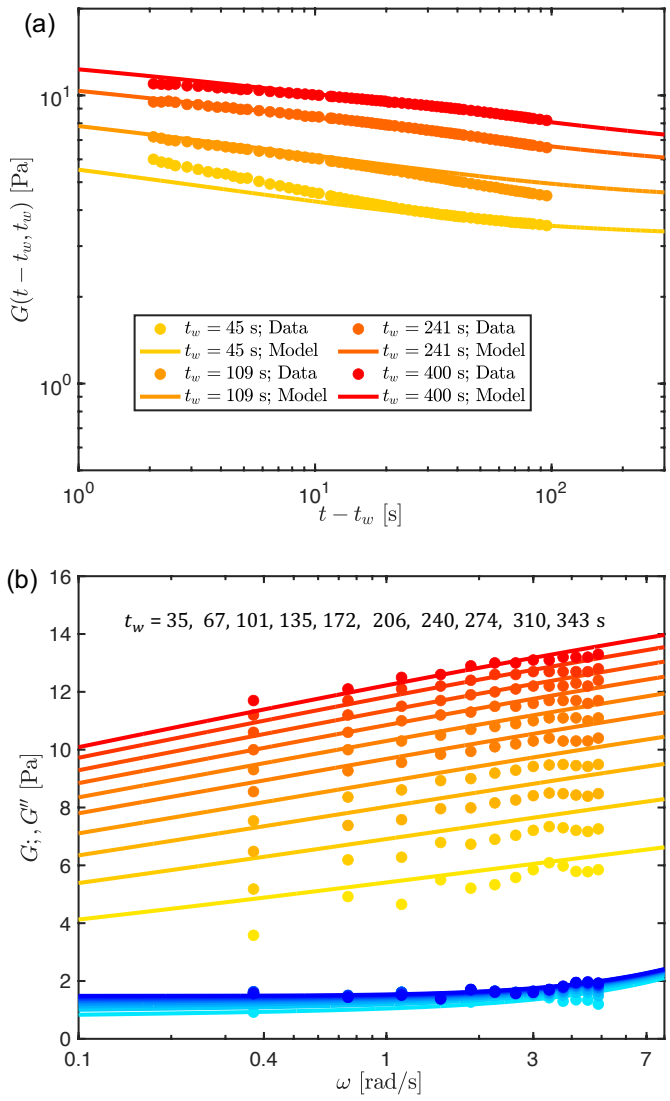

Figure 4-25: (a) Data points and solid lines represent the experimental data and model fits for the relaxation modulus respectively for different wait times at T = 10°C. (b) Red shaded data points and solid lines represent the experimental data and model fits for the storage modulus respectively as a function of frequency for different wait or age times for T = 10°C. Blue shaded solid points and solid lines represent the experimental data and model fits for the loss modulus respectively as a function of frequency for different wait or age times for T = 10°C. Both the red and blue color intensity increases with age time t_w. The model parameters: $\mathbb{G}$ = 19.1 Pa; $\mathbb{V}$ = 29.9 Pa·s$^{\alpha}$; α = 0.19; n = 0.21; μ = 1.62; η_0 = 0.15 Pa·s and the arbitrary reference time chosen is t_R = 300 s.

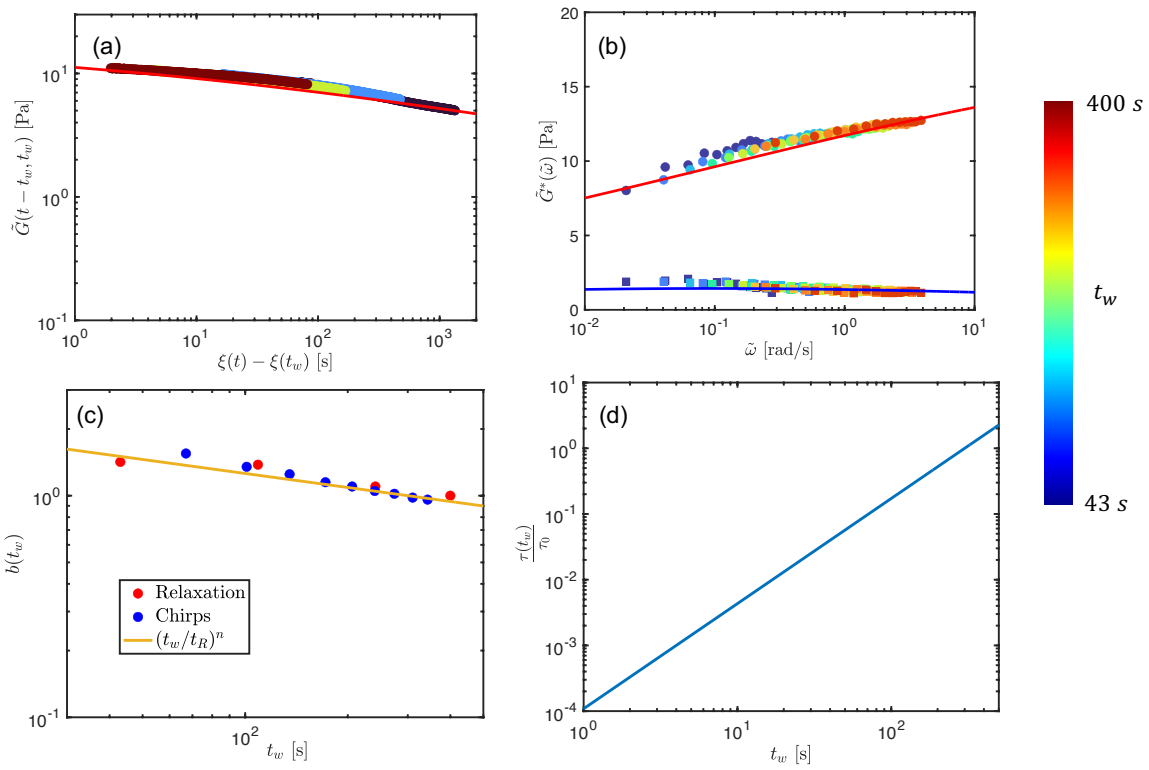

Figure 4-26: (a) Relaxation modulus and (b) complex moduli in material time and frequency domain. The data points are experimental data points transformed to material domain and the fits are the FMG fits with the parameters $\mathbb{G}$ = 19.1 Pa; $\mathbb{V}$ = 29.9 Pa·s$^{\alpha}$; α = 0.19; n = 0.21; μ = 1.6; η_0 = 0.15 and the arbitrary reference time chosen is t_R = 300 s. The different colors used in (a) and (b) represent different age-times t_w as shown by the color bar. (c) The data points are used to superpose the relaxation in frequency domain and the solid line is the fit $\left(\frac{t_w}{t_R}\right)^n$ from the parameter n. (d) The ratio of relaxation time $\tau(t_w)$ and reference relaxation time τ_0 constructed using aging exponent μ. τ_0 is the relaxation time at t_R = 300 s.

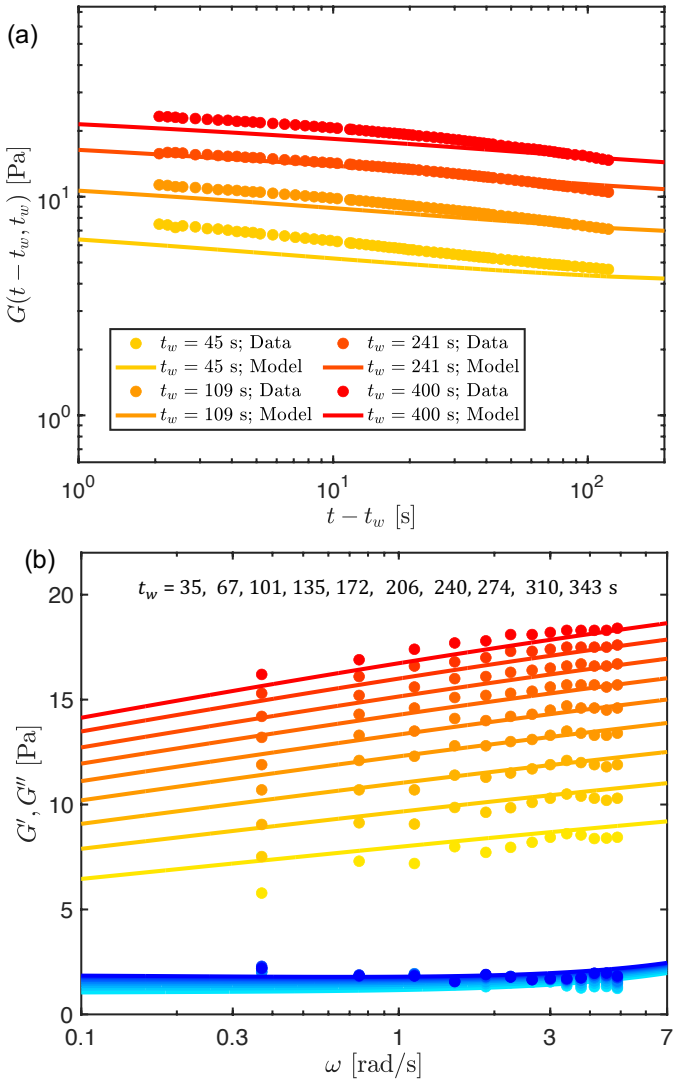

Figure 4-27: (a) Data points and solid lines represent the experimental data and model fits for the relaxation modulus respectively for different wait times at T = 37°C. (b) Red shaded data points and solid lines represent the experimental data and model fits for the storage modulus respectively as a function of frequency for different wait or age times for T = 37°C. Blue shaded solid points and solid lines represent the experimental data and model fits for the loss modulus respectively as a function of frequency for different wait or age times for T = 37°C. Both the red and blue color intensity increases with age time t_w. For, T = 37°C, the model parameters alone are obtained by fitting for relaxation modulus and complex modulus separately due to small sample variability and then interpolated. Interpolated parameters are $\mathbb{G}$ = 26 Pa; $\mathbb{V}$ = 56 Pa·s$^{\alpha}$; α = 0.19; n = 0.42; μ = 1.3; η_0 = 0.15 Pa·s and the arbitrary reference time chosen is t_R = 300 s.

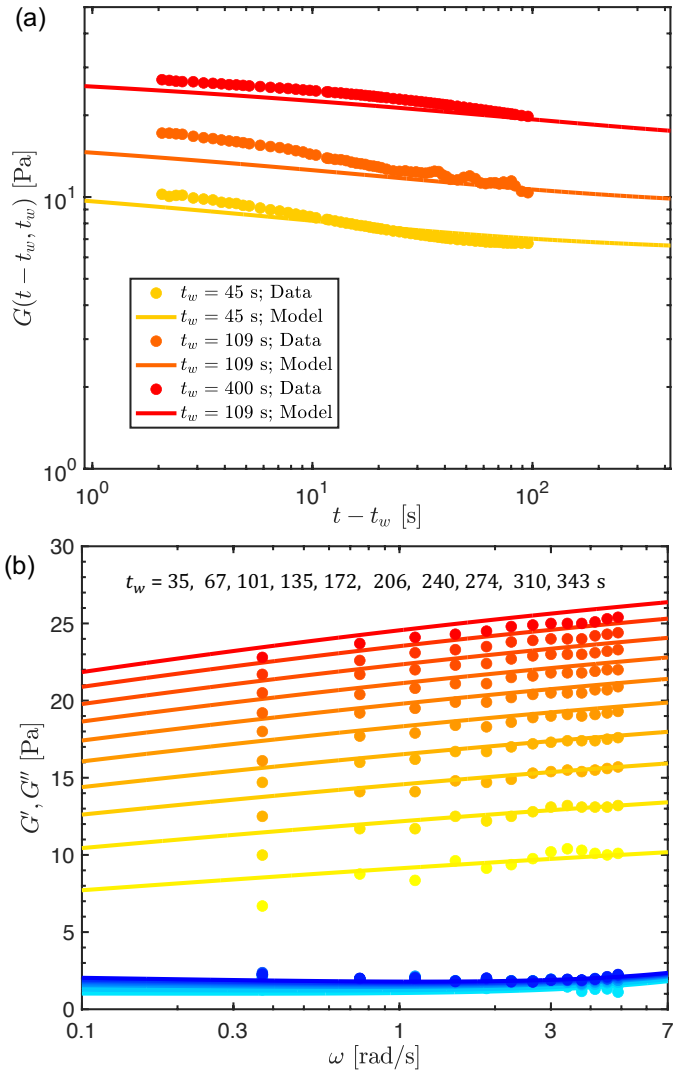

Figure 4-28: (a) Data points and solid lines represent the experimental data and model fits for the relaxation modulus respectively for different wait times at T = 49°C. (b) Red shaded data points and solid lines represent the experimental data and model fits for the storage modulus respectively as a function of frequency for different wait or age times for T = 49°C. Blue shaded solid points and solid lines represent the experimental data and model fits for the loss modulus respectively as a function of frequency for different wait or age times for T = 49°C. Both the red and blue color intensity increases with age time t_w. The model parameters: $\mathbb{G}$ = 30 Pa; $\mathbb{V}$ = 100 Pa·s$^{\alpha}$; α = 0.19; n = 0.37; μ = 1.22; η_0 = 0.15 Pa·s and the arbitrary reference time chosen is t_R = 300 s.

4.5 Discussion

It has been reported in the past [39] that the aging exponent $\mu(T)$ is a linear function of $1/T$. we find this functional form describes our data well as as illustrated in Fig. 4-29.The best fit for μ with $1/T$ as determined by regression to be:

$$\mu(T) = \frac{978}{T} - 1.8 \tag{4.24}$$

where T is in Kelvin scale. The reason for this dependence on the reciprocal temperature is explained in [85] which notes that we expect μ from :

$$\mu \propto \frac{G_0 b^3}{k_B T} \tag{4.25}$$

where k_B is the Boltzmann constant and T is the absolute temperature so $k_B T$ gives a characteristic energy density in the thermally aging soft glass. G_0 is the elastic modulus of the bentonite dispersion and b is the characteristic length scale of the particles dispersed in the dispersion so that $G_0 b^3$ represents the elastic energy scale in the material. Assuming $G_0 \approx 10$ Pa and using Eq. (4.24), we obtain the value of b to be 10^{-7} m or 10 μm using which is on the same order of the length scale of the bentonite particles as observed from SEM images, Fig. 4-2. This paves the way for connecting the bulk rheological experiments to the microstructural theories for disc shaped particles.

We briefly discuss here the temperature superposition for the data obtained at different temperatures. To superpose the data to a reference temperature (T_{ref}) in the material time and frequency domain, we make use of the FMG constitutive model in the material domain. For the data at different temperatures to superpose to the reference FMG model denoted by $\mathbb{G}_{ref}$ at our reference temperature, we need time temperature superposition to be obeyed in the material time domain:

$$\frac{\mathbb{V}(T_{ref})(i\tilde{\omega})^{\alpha}}{1 + \frac{\mathbb{V}(T_{ref})}{\mathbb{G}(T_{ref})}(i\tilde{\omega})^{\alpha}} = b_T \frac{\mathbb{V}(T_i)(i(\tilde{\omega}/a_T))^{\alpha}}{1 + \frac{\mathbb{V}(T_i)}{\mathbb{G}(T_i)}(i(\tilde{\omega}/a_T))^{\alpha}} \tag{4.26}$$

where $\mathbb{V}(T_{ref})$, $\mathbb{G}(T_{ref})$ and $\mathbb{V}(T_i)$, $\mathbb{G}(T_i)$ are the model parameters at the reference temper-

ature and the individual test temperatures at which we are interested in collapsing to the reference FMG curve respectively. For Eq. (4.26), to hold we require the vertical b_T and horizontal a_T shift factors for temperature superposition to be:

$$b_{T_i} = \frac{\mathbb{G}_{ref}}{\mathbb{G}_i} \tag{4.27}$$

$$a_{T_i} = \left(\frac{\mathbb{G}_{ref}\mathbb{V}_i}{\mathbb{G}_i\mathbb{V}_{ref}}\right)^{1/\alpha} \tag{4.28}$$

The characteristic relaxation time constant for FMG is given by $\tilde{\tau} = \left(\frac{\mathbb{V}}{\mathbb{G}}\right)^{\frac{1}{\alpha}}$. Therefore Eq.

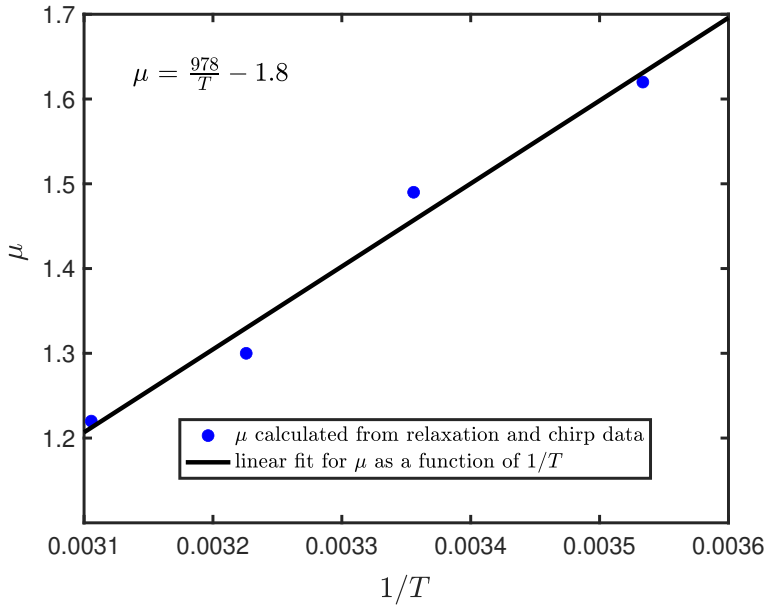

Figure 4-29: The aging exponent μ vs 1/T is plotted as a function of the reciprocal of temperature. The blue filled data points represent the values of μ calculated from experimental data of relaxation modulus and complex modulus at T = 10°C, 25°C, 37°C, 49°C. The solid black line represent a linear fit for the aging exponent μ as a function of of the reciprocal of temperature. In the plot, the temperature considered is in Kelvin scale.

(4.28) can also be rewritten in terms of the characteristic relaxation time of the FMG in material time domain as:

$$a_{T_i} = \frac{\tilde{\tau}_i}{\tilde{\tau}_{ref}} \tag{4.29}$$

The values of the six parameters of the aging FMG model with non-aging viscous mode for

different temperatures along with characteristic relaxation time in material time, horizontal shift factors a_{T_i} and vertical shift factors b_{T_i} calculated with $T_{ref} = 49°C$ is tabulated:

T [°C]	$\mathbb{G}$ [Pa]	$\mathbb{V}$ [Pa·s$^{\alpha}$]	α	μ	η_0	n	$\tilde{\tau}$ [s]	a_T	b_T
10	19.1	29.9	0.19	1.62	0.15	-0.21	10.6 s	0.018	1.57
25	19	59	0.19	1.49	0.15	-0.41	389 s	0.69	1.57
37	26	56	0.19	1.3	0.15	-0.42	56.7 s	0.1	1.15
49	30	100	0.19	1.22	0.15	-0.37	564 s	1	1

Table 4.2: Values of model parameters for bentonite dispersion at different temperatures. The reference temperature $T_{ref} = 49°C$ is considered for calculating horizontal shift factors a_T and vertical shift factors b_T.

Chapter 5

Conclusion and Future works

This thesis dealt with three different subjects connected through the central topic of time-resolved rheology. We focused on applying existing state of the art, time-resolved rheometry techniques such as OWCh to gain rheological insights on a weakly associated physical gel alginate through superposition rheometry and on a soft glassy material consisting of bentonite dispersions. We also developed a more advanced time-resolved technique '*Gaborheometry*' and demonstrated in detail the protocol and applications in rheology.

In chapter 2, we demonstrated that the conventional protocol used in superposition rheometry of superimposing a SAOS frequency sweep with steady shear flow can be replaced by superposition of an Optimally Windowed Chirp (OWCh) imposed orthogonally to a with steady shear flow. This reduces the experimental time required to determine the frequency spectrum and can also monitor the transient evolution of the complex modulus for mutating materials. We presented a novel methodology to investigate flow induced anisotropy by comparing the relaxation spectrum measured in the flow direction and in the perpendicular direction to the steady shear flow. The work presented here suggests future work on quantifying the degree of flow induced anisotropy and how it increases with shear rate. The present study also informs us of the outstanding need to develop rigorous constitutive equations which take into consideration the flow induced anisotropy.

Secondly, in chapter 3, we developed a novel time-resolved rheometric protocol, '*Gaborheometry*' using discrete Gabor transform to obtain the temporal evolution of the complex modulus in an aging or mutating material for a specified deformation frequency. For rapidly

mutating systems in which the mutation number Mu cannot be reduced to $Mu \leq 0.15$ even whilst using OWCh protocol, Gaborheometry remains the only approach to obtain accurate measurements of the time dependent complex moduli information for different frequencies. We also presented other applications of discrete Gabor transforms in rheometry such as: (i) quick extraction of non-linear Fourier and Chebyshev coefficients using an amplitude-modulated signal for a specified deformation frequency and (ii) extraction of transient and steady state complex modulus or compliance data accurately from the initial transient response following the inception of oscillatory flow. Future work, beyond the scope of this thesis, will focus on investigating more advanced signal processing techniques such as applications of wavelets or multi-tone signals for applications in time-resolved rheometry and automating the rheological experiments.

Finally, in chapter 3, we investigated the rheological aging behavior of 5 wt.% bentonite dispersion by monitoring the evolution of the linear viscoelastic response with age time at four different temperatures. By using a time domain transformation from the laboratory time to material time combined with a Fractional Maxwell Gel (FMG) model, we formulated a six parameter constitutive theory to model the dependence of the linear viscoelastic response of the bentonite dispersion at different temperatures. The parameter fits enable interpolation of the values at intermediate temperatures to make forward predictions of the linear properties of bentonite dispersions in previously unstudied conditions. The resulting time—age–time—temperature superposition (tatTs) formulation can be extended to a range of soft glassy materials and mutating colloidal gels such as clay-based systems. In the future, we plan to extend the study on bentonite dispersions by linking the rheological data and modeling presented, to microstructural theories for disc shaped particles.

Appendix A

Point of inflection of rate dependent spectra $H_{rz}(\tau, \dot{\gamma})$)

The rate dependent spectra H_{rz} under the application of non-linear large deformation (uni-directional shear) undergoes a reduction of spectrum at long time scales.

$$H_{rz}(\tau, \dot{\gamma}) = \frac{1}{\pi} \frac{\mathbb{G}\lambda(\dot{\gamma})^{1-\beta}\tau^{-1}\sin(\pi\beta)}{\lambda(\dot{\gamma})^{1-\beta}\tau^{\beta-1} + \lambda(\dot{\gamma})^{\beta-1}\tau^{(1-\beta)} + 2\cos(\pi(1-\beta))} \tag{A.1}$$

The point of inflection of the function provides a appropriate time scale after which the spectrum gets reduced or scale as $\tau^{-(2-\beta)}$. To obtain the point of inflection, the relaxation time at which second derivative of the rate dependent spectrum H_{rz} is found. For $\beta = 0.33$, we find the point of inflection to be around the characteristic time constant $\lambda(\dot{\gamma})$.

$$\frac{\partial^2 H_{rz}(\tau, \dot{\gamma})}{\partial \tau^2}\Big|_{\tau=\lambda(\dot{\gamma})} \approx 0 \tag{A.2}$$

This informs us that for relaxation times scales greater than $\lambda(\dot{\gamma})$, we observe a reduction of spectrum which scales with relaxation time as $\tau^{-(2-\beta)}$.

Appendix B

Gaborheometry: Time Frequency uncertainty

There is always a trade-off in using the short time Fourier transform techniques between the frequency and time resolution. Longer the window, better the frequency resolution but poor time resolution and shorter the window, better the time resolution but poor frequency resolution. The time frequency spread around Gaussian obeys Heisenberg uncertainty principle [57, 11].

$$\left(\int_{-\infty}^{\infty} t^2 |g(t)|^2 dt \right) \left(\int_{-\infty}^{\infty} \omega^2 |\tilde{g}(\omega)|^2 d\omega \right) \geq \frac{1}{16\pi^2} \tag{B.1}$$

The function inside the time integral is the variance of the time signal $g(t)$ and the function inside the frequency integral is the variance of $\tilde{g}(\omega)$ which is the Fourier transform of $g(t)$ in frequency space. For a Gaussian time signal, the Fourier transform also results in a Gaussian function. To illustrate the time-frequency uncertainty principle, we consider the signal:

$$x(t) = \begin{cases} \sin(1t) & t < 15\pi \\ \sin(5t) & t > 15\pi \end{cases} \tag{B.2}$$

The DGT spectrum of the Eq. (B.2) for two different window lengths ($a = 2.6$ s and $a = 26$ s) are shown in Fig. B-1. The Δt and $\Delta\omega$ are the characteristic time and frequency resolution to which time and frequency information can be resolved accurately. A good

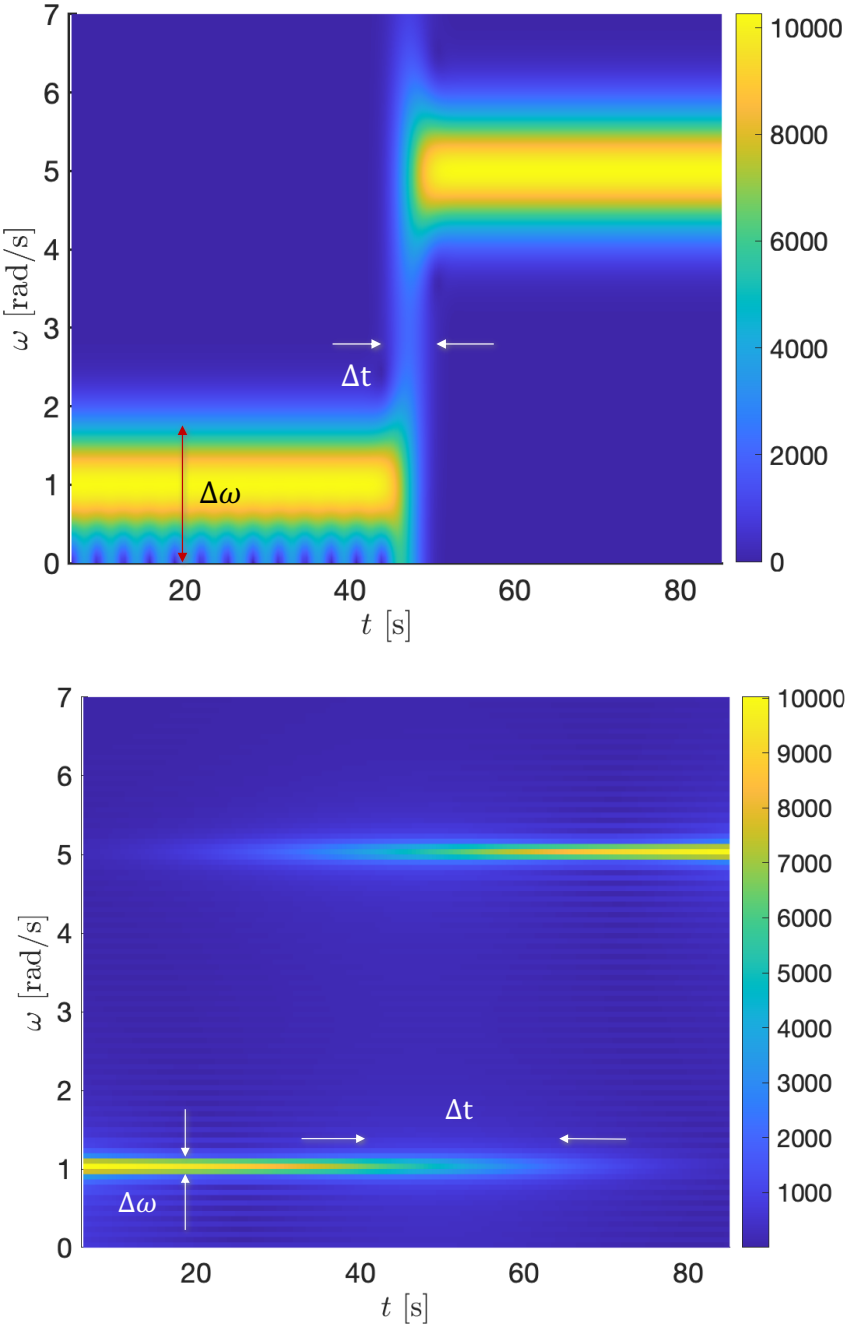

Figure B-1: (a) DGT spectrum of Eq. (B.2) with $a = 2.6$ s. (b) DGT spectrum of Eq. (B.2) with $a = 26$ s. As the time resolution increases, the frequency resolution decreases and vice-versa.

estimate of Δt is two times the standard deviation ($2a$) of the distribution in time of the Gaussian window used to traverse the time signal and a good estimate of $\Delta\omega$ is two times the standard deviation of the distribution of the amplitude spectrum in frequency space. As observed in Fig. B-1, for $a = 2.6$ s, the Δt is lower than of the Δt for $a = 26$ s. But, $\Delta\omega$ is lower for $a = 26$ s, when compared to $a = 2.6$ s. Therefore, as one improves the time resolution by decreasing window length, the frequency resolution worsens and vice-versa constituting the time-frequency uncertainty principle.

Appendix C

Signatures of hyperaging ($\mu > 1$)

We present here the signatures that identify the phenomena of hyperaging in soft glassy systems that exhibit rheological aging. For $\mu > 1$, the conversion formula from lab time to material time given in Eq. (4.13) can be rewritten more clearly as:

$$\tilde{t} = \xi(t) - \xi(t_w) = \frac{t_R^{\mu}}{\mu - 1}\left[\frac{1}{t_w^{\mu-1}} - \frac{1}{t^{\mu-1}}\right] \tag{C.1}$$

where t is the total time elapsed after the cessation of pre-shear and t_w is the age time or the waiting time of the bentonite dispersion. The age time t_w and the time elapsed t for different rheological experiments can be visualized from Fig. 4-21 in chapter 4. The dependence between the material time domain and laboratory time domain is illustrated in Fig. C-1 by utilizing Eq. (C.1). The material time reaches an asymptote as the laboratory time increases and is given by:

$$lim_{t\to\infty}\ \ \xi(t) - \xi(t_w) = \tilde{t}_{asymp} = \frac{t_R^{\mu}}{\mu - 1}\left[\frac{1}{t_w^{\mu-1}}\right] \tag{C.2}$$

As seen in Eq. (C.2), the material time asymptote is dependent on the age time t_w, aging exponent μ and on the arbitrary reference time t_R chosen to observe the material time window. The material time asymptote can be thought of as a frame-dependent limiting quantity which depends on the frame of reference chosen. Analogously, the arbitrarily chosen reference time t_R can be thought of as the reference point compared to which we observe the material time domain. The material time stops at a certain value $\tilde{t}_{asymp}$ and does not go beyond it even as the real time approaches infinity. In other words, due to hyperaging ($\mu > 1$),

the material time gets arrested at a certain value as real time progresses to infinity. From Eq. (C.2), it can be seen that as the wait time or age time t_w increases, the asymptote of material time decreases. Although, mathematically the $\tilde{t}_{asymp}$ is reached only at infinite laboratory time, a good approximation of the laboratory time at which the plateau in material time is reached can be calculated. At short laboratory time $fract - t_w t_w \ll 1$, the material time is linearly dependent on lab time with a scaling factor that depends how far t_w is from t_R and on μ.

$$lim_{t\to 0} \;\; \xi(t) - \xi(t_w) = \left(\frac{t_R}{t_w}\right)^{\mu} (t - t_w) \tag{C.3}$$

The short time asymptote given by Eq. (C.3) can be equated to the asymptote of material time Eq. (C.2), to obtain characteristic time scale in the laboratory frame ($\lambda_{plateau}$) beyond which the material time domain reaches a plateau.

$$\lambda_{plateau} = \left(\frac{\mu}{\mu - 1}\right) t_w \tag{C.4}$$

This suggest that the time taken for the material time to reach a plateau increases linearly with the laboratory wait time or age time.

Therefore, for hyperaging materials, at a particular age time t_w, the information conveyed by the relaxation modulus $\tilde{G}$ in the material time domain exist only between $\tilde{t} = 0$ to $\tilde{t} = \tilde{t}_{asymp}(t_w)$. This can be visualized in Fig. C-2 for two different age times $t_w = 45$ s and $t_w = 320$ s. For laboratory time greater than $t = \lambda_{plateau}$, the material time reaches a plateau of $\tilde{t} = \tilde{t}_{asymp}(t_w)$ whose relaxation modulus is $\tilde{G}\left(\tilde{t}_{asymp}(t_w)\right)$. Therefore, the relaxation modulus (G) in laboratory time reaches a plateau for times greater than $t = \lambda_{plateau}$ whose value can be calculated as $G_\infty(t_w) = \tilde{G}\left(\tilde{t}_{asymp}(t_w)\right)/b(t_w)$ from Eq. (4.14). The plateau observed in the relaxation modulus in lab time is because the material time gets arrested to $\tilde{t} = \tilde{t}_{asymp}(t_w)$ with $\tilde{G}\left(\tilde{t}_{asymp}(t_w)\right)$ and cannot go beyond it even as the lab time increases to infinity. The relaxation modulus plateau in laboratory time can be observed in Fig. C-3 for different age times t_w with the plateau modulus values $G_\infty(t_w) = \tilde{G}\left(\tilde{t}_{asymp}(t_w)\right)/b(t_w)$. We use the form $b(t_w) = \left(\frac{t_w}{t_R}\right)^n$ for the vertical shift factor.

Consequently, two experimental signatures can be considered to identify the hyperaging behavior of collidal gels and glasses:

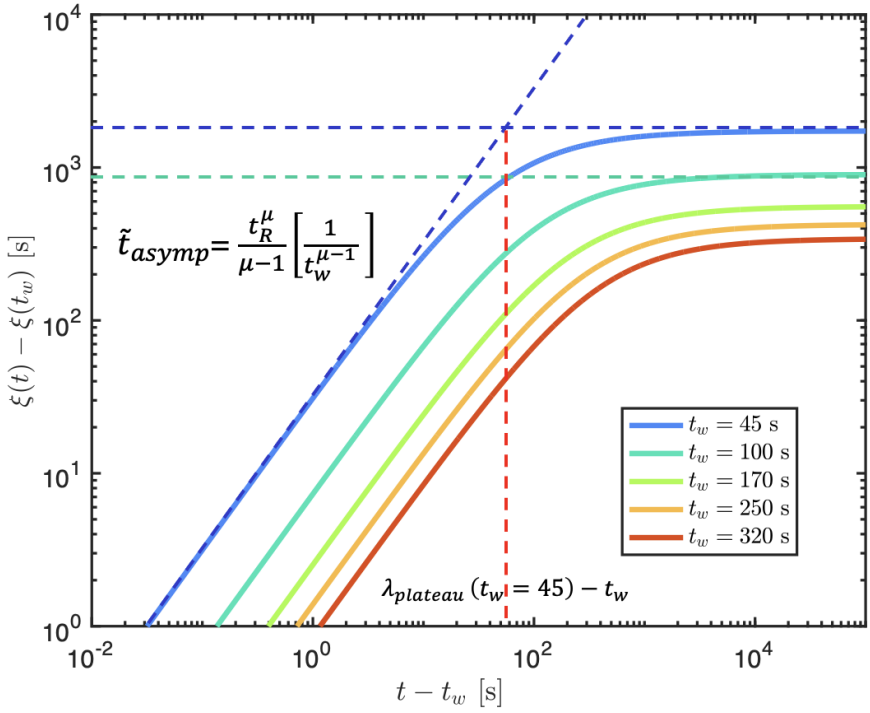

Figure C-1: The dependence of material time with laboratory time for different age times is plotted for $t_R = 300$ s and $\mu = 1.8$. The material time aymptote decreases as the age time increases.

(i) The increase of relaxation modulus plateau with age time.

(ii) The laboratory time taken to reach the relaxation modulus plateau increases roughly linearly with age time of the gel as specified in Eq. (C.4).

Eq. (C.4) also presents an alternative and more easier way to find the aging exponent μ in aging systems. The traditional way of obtaining the aging exponent μ in aging systems is by transformation of laboratory time to material time using μ and determining the value the μ which gives the best superposition of relaxation modulus with the choice of vertical shift factors $b(t_w)$. Instead, one can utilize Eq. (C.4) to find the aging exponent μ by plotting the laboratory time it takes for the relaxation modulus to reach a plateau $\lambda_{plateau}$ against different age times t_w. Linear regression maybe used between the experimental plateau times $\lambda_{plateau}$ and age times t_w and its slope can be equated to $\mu/(\mu - 1)$ following Eq. (C.4) to calculate the aging exponent μ. This method also decouples the conventional process of finding aging exponent μ and vertical shift factors $b(t_w)$ together.

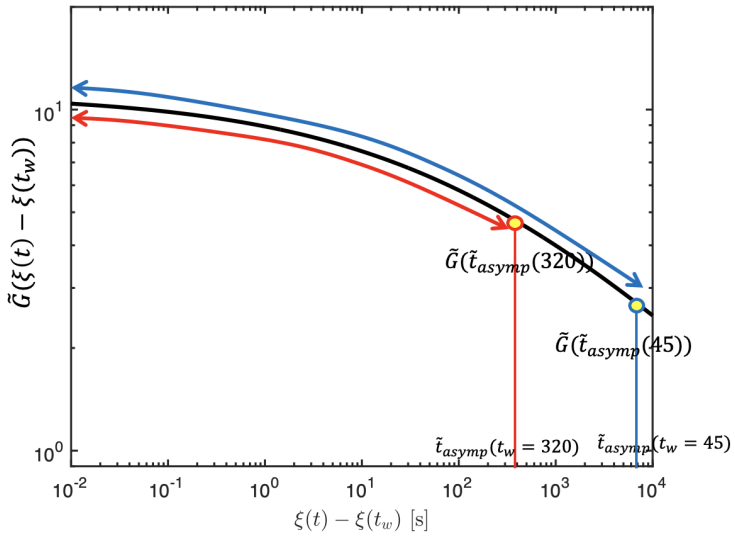

Figure C-2: The relaxation modulus using fractional Maxwell gel model (FMG) with paramters $\mathbb{G} = 11.1$ Pa, $\mathbb{V} = 51.5$ Pa·s$^{\alpha}$, $\alpha = 0.28$ is represented in material time. The aging exponent and reference time in the material time are $\mu = 1.8$ and $t_R = 300$ s respectively. The available information of relxation modulus in material time for two different times $t_w = 45$ s and $t_w = 320$ s are represented using blue and red solid double arrows respectively.

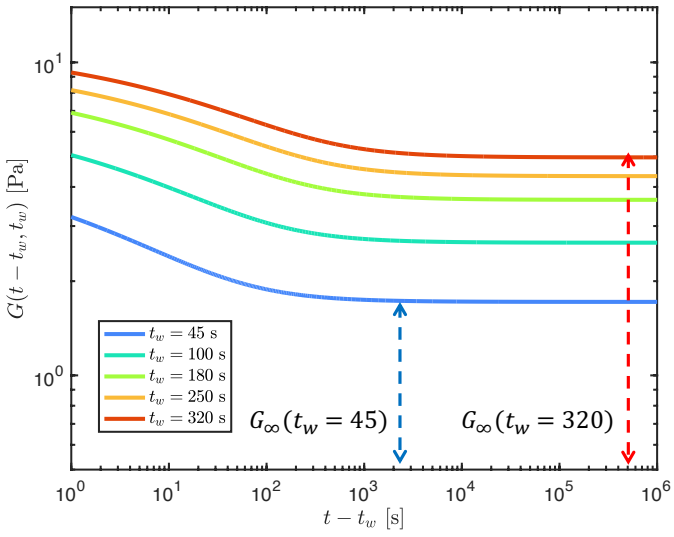

Figure C-3: The corresponding relaxation modulus in laboratory time for the relaxation modulus $\tilde{G}$ represented in Fig. C-2 in material time using $b(t_w) = \left(\frac{t_w}{t_R}\right)^n$. The complete set of parameters required to construct these curves are $\mathbb{G} = 11.1$ Pa, $\mathbb{V} = 51.5$ Pa·s$^{\alpha}$, $\alpha = 0.28$, $\mu = 1.8$, $t_R = 300$ s, $n = -0.36$.

Bibliography

[1] Mayank Agarwal and Yogesh M. Joshi. Signatures of physical aging and thixotropy in aqueous dispersion of Carbopol. *Physics of Fluids*, 31(6):063107, June 2019. Publisher: American Institute of Physics.

[2] Varun Awasthi and Yogesh M. Joshi. Effect of temperature on aging and time–temperature superposition in nonergodic laponite suspensions. *Soft Matter*, 5(24):4991–4996, 2009. Publisher: Royal Society of Chemistry.

[3] Bharat Baldewa and Yogesh M. Joshi. Thixotropy and physical aging in acrylic emulsion paint. *Polymer Engineering & Science*, 51(10):2085–2092, 2011. _eprint: https://onlinelibrary.wiley.com/doi/pdf/10.1002/pen.22078.

[4] Ranjini Bandyopadhyay, P. Harsha Mohan, and Yogesh M. Joshi. Stress relaxation in aging soft colloidal glasses. *Soft Matter*, 6(7):1462–1466, 2010. Publisher: Royal Society of Chemistry.

[5] Paul Becher. A Review of: "Foundations of Colloid Science, Vol. 1, Robert J. Hunter (written in the collaboration of L. R. White, L. R. Fisher, N. Parker, R. M. pashley, D. H. Napper, R. W. O'Brien, J. Ralston, F. Grieser).Clarendon Press, Oxford University Press, New York, 1987. pp. xi +673. $115.00. *Journal of Dispersion Science and Technology*, 9(4):425–426, January 1988.

[6] B Bernstein, E A Kearsley, and L J Zapas. A Study of Stress Relaxation with Finite Strain. *Transactions of the Society of Rheology*, 7:391–410, 1963.

[7] R. B. Bird, R. C. Armstrong, and O. Hassager. *Dynamics of polymeric liquids bird.pdf*. John Wiley & Sons, New York, 1987.

[8] R. Byron Bird and A. Jeffrey Giacomin. Who conceived the "complex viscosity"? *Rheologica Acta*, 51(6):481–486, June 2012.

[9] Mehdi Bouzid, Bavand Keshavarz, Michela Geri, Thibaut Divoux, Emanuela Del Gado, and Gareth H. McKinley. Computing the linear viscoelastic properties of soft gels using an optimally windowed chirp protocol. *Journal of Rheology*, 62(4):1037–1050, July 2018. Publisher: The Society of Rheology.

[10] Anders Brandt. Spectrum and Correlation Estimates Using the DFT. In *Noise and Vibration Analysis*, pages 205–243. John Wiley & Sons, Ltd. Section: 10 _eprint: https://onlinelibrary.wiley.com/doi/pdf/10.1002/9780470978160.ch10.

[11] Steven L. Brunton and J. Nathan Kutz. *Data-Driven Science and Engineering: Machine Learning, Dynamical Systems, and Control*. Cambridge University Press, February 2019. Google-Books-ID: jkSIDwAAQBAJ.

[12] Gabriele Colombo, Sunhyung Kim, Thomas Schweizer, Bram Schroyen, Christian Clasen, Jan Mewis, and Jan Vermant. Superposition rheology and anisotropy in rheological properties of sheared colloidal gels. *Citation: Journal of Rheology*, 61:1035, 2017.

[13] Théau Conte and Mohend Chaouche. Parallel superposition rheology of cement pastes. *Cement and Concrete Composites*, 104, 2019. Publisher: Elsevier Ltd.

[14] Leendert Cornelis, Elisa Struik, Natuurkundig Ingenieur, Prof Dr, D. W. Van Krevelen, Aan Hilde, and Chemische Werke Huls. *aging in amorphous polymers*.

[15] P. Coussot, H. Tabuteau, X. Chateau, L. Tocquer, and G. Ovarlez. Aging and solid or liquid behavior in pastes. *Journal of Rheology*, 50(6):975–994, November 2006. Publisher: The Society of Rheology.

[16] D J Curtis and A R Davies. On response spectra and Kramers-Kronig relations in superposition rheometry. *Physics of Fluids*, 31(12), 2019. Publisher: American Institute of Physics Inc.

[17] D. J. Curtis and A. R. Davies. On shear-rate dependent relaxation spectra in superposition rheometry: A basis for quantitative comparison/interconversion of orthogonal and parallel superposition moduli. *Journal of Non-Newtonian Fluid Mechanics*, 274(October), 2019.

[18] D. J. Curtis, A. Holder, N. Badiei, J. Claypole, M. Walters, B. Thomas, M. Barrow, D. Deganello, M. R. Brown, P. R. Williams, and K. Hawkins. Validation of Optimal Fourier Rheometry for rapidly gelling materials and its application in the study of collagen gelation. *Journal of Non-Newtonian Fluid Mechanics*, 222:253–259, August 2015.

[19] J. G. Daugman. Complete discrete 2-D Gabor transforms by neural networks for image analysis and compression. *IEEE Transactions on Acoustics, Speech, and Signal Processing*, 36(7):1169–1179, July 1988. Conference Name: IEEE Transactions on Acoustics, Speech, and Signal Processing.

[20] Jan K G Dhont and Norman J Wagner. Superposition rheology.

[21] Christopher J. Dimitriou, Randy H. Ewoldt, and Gareth H. McKinley. Describing and prescribing the constitutive response of yield stress fluids using large amplitude oscillatory shear stress (LAOStress). *Journal of Rheology*, 57(1):27–70, January 2013.

[22] D. L. Donoho, M. Vetterli, R. A. DeVore, and I. Daubechies. Data compression and harmonic analysis. *IEEE Transactions on Information Theory*, 44(6):2435–2476, October 1998. Conference Name: IEEE Transactions on Information Theory.

[23] Konraad Dullaert and Jan Mewis. Thixotropy: Build-up and breakdown curves during flow. *Journal of Rheology*, 49(6):1213–1230, October 2005. Publisher: The Society of Rheology.

[24] J. A. Epaarachchi. 17 - The effect of viscoelasticity on fatigue behaviour of polymer matrix composites. In Rui Miranda Guedes, editor, *Creep and Fatigue in Polymer Matrix Composites*, Woodhead Publishing Series in Composites Science and Engineering, pages 492–513. Woodhead Publishing, January 2011.

[25] R. H. Ewoldt, A. E. Hosoi, and G. H. McKinley. Nonlinear viscoelastic biomaterials: meaningful characterization and engineering inspiration. *Integrative and Comparative Biology*, 49(1):40–50, July 2009.

[26] Randy H. Ewoldt. Defining nonlinear rheological material functions for oscillatory shear. *Journal of Rheology*, 57(1):177–195, January 2013.

[27] Randy H Ewoldt and N Ashwin Bharadwaj. Low-dimensional intrinsic material functions for nonlinear viscoelasticity. *Rheol Acta*, page 19, 2013.

[28] Randy H. Ewoldt, Christian Clasen, A. E. Hosoi, and Gareth H. McKinley. Rheological fingerprinting of gastropod pedal mucus and synthetic complex fluids for biomimicking adhesive locomotion. *Soft Matter*, 3(5):634–643, April 2007. Publisher: The Royal Society of Chemistry.

[29] Randy H. Ewoldt, A. E. Hosoi, and Gareth H. McKinley. New measures for characterizing nonlinear viscoelasticity in large amplitude oscillatory shear. *Journal of Rheology*, 52(6):1427–1458, November 2008.

[30] Randy H. Ewoldt, Peter Winter, Jason Maxey, and Gareth H. McKinley. Large amplitude oscillatory shear of pseudoplastic and elastoviscoplastic materials. *Rheologica Acta*, 49(2):191–212, February 2010.

[31] Hans G. Feichtinger and Thomas Strohmer. *Gabor Analysis and Algorithms: Theory and Applications*. Springer Science & Business Media, December 2012. Google-Books-ID: mfLxBwAAQBAJ.

[32] Rubens Rosario Fernandes, Guilherme Turezo, Diogo E. V. Andrade, Admilson T. Franco, and Cezar Otaviano Ribeiro Negrão. Are the rheological properties of water-based and synthetic drilling fluids obtained by the Fann 35A viscometer reliable? *Journal of Petroleum Science and Engineering*, 177:872–879, June 2019.

[33] S. M. Fielding, P. Sollich, and M. E. Cates. Aging and rheology in soft materials. *Journal of Rheology*, 44(2):323–369, March 2000.

[34] D. Gabor. Theory of communication. Part 1: The analysis of information. *Journal of the Institution of Electrical Engineers - Part III: Radio and Communication Engineering*, 93(26):429–441, November 1946. Publisher: IET Digital Library.

[35] Michela Geri, Bavand Keshavarz, Thibaut Divoux, Christian Clasen, Daniel J. Curtis, and Gareth H. McKinley. Time-Resolved Mechanical Spectroscopy of Soft Materials via Optimally Windowed Chirps. *Physical Review X*, 8(4):041042, December 2018.

[36] Etienne Ghiringhelli, Denis Roux, Didier Bleses, Helene Galliard, and Francois Caton. Optimal fourier rheometry: Application to the gelation of an alginate. *Rheologica Acta*, 51(5):413–420, May 2012.

[37] R. Greene-Kelly. Irreversible dehydration in montmorillonite. *Clay Minerals Bulletin*, 1(7):221–227, June 1952. Publisher: Cambridge University Press.

[38] Grim, R. E. *Applied Clay Mineralogy*. McGraw-Hill, 1962.

[39] Rahul Gupta, Bharat Baldewa, and Yogesh M. Joshi. Time temperature superposition in soft glassy materials. *Soft Matter*, 8(15):4171–4176, 2012. Publisher: Royal Society of Chemistry.

[40] Frode K. Hansen, Krzysztof M. Górski, and Eric Hivon. Gabor transforms on the sphere with applications to CMB power spectrum estimation. *Monthly Notices of the Royal Astronomical Society*, 336(4):1304–1328, November 2002.

[41] Fredric J. Harris. On the Use of Windows for Harmonic Analysis with the Discrete Fourier Transform. *Proceedings of the IEEE*, 66(1):51–83, 1978.

[42] Ole Hassager. Stress-controlled oscillatory flow initiated at time zero: A linear viscoelastic analysis. *Journal of Rheology*, 64(3):545–550, May 2020.

[43] Niels Holten-Andersen, Matthew J. Harrington, Henrik Birkedal, Bruce P. Lee, Phillip B. Messersmith, Ka Yee C. Lee, and J. Herbert Waite. pH-induced metal-ligand cross-links inspired by mussel yield self-healing polymer networks with near-covalent elastic moduli. *Proceedings of the National Academy of Sciences of the United States of America*, 108(7):2651–2655, February 2011.

[44] Kyu Hyun, Manfred Wilhelm, Christopher O. Klein, Kwang Soo Cho, Jung Gun Nam, Kyung Hyun Ahn, Seung Jong Lee, Randy H. Ewoldt, and Gareth H. McKinley. A review of nonlinear oscillatory shear tests: Analysis and application of large amplitude oscillatory shear (LAOS). *Progress in Polymer Science*, 36(12):1697–1753, December 2011.

[45] G. Ianniruberto and G. Marrucci. On compatibility of the Cox-Merz rule with the model of Doi and Edwards. *Journal of Non-Newtonian Fluid Mechanics*, 65(2-3):241–246, 1996. Publisher: Elsevier.

[46] Aditya Jaishankar and Gareth H. McKinley. Power-law rheology in the bulk and at the interface: quasi-properties and fractional constitutive equations. *Proceedings of the Royal Society A: Mathematical, Physical and Engineering Sciences*, 469(2149):20120284, 2013. Publisher: Royal Society.

[47] Aditya Jaishankar and Gareth H Mckinley. A fractional K-BKZ constitutive formulation for describing the nonlinear rheology of multiscale complex fluids. *Citation: Journal of Rheology*, 58:1751, 2014.

[48] Jie Yao, P. Krolak, and C. Steele. The generalized Gabor transform. *IEEE Transactions on Image Processing*, 4(7):978–988, July 1995. Conference Name: IEEE Transactions on Image Processing.

[49] Yogesh Joshi. Dynamics of Colloidal Glasses and Gels. *Annual review of chemical and biomolecular engineering*, 5, March 2014.

[50] Yogesh M. Joshi and G. Ranjith K. Reddy. Aging in a colloidal glass in creep flow: Time-stress superposition. *Physical Review E*, 77(2):021501, February 2008.

[51] Yogesh M Joshi, G.Ranjith K Reddy, Ajit L Kulkarni, Nishant Kumar, and Raj P Chhabra. Rheological behaviour of aqueous suspensions of laponite: new insights into the ageing phenomena. *Proceedings of the Royal Society A: Mathematical, Physical and Engineering Sciences*, 464(2090):469–489, February 2008. Publisher: Royal Society.

[52] Manish Kaushal and Yogesh M. Joshi. Linear viscoelasticity of soft glassy materials. *Soft Matter*, 10(12):1891–1894, 2014. Publisher: Royal Society of Chemistry.

[53] Vassilios C Kelessidis. Yield Stress of Bentonite Dispersions. *open access*, 1(1):12, 2017.

[54] R. Keren, I. Shainberg, and Eva Klein. Settling and Flocculation Value of Sodium-Montmorillonite Particles in Aqueous Media. *Soil Science Society of America Journal*, 52(1):76–80, 1988.

[55] Bavand Keshavarz, Donatien Gomes Rodrigues, Jean-Baptiste Champenois, Matthew G. Frith, Jan Ilavsky, Michela Geri, Thibaut Divoux, Gareth H. McKinley, and Arnaud Poulesquen. Time–connectivity superposition and the gel/glass duality of weak colloidal gels. *Proceedings of the National Academy of Sciences*, 118(15):e2022339118, April 2021.

[56] Sunhyung Kim, Jan Mewis, Christian Clasen, and Jan Vermant. Superposition rheometry of a wormlike micellar fluid. *Rheologica Acta*, 52(8-9):727–740, 2013. Publisher: Springer Verlag.

[57] J. Nathan Kutz. *Data-Driven Modeling & Scientific Computation: Methods for Complex Systems & Big Data*. OUP Oxford, August 2013.

[58] Y. Kwon and A. I. Leonov. Remarks on orthogonal superposition of small amplitude oscillations on steady shear flow. *Rheologica Acta*, 32(1):108–112, 1993. Publisher: Steinkopff-Verlag.

[59] Salim Lahmiri and Mounir Boukadoum. Hybrid Discrete Wavelet Transform and Gabor Filter Banks Processing for Features Extraction from Biomedical Images. *Journal of Medical Engineering*, 2013:1–13, April 2013.

[60] Ronald G. Larson and Yufei Wei. A review of thixotropy and its rheological modeling. *Journal of Rheology*, 63(3):477–501, May 2019. Publisher: The Society of Rheology.

[61] Johnny Ching-Wei Lee, Yu-Tong Hong, Katie M. Weigandt, Elizabeth G. Kelley, Hyunjoon Kong, and Simon A. Rogers. Strain shifts under stress-controlled oscillatory shearing in theoretical, experimental, and structural perspectives: Application to probing zero-shear viscosity. *Journal of Rheology*, 63(6):863–881, November 2019.

[62] Kyle R. Lennon, Michela Geri, Gareth H. McKinley, and James W. Swan. Medium amplitude parallel superposition (MAPS) rheology. Part 2: Experimental protocols and data analysis. *Journal of Rheology*, 64(5):1263–1293, September 2020.

[63] Kyle R. Lennon, Gareth H. McKinley, and James W. Swan. Medium amplitude parallel superposition (MAPS) rheology. Part 1: Mathematical framework and theoretical examples. *Journal of Rheology*, 64(3):551–579, May 2020.

[64] Kyle R. Lennon, Gareth H. McKinley, and James W. Swan. Medium amplitude parallel superposition (MAPS) rheology. Part 1: Mathematical framework and theoretical examples. *Journal of Rheology*, 64(3):551–579, May 2020.

[65] A. I. Leonov, E. H. Lipkina, E. D. Paskhin, and A. N. Prokunin. Theoretical and experimental investigation of shearing in elastic polymer liquids. *Rheologica Acta*, 15(7-8):411–426, 1976. Publisher: Steinkopff-Verlag.

[66] Hui Li, Peng Yang, Parasmani Pageni, and Chuanbing Tang. Recent Advances in Metal-Containing Polymer Hydrogels. *Macromolecular rapid communications*, 38(14), July 2017.

[67] Paul F Luckham and Sylvia Rossi. The colloidal and rheological properties of bentonite suspensions. *Advances in Colloid and Interface Science*, 82(1-3):43–92, October 1999.

[68] Luca Martinetti and Randy H Ewoldt. Time-strain separability in medium-amplitude oscillatory shear. *Physics of Fluids*, page 31, 2019.

[69] J. Mewis. Thixotropy - a general review. *Journal of Non-Newtonian Fluid Mechanics*, 6(1):1–20, January 1979.

[70] J Mewis, B Kaffashi, J Vermant, and R J Butera. Determining Relaxation Modes in Flowing Associative Polymers Using Superposition Flows. 2001.

[71] Jan Mewis and Norman J. Wagner. Thixotropy. *Advances in Colloid and Interface Science*, 147-148:214–227, March 2009.

[72] R. W. Mooney, A. G. Keenan, and L. A. Wood. Adsorption of Water Vapor by Montmorillonite. I. Heat of Desorption and Application of BET Theory [1]. *Journal of the American Chemical Society*, 74(6):1367–1371, March 1952.

[73] Faith Morrison. *Understanding Rheology*. Oxford University Press, 2001.

[74] M. Mours and H. H. Winter. Time-resolved rheometry. *Rheologica Acta*, 33(5):385–397, 1994. Publisher: Steinkopff-Verlag.

[75] Johanne Mouzon, Iftekhar U. Bhuiyan, and Jonas Hedlund. The structure of montmorillonite gels revealed by sequential cryo-XHR-SEM imaging. *Journal of Colloid and Interface Science*, 465:58–66, March 2016.

[76] I. Mukasa-Tebandeke, P. Ssebuwufu, S. Nyanzi, A. Schumann, George Nyakairu, M. Ntale, and F. Lugolobi. The Elemental, Mineralogical, IR, DTA and XRD Analyses Characterized Clays and Clay Minerals of Central and Eastern Uganda. *Advances in Materials Physics and Chemistry*, 05:67–86, January 2015.

[77] Trevor S. K. Ng, Gareth H. McKinley, and Randy H. Ewoldt. Large amplitude oscillatory shear flow of gluten dough: A model power-law gel. *Journal of Rheology*, 55(3):627–654, May 2011.

[78] Liviu Iulian Palade, Vicent Verney, and Pierre Attané. A modified fractional model to describe the entire viscoelastic behavior of polybutadienes from flow to glassy regime. *Rheologica Acta*, 35(3):265–273, 1996. Publisher: Springer Verlag.

[79] Srinivasa R. Raghavan and Saad A. Khan. Shear-induced microstructural changes in flocculated suspensions of fumed silica. *Journal of Rheology*, 39(6):1311–1325, 1995. Publisher: Society of Rheology.

[80] Víctor H Rolón-Garrido, Manfred H Wagner, V H Rolón-Garrido, and M H Wagner. The damping function in rheology. *Rheol Acta*, 48:245–284, 2009.

[81] Kazi Sadman, Qifeng Wang, Yaoyao Chen, Bavand Keshavarz, Zhang Jiang, and Kenneth R. Shull. Influence of Hydrophobicity on Polyelectrolyte Complexation. *Macromolecules*, 50(23):9417–9426, 2017. Publisher: American Chemical Society.

[82] Ervin Sejdić, Igor Djurović, and Jin Jiang. Time–frequency feature representation using energy concentration: An overview of recent advances. *Digital Signal Processing*, 19(1):153–183, January 2009.

[83] A. Shahin and Yogesh M. Joshi. Irreversible Aging Dynamics and Generic Phase Behavior of Aqueous Suspensions of Laponite. *Langmuir*, 26(6):4219–4225, March 2010. Publisher: American Chemical Society.

[84] A. Shahin and Yogesh M. Joshi. Prediction of Long and Short Time Rheological Behavior in Soft Glassy Materials. *Physical Review Letters*, 106(3):038302, January 2011.

[85] A. Shahin and Yogesh M Joshi. Hyper-Aging Dynamics of Nanoclay Suspension. *Langmuir*, 28(13):5826–5833, April 2012.

[86] A. Shahin and Yogesh M Joshi. Physicochemical Effects in Aging Aqueous Laponite Suspensions. *Langmuir*, 28(44):15674–15686, November 2012. Publisher: American Chemical Society.

[87] Asheesh Shukla, Sachin Shanbhag, and Yogesh M. Joshi. Analysis of linear viscoelasticity of aging soft glasses. *Journal of Rheology*, 64(5):1197–1207, September 2020. Publisher: The Society of Rheology.

[88] Piyush K. Singh, Johannes M. Soulages, and Randy H. Ewoldt. Frequency-sweep medium-amplitude oscillatory shear (MAOS). *Journal of Rheology*, 62(1):277–293, December 2017. Publisher: The Society of Rheology.

[89] Julius Orion Smith. *Mathematics of the Discrete Fourier Transform (DFT): With Audio Applications*. Julius Smith, 2007. Google-Books-ID: fTOxS9huzHoC.

[90] Y. H. Sun, A. Concustell, M. A. Carpenter, J. C. Qiao, A. W. Rayment, and A. L. Greer. Flow-induced elastic anisotropy of metallic glasses. *Acta Materialia*, 112:132–140, 2016. Publisher: Elsevier Ltd.

[91] Sang Hoon Sung, Sunhyung Kim, Jan Hendricks, Christian Clasen, and Kyung Hyun Ahn. Orthogonal superposition rheometry of colloidal gels: Time-shear rate superposition. *Soft Matter*, 14(42):8651–8659, 2018. Publisher: Royal Society of Chemistry.

[92] H. Suzuki, T. Kinjo, Y. Hayashi, M. Takemoto, and Kanji Ono. Wavelet transform of acoustic emission signals. *Journal of Acoustic Emission*, 14:69–84, January 1996.

[93] R I Tanner. From A to (BK)Z in Constitutive Relations. *Citation: Journal of Rheology*, 32:673, 2006.

[94] Nicholas W. Tschoegl. *The Phenomenological Theory of Linear Viscoelastic Behavior: An Introduction*. Springer-Verlag, Berlin Heidelberg, 1989.

[95] H van Olphen. Internal mutual flocculation in clay suspensions. *Journal of Colloid Science*, 19(4):313–322, April 1964.

[96] Priya Varadan and Michael J Solomon. Shear-Induced Microstructural Evolution of a Thermoreversible Colloidal Gel. 2001.

[97] Zsigmond Varga and James W Swan. Large scale anisotropies in sheared colloidal gels. *Citation: Journal of Rheology*, 62:405, 2018.

[98] J. Vermant, P. Moldenaers, J. Mewis, M. Ellis, and R. Garritano. Orthogonal superposition measurements using a rheometer equipped with a force rebalanced transducer. *Review of Scientific Instruments*, 68(11):4090–4096, November 1997.

[99] J Vermant, P Van Puyvelde, P Moldenaers, J Mewis, and G G Fuller. Anisotropy and Orientation of the Microstructure in Viscous Emulsions during Shear Flow. Technical report, 1998.

[100] J. Vermant, L. Walker, P. Moldenaers, and J. Mewis. Orthogonal versus parallel superposition measurements. *Journal of Non-Newtonian Fluid Mechanics*, 79(2-3):173–189, 1998. Publisher: Elsevier Sci B.V.

[101] Zisis Vryzas, Vassilios C. Kelessidis, Lori Nalbantian, Vassilis Zaspalis, Dimitrios I. Gerogiorgis, and Yiming Wubulikasimu. Effect of temperature on the rheological properties of neat aqueous Wyoming sodium bentonite dispersions. *Applied Clay Science*, 136:26–36, February 2017.

[102] M. H. Wagner and J. Meissner. Network Disentanglement and Time-Dependent Flow Behaviour of Polymer Melts. *Die Makromolekulare Chemie*, 181(7):1533–1550, 1980.

[103] H. H. Winter. The Critical Gel. In *Structure and Dynamics of Polymer and Colloidal Systems*, pages 439–470. Springer Netherlands, 2002.

[104] H Henning Winter and Francois Chambon. Analysis of Linear Viscoelasticity of a Crosslinking Polymer at the Gel Point. *Citation: Journal of Rheology*, 30:367, 1986.

[105] Misazo Yamamoto. Rate-Dependent Relaxation Spectra and Their Determination. *Transactions of the Society of Rheology*, 15(2):331–344, July 1971.

[106] L. J. Zapas and T. Craft. Correlation of Large Longitudinal Deformations With Different Strain Histories. *Journal of Research of the National Bureau of Standards. Section A, Physics and Chemistry*, 69A(6):541–546, 1965.